ANALYIS OF AIRBORNE MICROWAVE POLARIMETRIC RADIOMETER MEASUREMENTS IN THE PRESENCE OF DYNAMIC PLATFORM ATTITUDE ERRORS

by:

JEAN YVES W KABORE
B.S. University of Central Florida, 2003

A thesis submitted in partial fulfillment of the requirements
for the degree of Master of Science
in the Department of Electrical and Computer Engineering
in the College of Engineering and Computer Science
at the University of Central Florida
Orlando, Florida

Spring Term
2006

ABSTRACT

There are numerous applications for airborne imaging systems in remote sensing, and this thesis deals with a new microwave polarimetric radiometer technique for inferring ocean surface wind direction. This technique is based upon the anisotropy of the polarized ocean blackbody emissions at microwave frequencies relative to the azimuth angle between the microwave radiometer antenna "look" direction and the direction of the wind. Because of the weak wind direction signature, it is important that all systematic brightness temperature (Tb) errors be eliminated, especially those that vary with the radiometer antenna scan position (look direction). This can be accomplished either in hardware implementation or through data processing corrections. Unfortunately, the misalignment of the axis of rotation for a conical-scanning imager can introduce such azimuthally dependent errors of significant magnitude. As the title suggests, the analysis of the resulting Tb errors caused by static and dynamic time-varying aircraft attitude errors is the main thrust of this thesis.

In this thesis, we present analytical models developed to account for platform attitude changes on measured ocean microwave brightness temperature collected by a conically scanning radiometer. Data processing procedures for removing unwanted variations in ocean brightness temperatures are outlined. The analytical models are validated by making comparisons between modeled and measured Tb's obtained by the Conically Scanning Two-Look Airborne Radiometer (C-STAR). Results demonstrated that the analytical Tb model accurately predicts the measured polarized Tb's under actual flight conditions.

ACKNOWLEDGMENTS

I would like to thank my family and all of those who have supported me throughout the years while I worked on this thesis. I would especially like to thank my parents, and my sisters Nadine, Armelle, and Gwladys Kabore for their unconditional support.

I would like to express my sincere gratitude to my advisor and committee chair Dr Linwood Jones for giving me the opportunity to work on this thesis. I am greatly indebted to him for all the countless hours he spent guiding and supporting me throughout this project.

Last but not least, I would like to say thank you to my committee members including Mr James Johnson, Dr. Takis Kasparis, and Dr. Stephen Watson for their time and guidance.

This research was partially sponsored under grant from the NASA Marshall Space Flight Center, Huntsville, AL.

TABLE OF CONTENTS

LIST OF FIGURES

LIST OF TABLES

LIST OF ACRONYMS

C-STAR	Conically Scanning Two-Look Airborne Radiometer
Tb	Brightness temperature
V	Vertical
H	Horizontal
P	+45
Q	-45
K	Kelvin
FWD	Forward
Pol	Polarization
SST	Sea surface temperature
QC	Quality control
PRA	Polarization rotation angle
CCW	Counter clockwise
CAMEX	Convection and moisture experiments
NASA	National Aeronautics and Space Administration
IFOV	Instantaneous field of view
IF	Intermediate frequency

CHAPTER 1: INTRODUCTION

1.1Background of microwave remote sensing

Microwave remote sensing is the engineering discipline related to the measurement of naturally emitted electromagnetic energy. It encompasses the study of radio wave propagation and its interaction with material media including surface, volume scattering and emissions. Because of the great distances involved, electromagnetic waves are used for the measurement of the media's parameters. Other means of measurements, such as aerial photography or optical imagery from space can be used but microwaves offer several advantages which include the ability to penetrate clouds, to some extent penetrate rain and their ability to work both day and night [1, 2].

Remote sensors are usually divided into two categories, active and passive. Active instruments are radars and provide their own source of illumination. They are usually referred to as scatterometers or imaging radars. Passive devices measure the emitted blackbody radiation from the scene under observation and are referred to as radiometers.

1.2. Fundamental Concepts of Microwave Remote Sensing

According to thermodynamic principles, all matter at temperatures greater than absolute zero both absorb and emit noncoherent electromagnetic (EM) energy simultaneously. This absorption causes the body's physical temperature or thermodynamic temperature to rise, which in turn results in an increase in the emitted EM

radiation [1]. This process continues until the body reaches thermal equilibrium at which point its physical temperature is constant and the amount of energy absorbed is equal to the amount of energy emitted. A medium, which perfectly absorbs and emits EM energy is called a blackbody. The medium has zero reflectance and transmittance meaning all energy incident upon the medium is absorbed internally, and the energy is converted to heat which raises the mediums thermodynamic temperature. The energy flux density emitted by a blackbody, shown in Fig. 1, varies with wavelength and is described by Planck's law [1]:

$$S(\lambda) = \frac{2\pi hc^2}{\lambda^5} \frac{1}{e^{ch/\lambda kT} - 1} \qquad (1.1)$$

where,

h = Planck's constant = 6.6253x10 $^{-34}$, joule/sec

k = Boltzmann's constant = 1.38x10 $^{-23}$, joule/Kelvin

c = the speed of light in vacuum = 3.0 x 10^8 m/s

T = physical temperature of black body in Kelvin

λ = wavelength

For an incremental wavelength, the total radiated flux in Watts per unit area per incremental wavelength (W*cm^{-2}*μm^{-1}) is given by:

$$S(\lambda)_{Total} = \int S(\lambda) d\lambda \qquad (1.2)$$

As can be noted from Fig. 1, the shape of the blackbody curve changes with the medium's physical temperature. The peak of the emission increases in proportion to the physical temperature of the body. Over the low frequency region of Planck's emission

spectrum, the spectral emittance can be approximated by a straight-line relationship on a Log-Log plot. This is know as Rayleigh-Jeans law:

$$S(\lambda) = \frac{2\pi ckT}{\lambda^4} \qquad (1.3)$$

For Rayleigh-Jeans law to be applicable, $ch/\lambda << kT$, which means that this law is only applicable to frequencies less than 100 GHz.

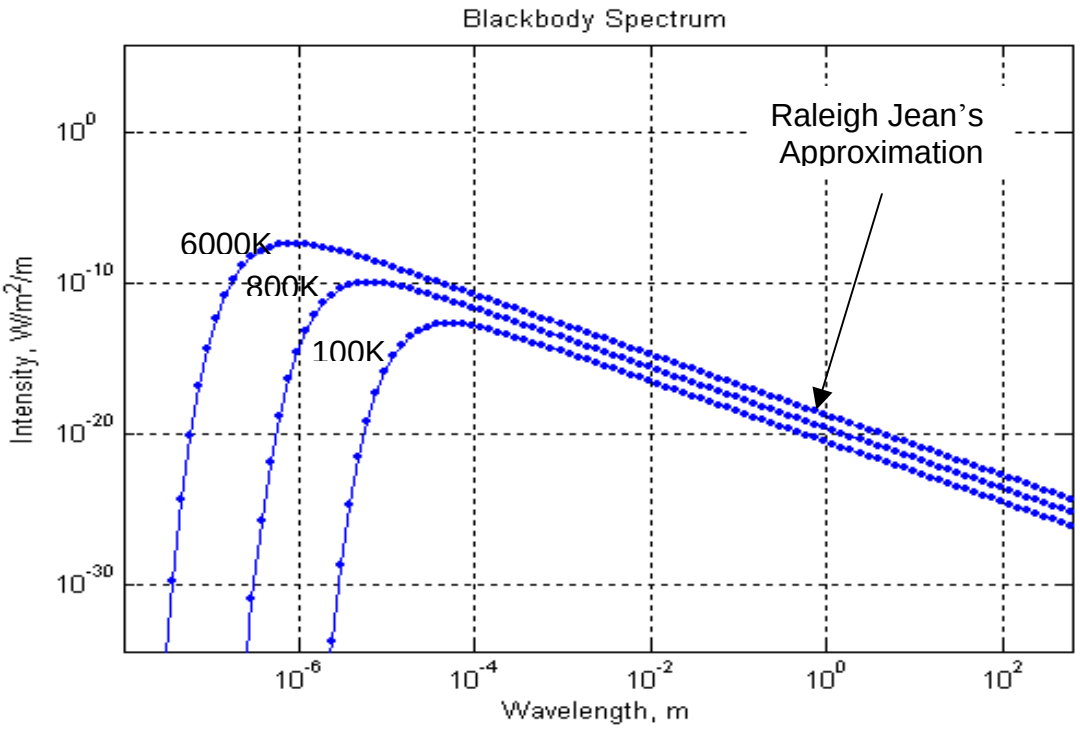

Figure 1.1 Planck's Law

1.3 Ocean Surface Emission and Reflection

Emissivity is defined as the blackbody radiation efficiency. It is a measure of how well a medium radiates EM energy taking into account internal reflections. Since a blackbody is a perfect emitter, it has an emissivity equal to unity. The emissivity of a body depends on the frequency of observation and for non-blackbodies, also referred to as grey-bodies, it is the ratio of the spectral emittance of the body to that of a blackbody:

$$\varepsilon(\lambda) = \frac{S(\lambda)_{non-blackbody}}{S(\lambda)_{blackbody}} \quad (1.4)$$

When observing a blackbody at microwave frequencies, the power collected by the microwave antenna is proportional to the body's physical temperature and the bandwidth of the receiver.

$$P_{blackbody} = kT_{phys}Bandwidth \quad (1.5)$$

Where:

k = Boltzmann's constant = 1.38×10^{-23}, joule/Kelvin

T = Body's physical temperature, Kelvin

Bandwidth=Receiver bandwidth, Hertz

Therefore, the body's physical temperature can be determined from the power collected by the radiometer antenna. For non-blackbodies, the measured microwave brightness temperature, Tb, is the product of the medium's emissivity and it's physical temperature:

$$T_b = \varepsilon * T_{phys} \quad (1.6)$$

The emissivity can be determined by considering the interaction EM waves at the surface boundary between two media, in our case air and sea water. As an EM wave travels from

one medium into another, at the surface boundary part of the wave is reflected and part is absorbed into the medium as illustrated in Fig. 1.2 [3]. The difference in the intrinsic impedance between the two media determines how much of the wave is reflected and absorbed. This intrinsic impedance is function of the medium's permittivity and permeability and is given by:

$$\eta = \sqrt{\mu / \varepsilon} \text{ , ohms} \qquad (1.7)$$

Where : μ = medium's permeability

ε = medium's permittivity

The permittivity is also referred to as the complex dielectric constant of the medium. It is a function of frequency, physical temperature and salinity and knowing its precise value is essential to determining the microwave radiation emitted by the ocean surface [4].

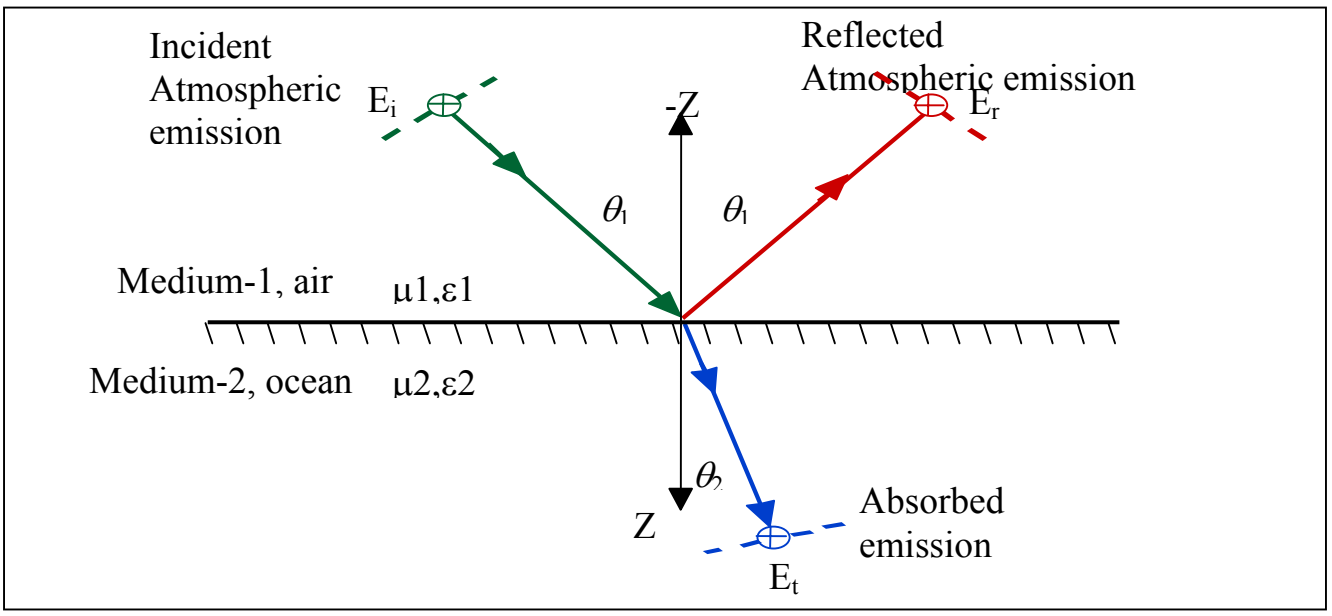

Figure 1.2 Plane waves at dielectric interface

The angle between the incident and a normal to the surface is referred to as the incidence angle. That between the reflected wave and the normal to the surface is called the reflection angle. As part of the wave is transmitted through to the medium, it is refracted and the angle between the refracted wave and a normal to the surface is referred to as the angle of refraction. Due to the conservation of energy, the magnitude of the incident wave is equal to the sum of the reflected and refracted waves [3]. The relation ship between the reflected and incident wave is described by the Fresnel reflection coefficient which is a function of incidence angle, polarization and the dielectric constant of the medium 2:

$$\rho_{v-pol} = \frac{\varepsilon_2 \cos\theta_1 - \sqrt{\mu_2\varepsilon_2 - \sin^2\theta_1}}{\varepsilon_2 \cos\theta_1 + \sqrt{\mu_2\varepsilon_2 - \sin^2\theta_1}} \qquad (1.8)$$

$$\rho_{H-pol} = \frac{\mu_2 \cos\theta_1 - \sqrt{\mu_2\varepsilon_2 - \sin^2\theta_1}}{\mu_2 \cos\theta_1 + \sqrt{\mu_2\varepsilon_2 - \sin^2\theta_1}} \qquad (1.9)$$

A plot of both the horizontal and reflection coefficient versus incidence angle is shown in Fig. 1.3. At zero degrees, both the vertical and horizontal polarizations have the same reflection coefficients. As the incidence angle increases, the horizontal reflection coefficient gradually increases while that of the vertical polarization decreases at approximately twice the rate of the horizontal. At a angle near grazing, the vertical reflection coefficient goes to zero. This is called the Brewster angle and it is the angle at which there is no reflection and all energy incident upon the surface is transmitted to the medium.

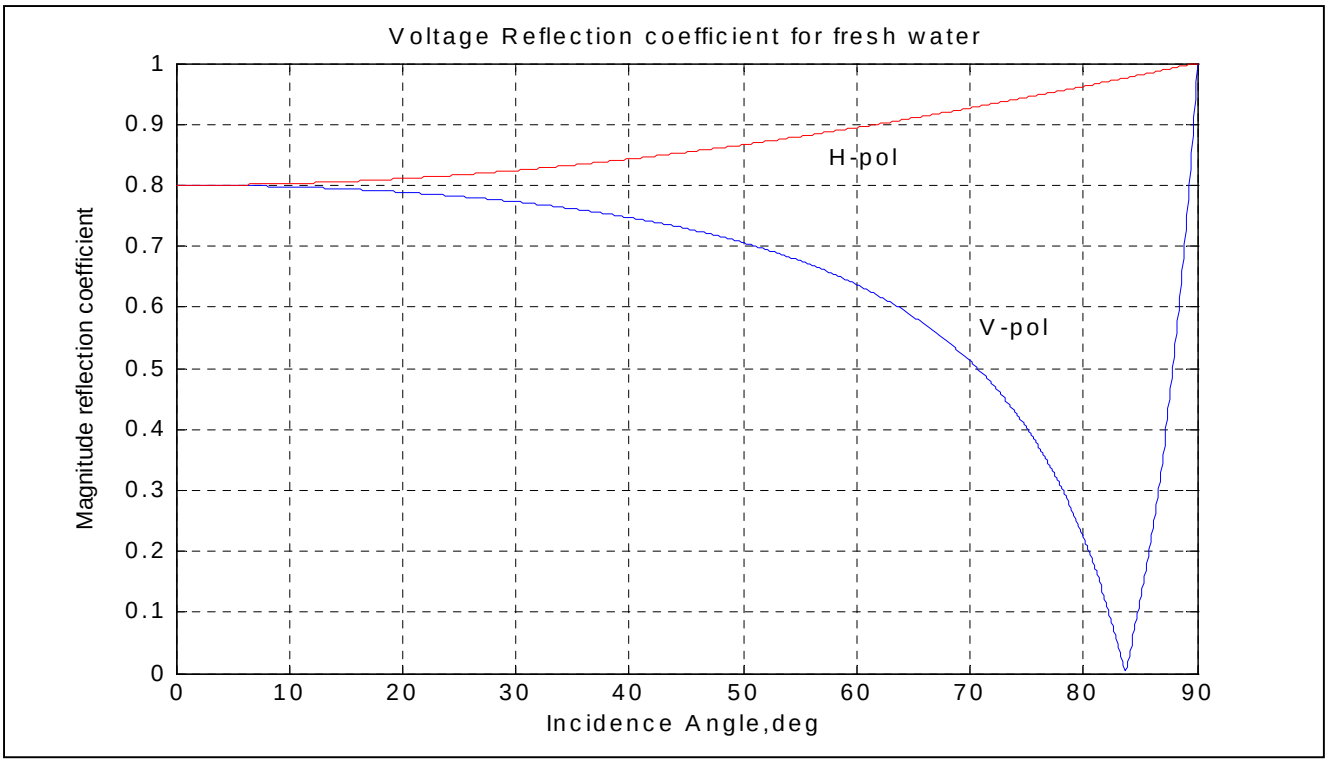

Figure 1.3 Example of Fresnel reflection coefficient

The power reflection coefficient is the square of the reflection coefficient and is given by:

$$\Gamma_{V-pol} = \left|\rho_{v-pol}\right|^2 \qquad (1.10)$$

$$\Gamma_{H-pol} = \left|\rho_{H-pol}\right|^2 \qquad (1.11)$$

Once the power reflection coefficient is obtained, it can be used to calculate the emissivity by the conservation of energy as:

$$\varepsilon = 1 - \Gamma \qquad (1.12)$$

1.4 Microwave Interaction in the Atmosphere

The earth's atmosphere plays an important role in microwave remote sensing. Through an understanding of the interaction between microwaves and atmospheric constituents such as water vapor and oxygen; the influence of the atmosphere on ocean surface or land observations can be accounted for. Such an understanding also provides means to monitor those atmospheric parameters and weather conditions. The upwelling brightness temperature within the atmosphere is predominantly due to emission of microwave energy by water vapor and oxygen molecules [5, 1]. By the laws of thermodynamics and blackbody radiation, a body that absorbs energy must also emit energy to maintain temperature equilibrium.

1.5 Water Vapor Absorption

The presence of water vapor (or humidity) in the atmosphere causes an increase in the measured brightness due to the quantum interaction between the EM waves and water vapor molecules. Absorption of EM energy occurs at key resonant frequencies, which in the case of water vapor are 21 GHz, 183 GHz and 325 GHz. The amount of absorption is dependent on the water vapor density, and the air temperature and pressure of the atmosphere along the observation path. As altitude increases, the number of water vapor molecules along with temperature decreases, but the decrease in pressure reduces the bandwidth of water vapor emission [1], which increases the overall strength of absorption. The water vapor absorption coefficients for frequencies below 300 GHz is

shown in Fig. 1.4. It is calculated for sea level conditions (Temperature = 300 K, Pressure = 1013 mbar, and pressure = 7.5 gm) as a function of frequency.

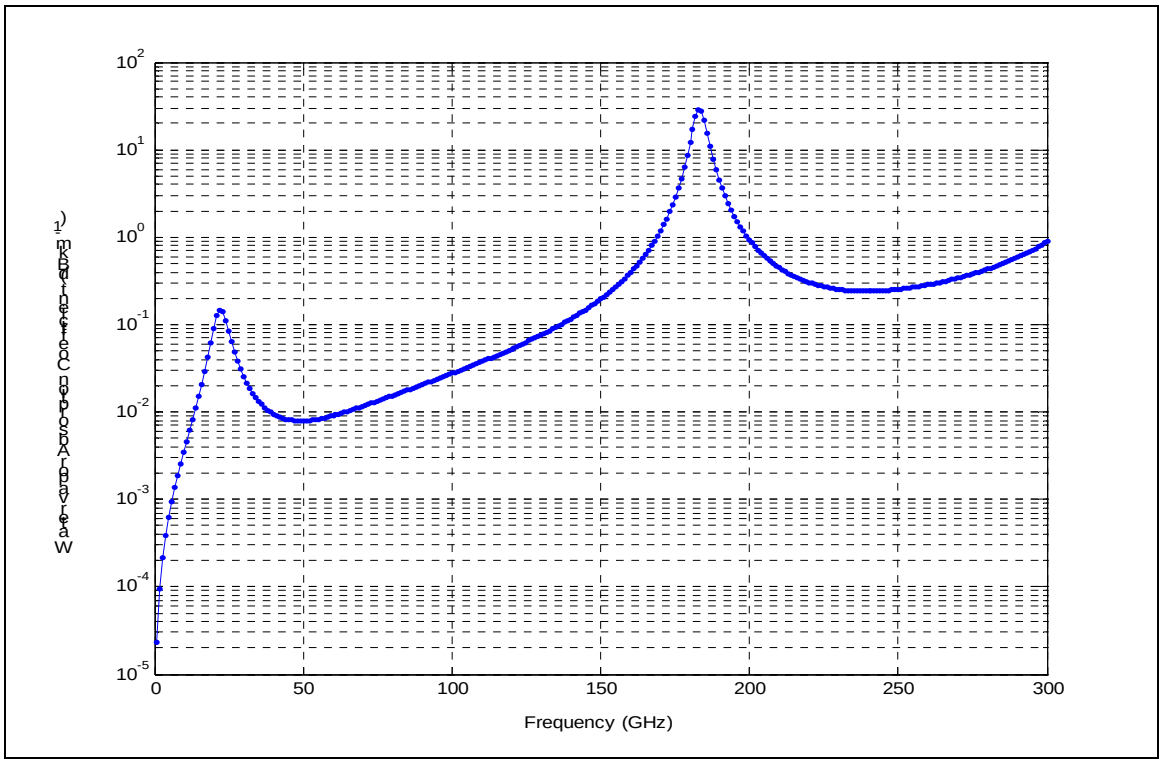

Figure 1.4 Attenuation coefficient of atmospheric water vapor for sea-level conditions.

1.6 Oxygen Absorption

The second major contributor to atmospheric emission is oxygen. Electromagnetic absorption by oxygen molecules occurs at 60 GHz and 118.75 GHz [5]. Like water vapor, the strength of the absorption depends on the number of oxygen molecules, altitude, pressure and on air temperature. As altitude increases, the number of oxygen molecules decreases, but the decrease in pressure reduces the absorption bandwidth

causing an increase emission. Figure 1.5 illustrates oxygen absorption for sea level conditions.

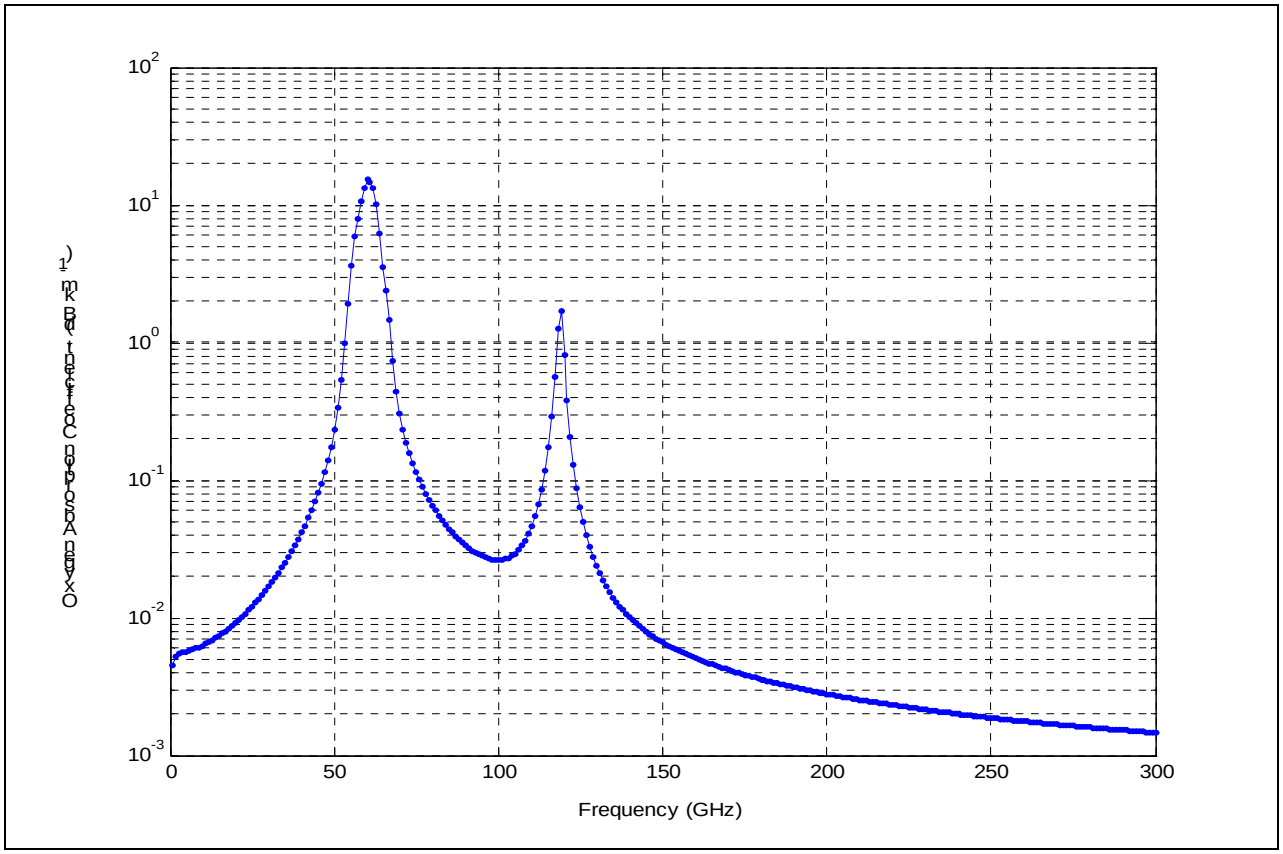

Figure 1.5 Attenuation coefficient of atmospheric oxygen for sea-level conditions.

1.7 Radiative Transfer Theory

The collection of natural gray-body emission, received by a satellite microwave radiometer viewing the ocean through the Earth's atmosphere, is illustrated conceptually in Fig. 1.6. Because each source of brightness temperature is wide-band Gaussian noise, the radiometer simply collects the total power i.e., the sum of the three components. To

interpret the radiometer measurements, the theory of radiative transfer must be applied to model the emissions (brightness temperature) from various sources [6, 7, 8, 1], which are:

1. The ocean brightness temperature propagated upwards through a slightly absorbing atmosphere to the antenna.
2. The sum of the cosmic background radiation and the downward-welling brightness temperature of the atmosphere propagated down to the ocean surface and then reflected and transmitted upwards to the antenna.
3. Direct upwelling emission of the brightness temperature of the atmosphere to the antenna.

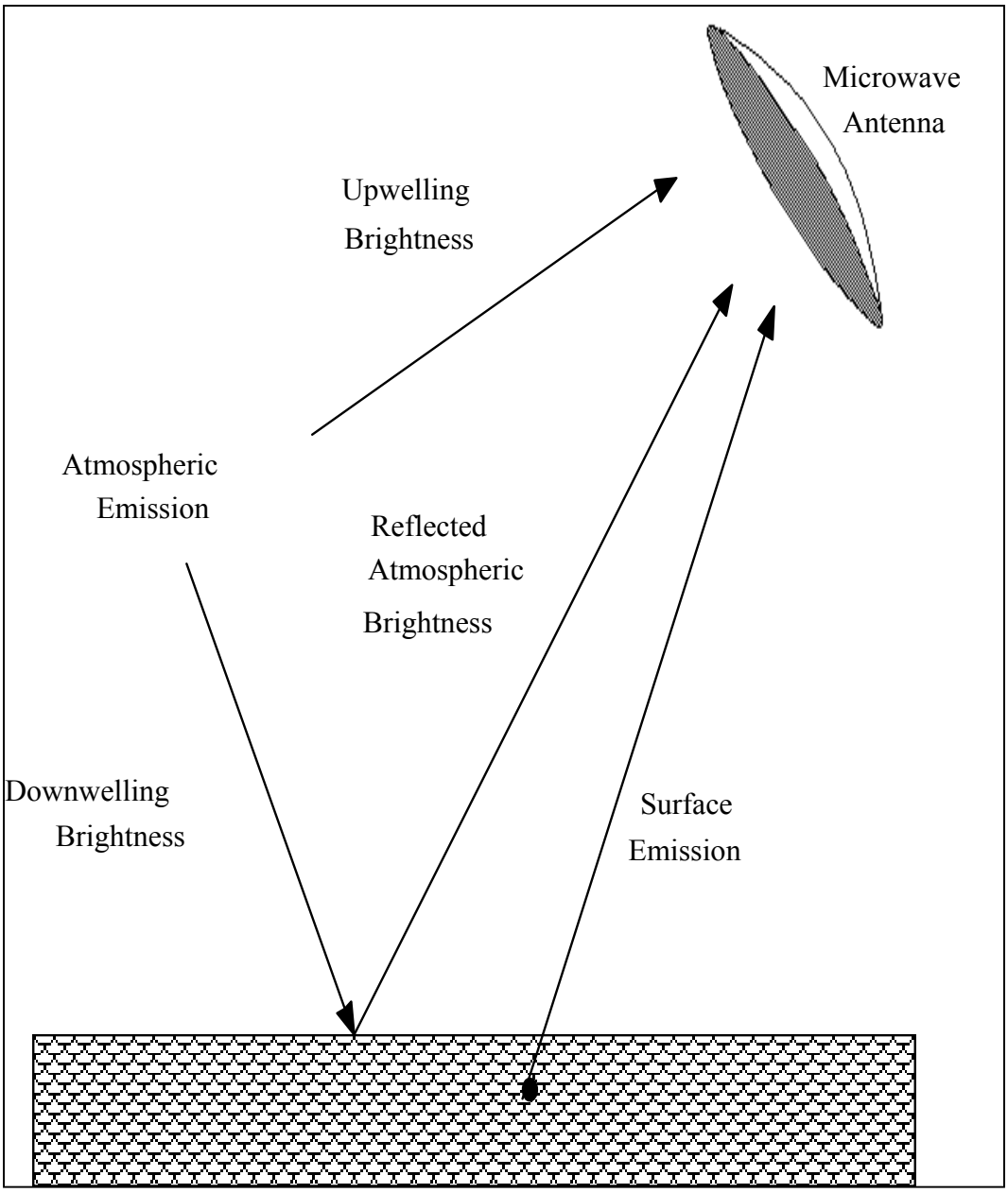

Figure 1.6 Satellite microwave radiative transfer concept.

All electromagnetic factors contributing to the apparent brightness temperature are a function of microwave frequency, antenna polarization and incidence angle (θ). Along the propagation path observed from the satellite antenna to the surface, the path length through the atmosphere is approximated by the height of the atmosphere times the $\sec\theta$.

Along this path, knowing the total loss factor of the atmosphere, L_o, affects the Tb seen by the satellite radiometer. The attenuation factor K_a, is the summation of absorption coefficients due to water vapor, oxygen and cloud liquid water. The optical depth (opacity) of the atmosphere is defined by:

$$\tau_o = \int_0^L K_a dz, \text{ Nepers,} \tag{1.13}$$

where **z** is the height above the surface. The total loss from the surface to the top of the atmosphere,

$$L_o = e^{-\tau_o} \tag{1.14}$$

The down welling brightness temperature,

$$T_{dn} = \sec(\theta)\int_0^\infty K_a(z)T(z)e^{-\tau_o(z)}dz, \tag{1.15}$$

where $T(z)$ is the atmospheric physical temperature profile, and the integral upper limit is the top of the atmosphere (~ 20 Km). Once the down-welling energy reaches the ocean surface, some of it is absorbed in the ocean while the rest is reflected specularly into the atmosphere [1]. The direct emission of the ocean radiance from the ocean to the atmosphere is:

$$T_b = \varepsilon * SST, \tag{1.16}$$

where SST is the sea surface temperature

The sky brightness T_{sky}, is:

$$T_{sky}(\theta) = T_{down}(\theta) + T_{ex}(\theta)e^{-\tau_o \sec\theta} \tag{1.17}$$

T_{ex} is the sum of the cosmic and galactic radiation equal to 2.7K

A portion of the microwave incident on the ocean surface is reflected, T_{refl} towards the atmosphere. The magnitude of the reflected wave is dependent on the emissivity (power reflectivity) of the ocean.

$$T_{refl}(\theta) = \Gamma T_{sky}(\theta) = (1 - \varepsilon) T_{sky}(\theta) \tag{1.18}$$

The resulting brightness measured by the radiometer is given by the radiative transfer equation:

$$T_{ap}(\theta) = T_{up}(\theta) + T_b e^{-\tau_o \sec\theta} + T_{refl} e^{-\tau_o \sec\theta} \tag{1.19}$$

CHAPTER 2: MICROWAVE RADIOMETERS

2.1. Conical Scanning Microwave Radiometers

"Radiative Transfer Theory" is used to describe the apparent brightness temperature measured by a microwave antenna. In microwave radiometry, the simplest types of radiometers used to measure apparent brightness is the "Total Power Radiometer", which is shown in Fig. 2.1. It is composed of an antenna, a receiver, a square law detector, and an integrator. In a radiometer system, the antenna is the most important component [2]. It has directional characteristics, which determine the instantaneous field of view (IFOV) from which electromagnetic energy is collected. It also has ohmic losses that contributes microwave biases, which must be characterized for accurate interpretation. The types of antennas used in radiometry are similar to those used in communication systems, except that the beam efficiency and spatial resolution are the most important characteristic in radiometry.

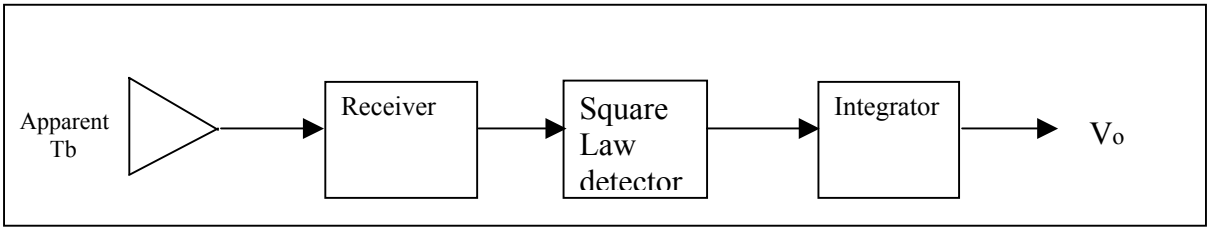

Figure 2.1 Simplified block diagram of a total power radiometer

The noise output power from the antenna (input to the receiver), P_a, is

$$P_a = KT_aB \tag{2.1}$$

Where K is Boltzmann's constant, J/K

T_a is the antenna noise temperature, K

B is the noise effective bandwidth of the radiometer receiver, Hz

The antenna is connected to a receiver, which generates noise power internally; therefore, the radiometer system has an effective input noise power:

$$P_{sys} = KT_{sys}B \tag{2.2}$$

Where

Tsys the system input noise temperature, define as:

$$T_{sys} = T_a + T_{rec} \tag{2.3}$$

T_{rec} is the receiver equivalent input noise temperature, K

In the receiver, the signal is then amplified with a power gain, G, by radio frequency and/or intermediate frequency (IF) amplifiers to produce an output power (average), P_{IF}

$$P_{IF} = GkT_{sys}B \tag{2.4}$$

A square law detector is used to detect the mean value of the system output noise power. The average value of the output of the square law detector, $\overline{V_d}$ is:

$$\overline{V_d} = C_d P_{IF} \tag{2.5}$$

Where C_d is the square law detector power sensitivity constant

The signal at the output of the square law detector is then passed through a low pass filter to reduce unwanted ac signal components of the detected voltage. The low pass filter also acts as an integrator to integrate V_d over some interval of time, τ_{avg}. The integrator

dc output voltage component (I_{out}) is proportional to the average system temperature $<T_{sys}>$. The minimum change in T_{sys} that can be reliably detected (i.e., the radiometer measurement precision) is known as the radiometer ΔT. This is described by eq. 2.6, which defines the sensitivity of the total power radiometer.

$$\Delta T_{sys} = \frac{T_{sys}}{\sqrt{B\tau_{avg}}} \tag{2.6}$$

During radiometer operation, the transfer function (relating input power to output power) must be precisely known. Unfortunately, in the case of the total power radiometer, the receiver gain is variable and therefore the instrument must be continuously calibrated during operation. The most common mean of calibration is to use two external calibration targets that calibrate the entire radiometer. This is achieved by placing black body targets of different known temperature over the antenna.

In this manner, the integrator output ($I_{out,}$) is linearly related to the antenna temperature $T_{a,}$. In the case of the total power radiometers, a hot and cold load is used as the calibration targets (see Fig. 2.2) and their corresponding values are:

$$I_{out}^{h} = a(T_{cal}^{h}) + b, \text{ hot target calibration point} \tag{2.7}$$

$$I_{out}^{c} = a(T_{cal}^{c}) + b, \text{ cold target calibration point} \tag{2.8}$$

Solving the above equations for the constants a (receiver gain) and b (integrator offset) provide the radiometer linear transfer function. With good square-law detectors, linearity is not a significant issue as the dynamic range of the radiometer is very small (< 3 dB) [2]. The usual practice is to ensure that the hot and cold targets bracket the scene brightness temperature.

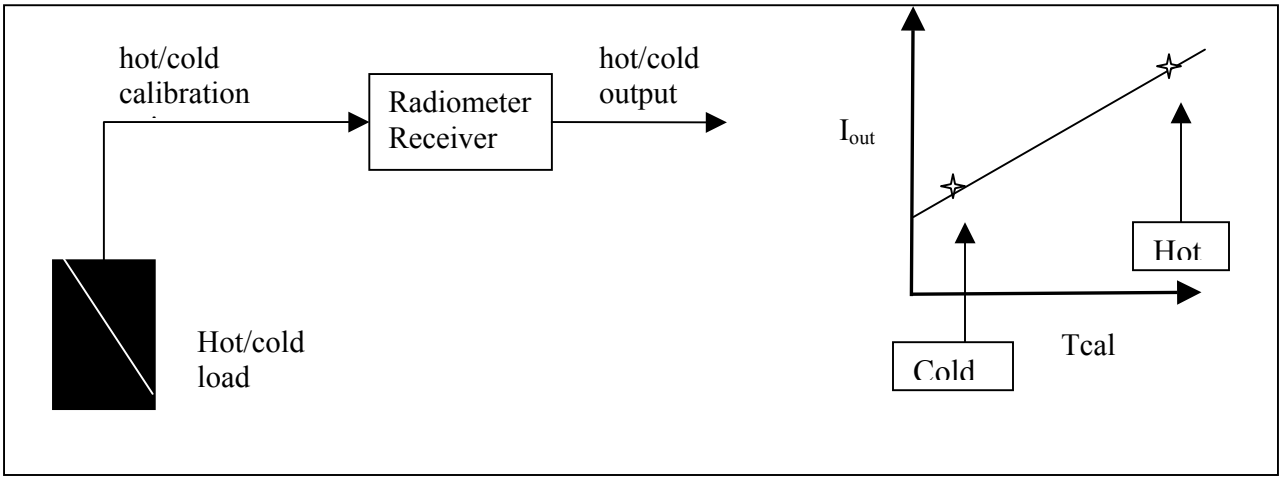

Figure 2.2: Calibration of a total power radiometer receiver

2.2 Conical Scan Geometry

The most commonly used viewing configuration for microwave radiometers imagers is "conical scan". For such an earth viewing instrument, the major advantage is that the incidence angle, defined by the angle between the normal to the surface and the antenna direction of propagation, remains constant as the antenna scans in azimuth. Also, this configuration eases calibration by allowing the antenna and feeds to rotate and view the calibration loads once per revolution. Fig. 2.3 illustrates the geometry of a satellite radiometer looking at the earth's surface. θi represents the incidence angle and is related to the cone angle by:

$$\phi = \arcsin\left[\frac{\rho}{\rho + h}\sin\theta i\right] \qquad (2.9)$$

$$\theta i = \arcsin\left[\frac{\rho + h}{\rho}\sin\phi\right] \qquad (2.10)$$

Where:

ρ is the radius of the earth, and h is the satellite altitude

R is the slant range given by:

$$R = \frac{\rho \sin\gamma}{\sin\phi} \qquad (2.11)$$

Where:

γ is the angle formed by a line from the center of the earth to the satellite and a line from the center of the earth to the observation point.

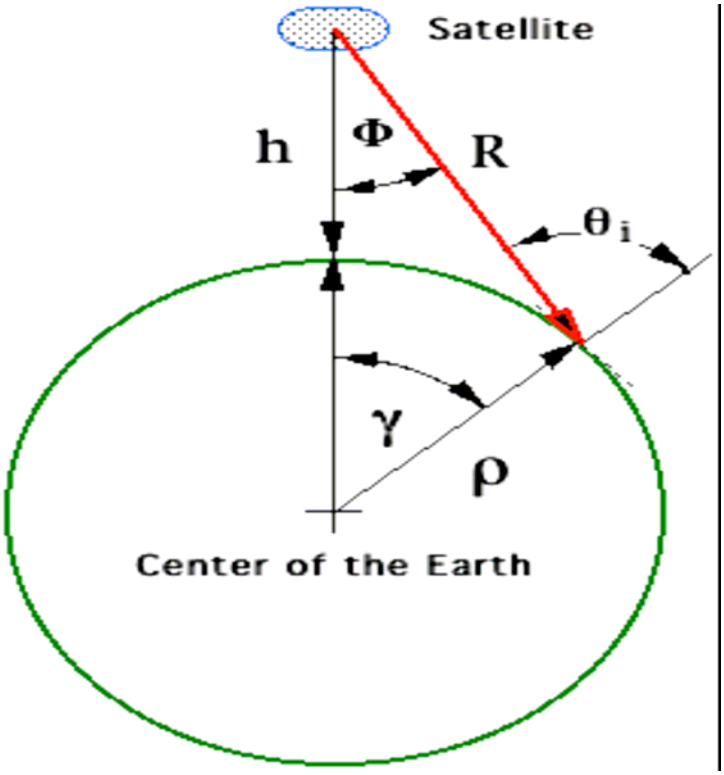

Figure 2.3 Conical scan geometry in incidence plane.

As the antenna scans, it makes observations of the surface over its instantaneous field of view (IFOV), which is the elliptical shape antenna footprint on the surface (see Fig. 2.4).

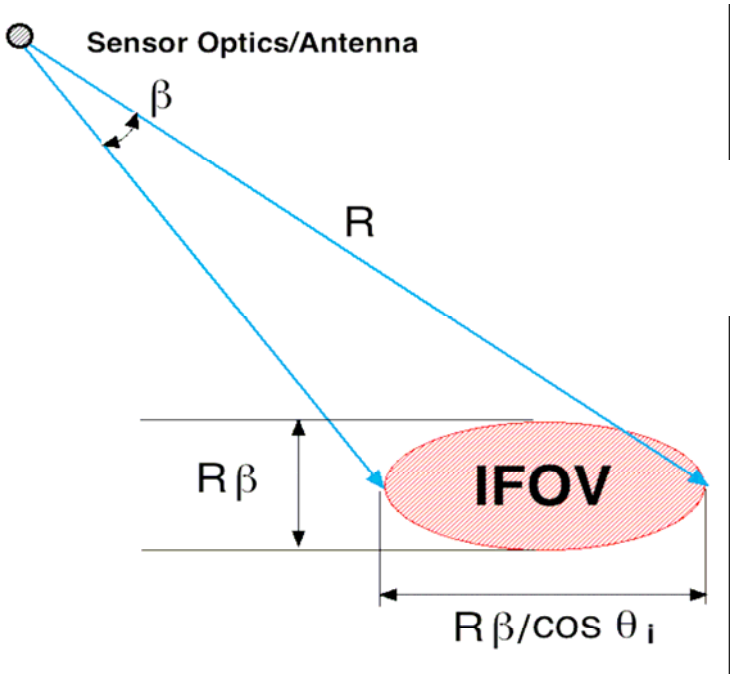

Figure 2.4 Radiometer instantaneous field of view.

2.3 CSTAR description

C-STAR was designed by NASA Marshal Space Flight Center to passively measure microwave emissions of wind and ocean interactions [9]. It was flown during the fourth field campaign in the Convection And Moisture Experiments (CAMEX) series that ran from August 16 to September 24, 2001.

C-STAR is a total power microwave radiometer that measures brightness temperature over a conical scan of the ocean's surface with two dual polarized antenna beams. The simplified block diagram (only one beam) is shown in Fig. 2.5, and Table 2.1 gives the key radiometer parameters and performance.

The instrument is mounted on the bottom of the aircraft with the spin axis aligned perpendicular to the aircraft yaw axis (Fig. 2.6). Two radiometer horns point to the nadir and two planar reflectors are used to produce squinted beams with identical cone angles of 45° with respect to the spin axis. With the spin axis aligned to point to the nadir (perpendicular to the surface), this results in a nominal incidence angle $\theta = 53°$ at the surface, and the two antenna beams provide vertical/horizontal and ± 45° polarizations (Fig 2.7). Unfortunately during flight, the aircraft experiences periodic changes in both the pitch and roll, which misaligns the spin axis and introduces an artificial ocean Tb anisotropy. From an aircraft altitude of approximately 20 km, the IFOV on the surface is approximately 5.2 km [9].

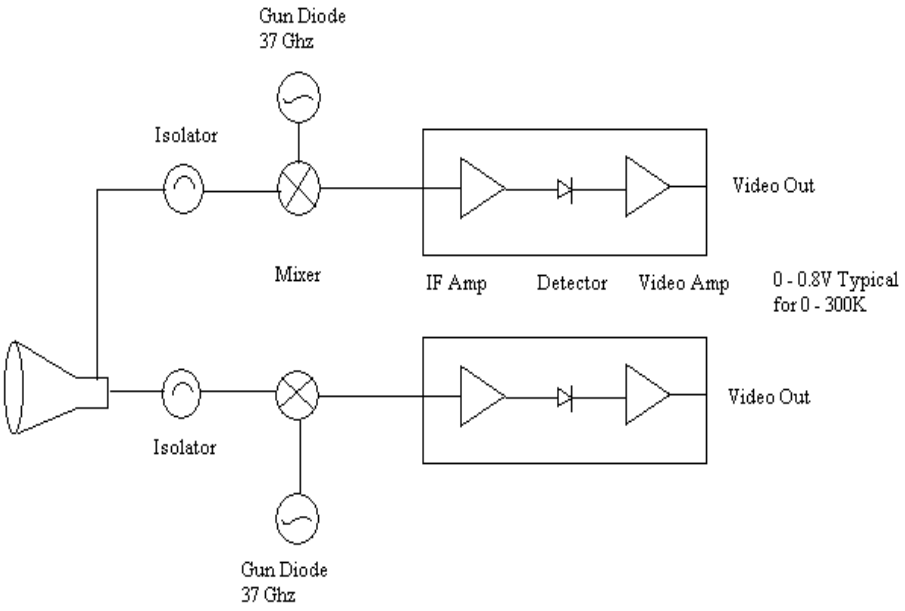

Figure 2.5 C-STAR radiometer simplified block diagram.

Table 2.1 C-STAR Characteristics and Performance

Frequency	37 GHz
Antenna	2 Horns & mirrors
Halfpower Beamwidth	7.5 degrees
Polarization	H, V, + 45, - 45
Incidence Angle	53 Degrees
Receivers	Superheterodyne
Bandwidth	900 Mhz
Delta T	0.15 K
A/D	16 bits
Integration time	100 ms
Scan rate/period	6 rpm (10 s period)
Azimuth range	Fore: 0° ± 45° Aft: 180° ± 45°
Pixels	26 fore/aft per scan
Instrument mass	100 lbs

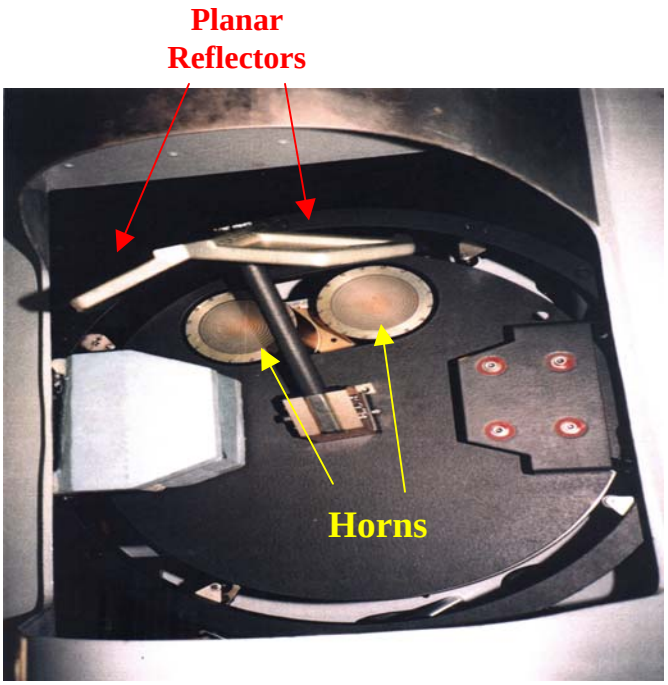

(a)

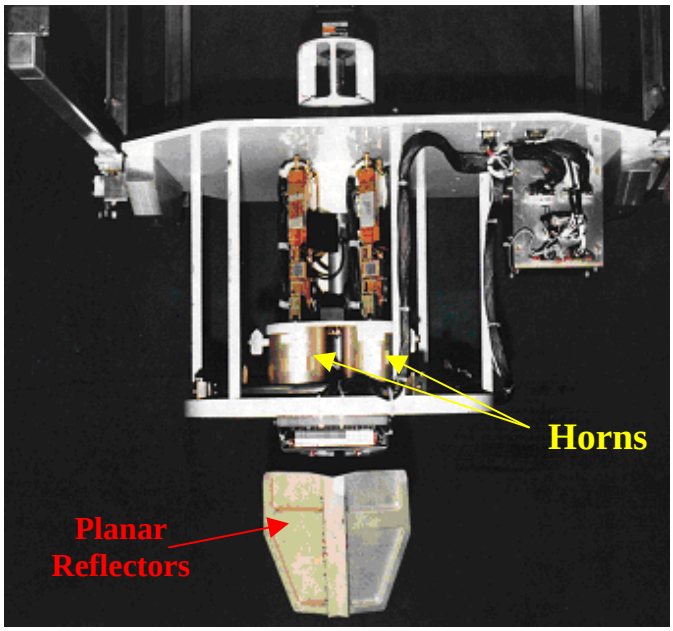

(b)

Figure 2.6: (a) Bottom view of C-Star radiometer mounted on a NASA aircraft,

(b) Side view of C-STAR .

2.4 C-STAR Scan Geometry

The instrument scans clockwise over 360° in azimuth, but data are collected only for forward (fwd) and rearward (aft) scenes that are each 90° sectors in azimuth. The fwd scene is centered on the flight direction (0°) with measurements ± 45° azimuth on either side; and the aft scene is centered at 180° (± 45°). Each scene consists of 26 pixels that are collected over a time of 2.5 seconds [10]. There are hot and ambient (cold) calibration targets located at 90° and 270° in azimuth respectively. Once each scan, both of the calibration loads are viewed by the horn antennas. Using these known temperature values, accurate radiometric calibration is achieved.

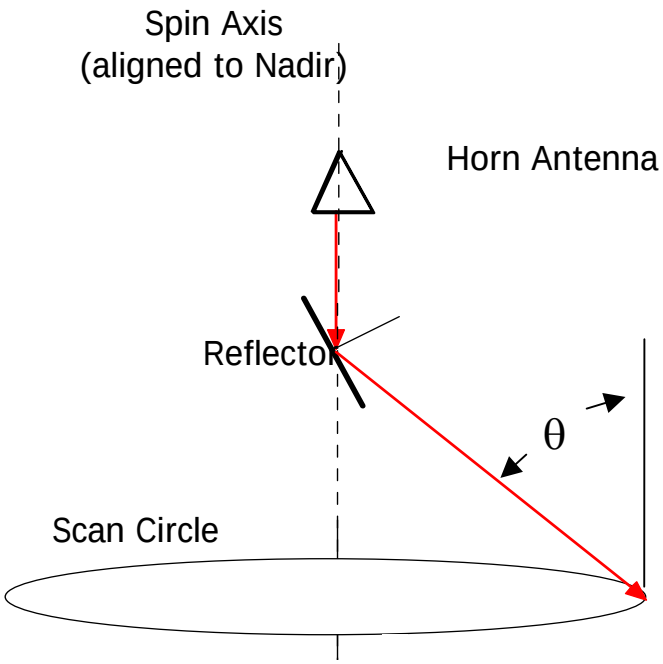

Figure 2.7. C-STAR scanning geometry.

CHAPTER 3: ANALYSIS OF ATTITUDE ERRORS ON MEASUREMENT GEOMETRY

3.1 Effects of Platform Attitude Errors

In microwave remote sensing applications, the goal is to retrieve one or more geophysical parameters that produced the multi-channel radiometer measured Tb's, e.g., ocean wind vectors [11]. Typically the change in Tb, due to a given geophysical parameter, is small (of order degrees); therefore, it is paramount that the brightness temperature be measured as precisely as possible. In an ideal conical scan, the spin axis is aligned to point to the nadir (perpendicular to the surface), and the resulting incidence angle is constant over the entire revolution. In this way, only geophysical changes (not geometry) affect the observed Tb. In practice, however, the initial orientation of the spin axis along with time-varying aircraft roll and pitch, as shown in Fig. 3.1 misaligns the spin axis (relative to nadir), causing variations in the true incidence angle [12, 13].

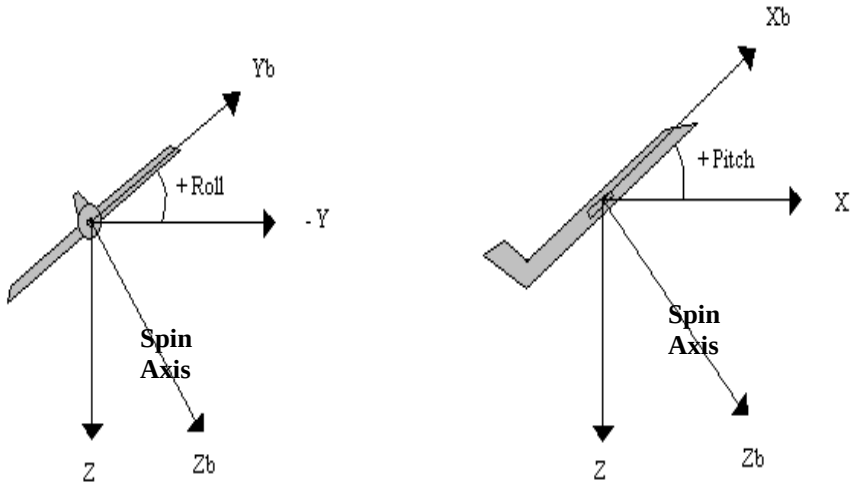

Figure 3.1. Aircraft roll and pitch depicted maneuvers. Left panel is + roll and right panel is + pitch.

The axes X, Y and Z in the above figure define the Earth geocentric coordinate system, and axes Xb, Yb and Zb are the aircraft body coordinates, where the aircraft velocity is in the + X direction. Positive roll is defined as CCW rotation about the +X axis and the roll angle is between the X-Y and the Xb-Yb planes, and it is measured in Y-Z plane. Roll is defined as the angle between the X-Y plane and the Xb-Yb plane and is measured in Y-Z plane. Pitch is defined in a similar manner as roll but is measured in X-Z plane.

3.2 Attitude Effects on Incidence Angle

The orientation of the instrument's spin axis must be aligned to point to nadir in order for the incidence angle to remain constant as the instrument scans in azimuth. Any fixed off-set errors in the alignment of the spin axis or any non-zero roll and/or pitch will contribute to an erroneous incidence angle and measured brightness. Therefore, the incidence angle of a conical scanning instrument is a function of the orientation of the spin axis, the aircraft pitch and roll, and the radiometer antenna azimuth look direction. As the radiometer scans in azimuth, the incidence angle varies as a sinusoid with phase and amplitude dictated by the instantaneous pitch and roll. This can be modeled as [12, 13];

$$\theta_i(pitch, roll, \psi) = \theta_i + pitch * \cos(\psi) - roll * \sin(\psi) \qquad (3.1)$$

Where:

ψ = Antenna azimuth measured clockwise from the forward direction.

Pitch = Aircraft pitch + pitch misalignment in spin axis.

Roll = Aircraft roll + roll misalignment in spin axis.

Plots of eq. 3.1 are shown in Fig. 3.2 for various combinations of assumed pitch and roll. As shown in panel (a), when the roll and pitch values are both zero, the incidence angle is constant over the full azimuth scan range. As the pitch is varied (and roll is kept constant at zero deg), the incidence angle dependence is a cosine function with the peak amplitude equal to the pitch value. In the forward (flight) direction, the pitch adds to the cone angle to increase the incidence; while looking aft the pitch subtracts; and at other scan positions, the incidence varies as the cosine of azimuth. Thus the peak-to-peak variation

in incidence angle is twice the pitch angle for zero roll. In panel (b), as the roll is varied (and the pitch equals zero), the incidence angle behaves as a negative sine function of the azimuth, which is maximum at 270° in azimuth and is minimum at 90°. The effect is that roll is similar to pitch except that the roll-axis is orthogonal to pitch (i.e., rotated by 90° in azimuth). In panel (c), roll is varied for a constant 1° pitch (a typical value during flight), and the result is that the locations (corresponding azimuth positions) of the maximum and minimum incidence angle depend upon the magnitude and sign of the roll.

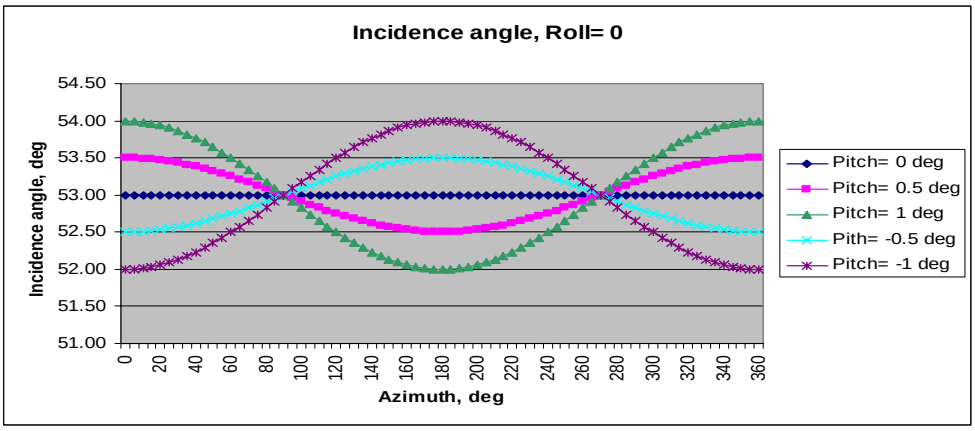

(a)

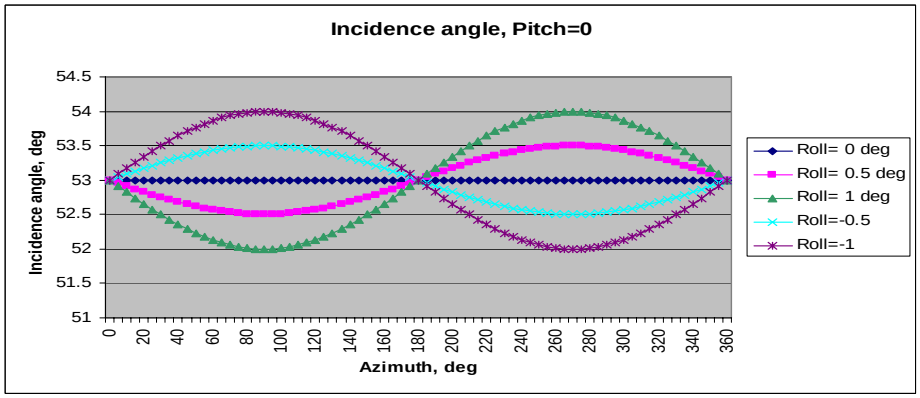

(b)

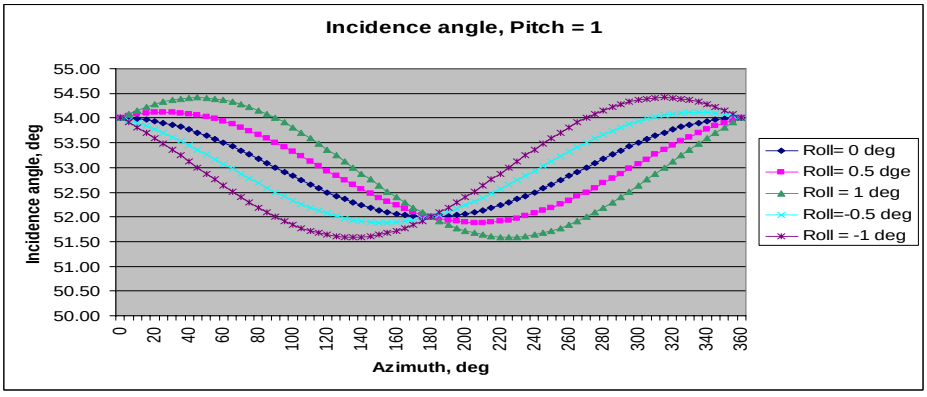

(c)

Figure 3.2 Incidence angle simulation using eq. 3.1 for: (a) zero roll and variable pitch, (b) zero pitch and variable roll; and (c) 1° pitch and variable roll.

3.3 Attitude Effects on Tb

Since the incidence angle is proportional to the measured brightness, a plot of brightness temperature versus azimuth will have a shape similar to those in Fig. 3.2. For V-pol, the Tb increases with incidence angle, and for H-pol the Tb decreases. The Fig. 3.3 below illustrates a comparison between the incidence angle and the measured brightness for a selected group of five scans for clear sky atmospheric conditions. The figures to the left represent the calculated incidence angle (eq. 3.1) while those to the right represent the measured Tb. The top two are the fwd scenes and the bottom two the aft scene. In this case, the average roll = 1.0 deg and the average pitch= 1.0 deg; and this results in very similar incidence angle and Tb curves versus azimuth.

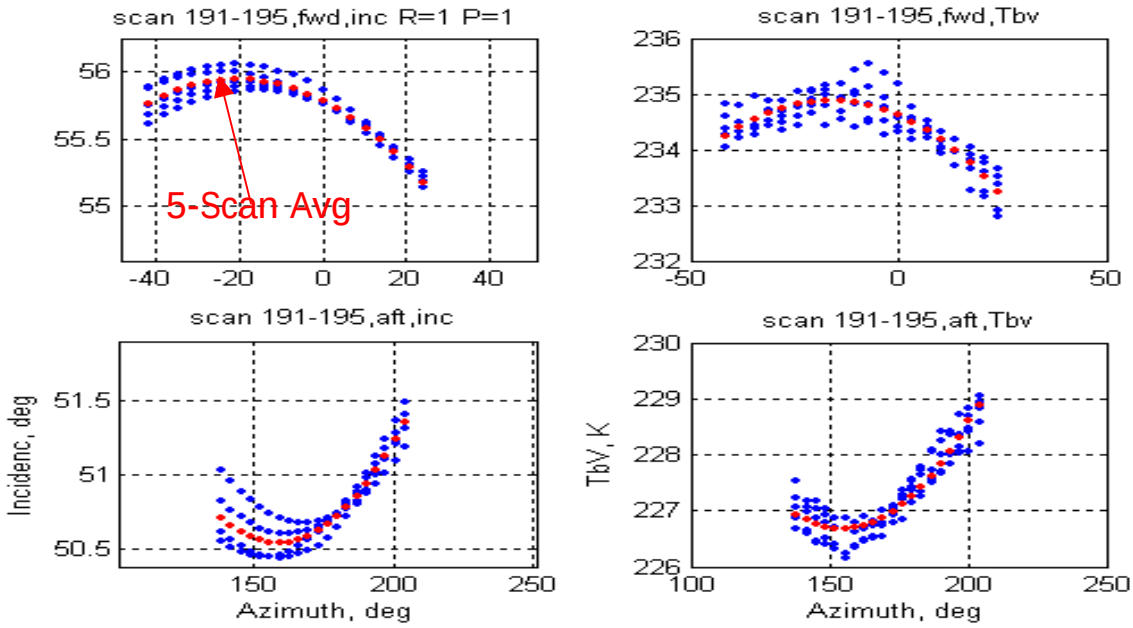

Figure 3.3 Incidence angle comparison to measured brightness temperature for roll and pitch biases of one. Scans 191-195.

3.4 Theoretical Tb Models

Our objective is to model systematic variations in the observed brightness due to aircraft attitude errors. This Tb model, in the presence of non-zero roll and pitch, will provide a means of accounting for variations in incidence angle and polarization rotation effects; thereby, making it possible to compensate the measured Tb and produce the equivalent Tb that would have been observed from a "perfect conical scanner" (without attitude error).

The general equation used to model the apparent brightness temperature for the four C-STAR polarizations (H-pol, V-pol, P-pol, or Q-pol) is given in eq. 3.2.

$$Tb = Tbh(\theta_i) * \cos^2(\beta) + Tbv(\theta_i) * \sin^2(\beta) \qquad (3.2)$$

Where,

Tbv and *Tbh* = the apparent horizontal and vertical brightness temperature measured at the aircraft altitude.

β = Orientation of the antenna electrical field

Using the radiative transfer model discussed in chapter 2, the apparent brightness temperature is modelled by:

$$Tbv = Tbv_{Atmos}(Az) + Tbv_{atmos}(Az) * \Gamma_v(\theta_i) * \tau + Tbv_{surface} * \tau + \frac{dTbv}{d\theta} * \Delta\theta_i \quad (3.3)$$

$$Tbh = Tbh_{Atmos}(Az) + Tbh_{atmos}(Az) * \Gamma_h(\theta_i) * \tau + Tbh_{surface} * \tau + \frac{dTbh}{d\theta} * \Delta\theta_i \quad (3.4)$$

where,

Tb_{atmos} is the upwelling or downwelling atmospheric brightness temperature that are assumed equal and allowed to vary with azimuth look direction

Γ is the sea surface power reflection coefficient, which varies with polarization, incidence angle and wind speed, but assumed to be isotropic (independent of azimuth look direction)

τ is the atmospheric transmission coefficient which varies with wavter vapor and clouds but is assumed to be isotropic

$dTb/d\theta$ is the rate of change of Tb with incidence angle (derived from radiative transfer theory)

$\Delta\theta$ is the difference between the instantaneous incidence angle and the nominal incidence angle (53 deg)

The four polarizations of C-STAR are illustrated in Fig. 3.4 where the angular orientation of the electric field of the radiometer antenna (β) determines its polarization. For example, H- and V-polarizations are orthogonal polarizations that are simultaneously produced by a single horn feed with an orthomode transducer. The C-STAR antenna is aligned (by mechanically rotating the antenna) to cause the V-pol electric field lie in the incident plane. This is vertical polarized at the surface, which corresponds to $\beta = 90$ deg. The orthogonal polarization produced by this feed is horizontally polarized, which corresponds to a $\beta = 0$ deg. To obtain the P and Q polarizations, β is set to be 45 deg, by physically rotating a second horn by 45 deg clockwise. This allows mixing of the H and V polarized Tb surface emissions.

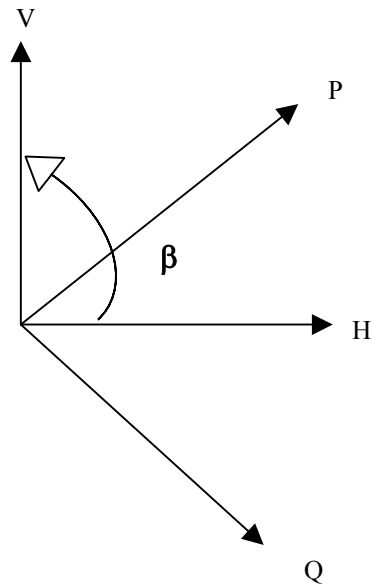

Figure 3.4 C-STAR antenna polarizations.

For the realistic case of non-zero roll and pitch, the β angle is also a function of roll and pitch and azimuth look direction as defined by

$$\beta = (\phi + \varepsilon) + \gamma \tag{3.5}$$

Where,

Φ = *0 for H, 90 for V, 45 for P, and -45 for Q*

ε = *antenna alignment error*

γ = *Polarization rotation angle (PRA)*

$$\gamma = roll * \cos(Az) + pitch * \sin(Az) \tag{3.6}$$

The polarization rotation angle plotted in Fig. 3.5 is similar to the equation developed for incidence angle (Fig. 3.2) in that the amplitude is controlled by the magnitude of the roll and pitch while the phase is control by the relative amplitudes of roll and pitch.

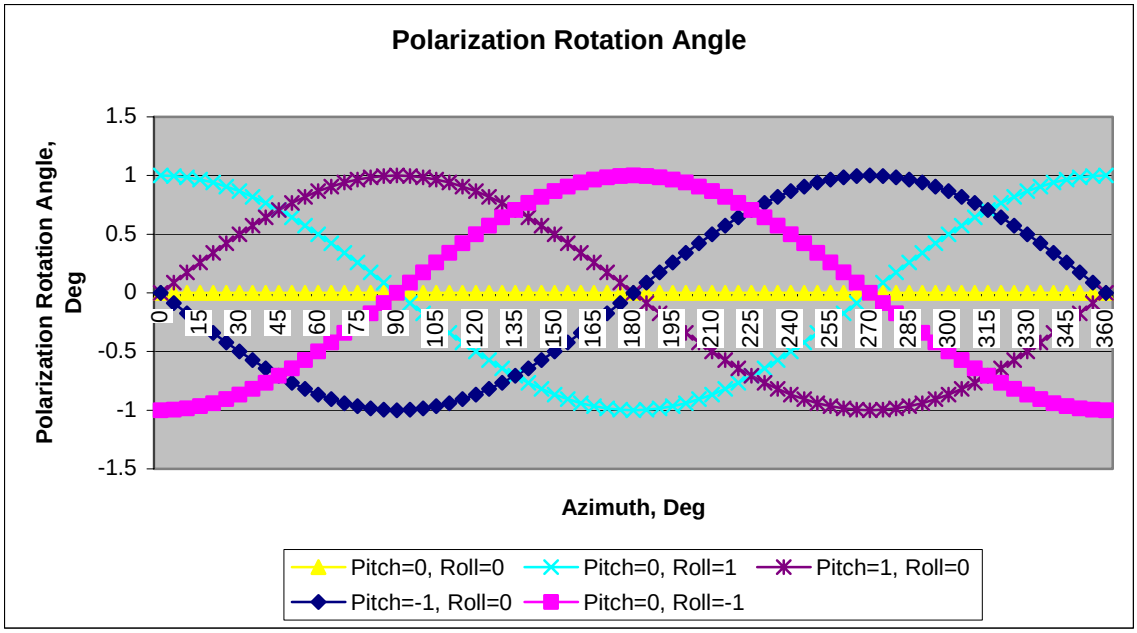

Figure 3.5 Polarization Rotation Angle

For the case where pitch and roll are both equal to zero, the PRA is zero as would be expected. When roll is zero and pitch non-zero, the PRA becomes a sine wave with amplitude equal to the pitch value. If the pitch is held zero and the roll non-zero, the PRA curve becomes a cosine wave with amplitude equal to the value of the roll. If the polarities are reversed, the same observations are made in a negative sense.

3.5 H- and V-polarization Tb Models

Typical roll and pitch values range between ± 2 deg; so a worst case value of roll and pitch combined is PRA ~ 3 deg. Assuming the antenna is properly aligned and using 3.0 deg for γ in eq. 3.5, we calculate the modelled brightness temperature using equation 3.2 for all polarizations. The result is that the polarization rotation has little effect on the

vertical and horizontal Tb's; but it has a significant effect on the P- and Q-polarizations. For example, we model the vertical brightness for a PRA of 3 deg and using typical values of "true" vertical Tbv = 220 K and horizontal Tbh = 170 K. The first term of eq. 3.2 (cross polarization) contributes 0.5 K, while the second term (dominant polarization) contributes 219.4 K, for a total brightness of 219.9 K, which is an error of ~ 0.1 K too low. For H-pol apparent Tb, the first term (dominant polarization) contributes 169.5 K, while the second term adds 0.6 K. For the P pol, the first term adds 76.1 K while the second term adds 121.5 K for a total of 170.1 K, which is also ~ 0.1 K error too high. Based upon these negligible modeling errors, the effect of PRA is neglected in the calculation of H- and V-pol Tb's. For the P- and Q-pol Tb's, both terms are nearly equal and must be used with the PRA to accurately model the brightness temperature.

Based on these observations, our models for the vertical and horizontal polarizations reduce to:

$$Tbv = Tbv_{Atmos}(Az) + Tbv_{atmos}(Az) * \Gamma_v(\theta_i) * \tau + Tbv_{surface} * \tau + \frac{dTbv}{d\theta} * \Delta\theta_i \quad (3.7)$$

$$Tbh = Tbh_{Atmos}(Az) + Tbh_{atmos}(Az) * \Gamma_h(\theta_i) * \tau + Tbh_{surface} * \tau + \frac{dTbh}{d\theta} * \Delta\theta_i \quad (3.8)$$

In the above equations, τ represents the atmospheric transmissivity, which is estimated from radiative transfer theory using satellite observations of water vapor. The sea surface power reflectivity's for V- and H-pol, Γ, are estimated using Fresnel

reflection theory described in chapter 2 and the estimated dielectric properties of sea water. Both τ and Γ are determined for given environmental conditions. SST is the sea surface temperature, which is estimated from satellite observations and $\Delta\theta_i$ is simply the difference between the mean and the instantaneous incidence angle.

In eq. 3.7 (and 3.8), the first term is the upwelling atmospheric brightness and the second term of the downwelling atmospheric brightness that is scattered by the sea surface and attenuated by the atmosphere. The third term adds the isotropic brightness temperature of the sea surface that is attenuated by the atmosphere. This parameter is a estimated constant, which affects only the DC level of the modelled brightness. During modeling the C-STAR Tb's, it is adjusted to improve the measured and modelled comparison. The last term of eq. 3.7 adds the contributions due to the aircraft roll and pitch variations as described in section 3.1. For a known set of environmental conditions, the change in Tb with respect to incidence angle (dTb/dθ) can be estimated using radiative transfer theory [6, 8] or from empirical observations of the measured Tb correlated with the instantaneous incidence angle. Knowledge of the slope (dTb/dθ) can then be applied to account for variations caused by aircraft attitude changes.

The atmospheric brightness, Tb_{atmos}, is most difficult to determine because of the transient nature of clouds; therefore, we developed an iterative procedure to estimate this quantity from the C-STAR measured Tb's. This is calculated at each azimuth position using eq. 3.9 (or 3.10) by subtracting the sea surface brightness (SST*{1 – Γ}) from the observed brightness that has been normalized (corrected) for incidence angle variations, Tb_{norm} .

$$Tbv_{Atmos}(Az) = \frac{Tbv_{norm}(Az) - SST * (1 - \Gamma_v)}{1 + \tau * \Gamma_v} \tag{3.9}$$

$$Tbh_{Atmos}(Az) = \frac{Tbh_{norm}(Az) - SST * (1 - \Gamma_h)}{1 + \tau * \Gamma_h} \tag{3.10}$$

3.6 P- & Q-Polarization Tb models

As explained in the previous section, the P (+45) and Q (- 45) polarizations are obtained by mixing the H and V polarization through a rotation of the radiometer antenna by 45°. Since the effects of polarization rotation is significant, the equation used to model the P and Q are the form of eq. 3.2. The P polarization is obtained by setting ϕ = + 45 deg in equation 3.5; and setting ϕ = – 45 for the Q polarization, as are shown below:

$$Tbp = Tbh(\theta_i) * \cos^2(\beta_{+45}) + Tbv(\theta_i) * \sin^2(\beta_{+45}) \tag{3.11}$$

$$Tbq = Tbh(\theta_i) * \cos^2(\beta_{-45}) + Tbv(\theta_i) * \sin^2(\beta_{-45}) \tag{3.12}$$

where,

$$Tbv(\theta_i) = Tbv_{Atmos}(Az) + Tbv_{atmos}(Az) * \Gamma_v(\theta_i) * \tau + Tbv_{surface} * \tau \tag{3.13}$$

$$Tbh(\theta_i) = Tbh_{Atmos}(Az) + Tbh_{atmos}(Az) * \Gamma_h(\theta_i) * \tau + Tbh_{surface} * \tau \tag{3.14}$$

$$\beta_p = (45 + \varepsilon) + \gamma \tag{3.15}$$

$$\beta_q = (-45 + \varepsilon) + \gamma \tag{3.16}$$

$$\gamma = roll * \cos(Az) + pitch * \sin(Az)$$

The ϕ terms represent the effective angular rotation of the horn antenna, and the γ term represents the error due to the angular rotation of the H- and V-polarizations caused by roll and pitch as shown in Fig. 3.6, which is the polarization rotation angle.

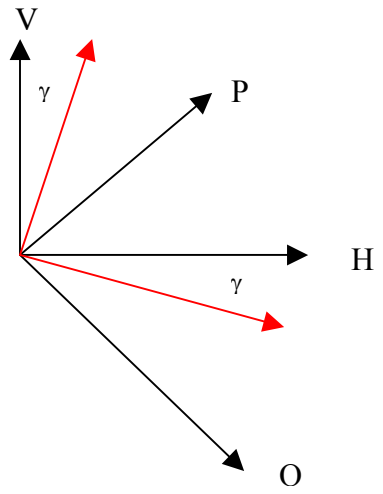

Figure 3.6 Polarization rotation

The models developed in this chapter could not be directly be used to simulate the measured brightness due to various factors that influence the accuracy of the models. In the following chapter, we first present data processing and quality control (QC) procedures adopted to remove unwanted effects and the present comparisons of the developed models against actual measured brightness temperatures.

CHAPTER 4: EXPERIMENTAL VALIDATION

The evaluation of the brightness temperature model is made through comparison with experimental measurements made by the C-STAR under a wide variety of measurement conditions. Given the measured aircraft attitude data (pitch and roll) and radiometer data (antenna azimuth position), it should be possible to accurately model the observed (C-STAR) Tb's, subject to estimating "unknown" environmental atmospheric and oceanic surface conditions. Unfortunately, this last necessary condition is often difficult to satisfy; so the challenge to validation is to select suitable cases where there is reasonable confidence in the estimated environmental parameters. Fortunately, there are some independent estimates of environmental conditions from satellite microwave radiometers [14]; although they are not coincident with the aircraft flights and have very coarse resolution (compared to the aircraft radiometer measurements). Never-the-less, for benign weather conditions (calm sea and clear sky) associated with high pressure weather systems, these satellite measurements are adequate to assure that nearly uniform conditions exist. So in this chapter, a number of selective cases are presented for comparison of measured and modelled Tb (at the top of the atmosphere). These cases range from "uniform" clear sky and calm sea surface winds to more difficult hurricane conditions associated with strong winds and heavy (heterogeneous) clouds.

Thus, the fidelity of the model will be demonstrated, by producing consistent time series of Tb's, under a variety of flight and environmental conditions, that are highly correlated with actual C-STAR measurements. In this chapter, we present these selected

comparisons between C-STAR and modelled results as well as other quality control or processing procedures used to select the comparison set.

4.1 C-STAR Time Bias Anomaly

As described in Chapter-2, scene data is collected by the C-STAR over two 90 degrees azimuth ranges in the forward and aft antenna look directions, each of which occurs during a 2.5 sec period [10]. In each scene, there are 26 azimuth pixels that are sequentially sample every 96.154 ms. To calculate the instantaneous incidence angle, the aircraft attitude (roll and pitch) must be well synchronized to the radiometer antenna azimuth position. Any misalignment would result in erroneous incidence angles associated with measured temperature. The aircraft navigation and C-STAR radiometer data are recorded on two separate data systems and then merged for processing earth-located Tb's. Since both systems made use of a scan counter to record the radiometer scan number; it was assumed that there were synchronized in time. Unfortunately, this later proved to be false and a significant time bias was discovered. This section presents the results of this investigation.

As explained in chapter three, the brightness temperature measured by a radiometer is a function of incidence angle. The incidence angle is a function of aircraft roll, pitch and radiometer azimuth; and as the incidence angle increases, so does the vertical brightness, while that of the horizontal decreases. To minimize the possibility Tb changes were caused by environmental changes, a C-STAR flight was selected which occurred under nearly clear sky conditions and light surface winds. A special quality

control (cloud editing) procedure was developed and applied to the C-STAR data as described in the next section 4.2).

In determining the existence of a time misalignment, we examined forward and aft Tb scans separately during periods when the aircraft experienced large changes in roll from one polarity to another. For example, when looking forward, the slope of Tb versus azimuth position increases directly proportional to positive roll as does the Tb dynamic range. Similarly, a negative roll will result in a proportional negative slope (dynamic range) of the measured brightness. When the roll is approximately zero, the measured brightness versus azimuth is symmetric (parabolic) about the 0 deg (or 180 deg) azimuth position. A temporal misalignment (of roll /pitch and azimuth) is noted in the pattern of the measured Tb's not agreeing with the polarity of the associated recorded roll as the aircraft goes from a positive to negative roll or vice versa.

In figure 4.1, we show the modelled and observed vertical Tb (upper panel) along with the corresponding aircraft roll and pitch (lower panel). In this figure, each section of 26 points (x-axis) represents one scan of the forward scene (aft scans omitted), which consists of measurements taken +/- 45 deg about an azimuth of 0 deg. For this group of scans, the aircraft pitch is nearly zero and constant; therefore any variations in the Tb are due to incidence angle changes with roll. A careful examination of the shapes of the brightness temperature curves shows that they do not agree with the corresponding roll values. The most noteworthy disagreement is for the third scan where the measured and modelled slopes are opposite, which we believe is the result of an apparent time misalignment. Since the aircraft data is recorded once every second, there exists a

possibility to realign the two data keeping systems by systematically adding a time bias (integer samples) to the aircraft data until measured and modelled Tb's agrees well.

Figure 4.2 illustrates the case where we have delayed the aircraft data to achieve such an agreement. Note that in figure 4.2a, the measured Tb does not change; but the modelled Tb does change as a result of the delay in the roll and pitch values associated with each scan. By comparing fig. 4.2a and fig. 4.2b, it is observed that before the roll changes polarity, the measured Tb has a negative slope. Afterwards, when the roll is positive, the slope of the brightness is reversed to be positive. Based on the above observations, we conclude that the aircraft data (roll and pitch) must be realigned to the radiometer data (azimuth) by adding a delay of 11 seconds; which is equal to one full scan(10 sec) plus one aircraft sample.

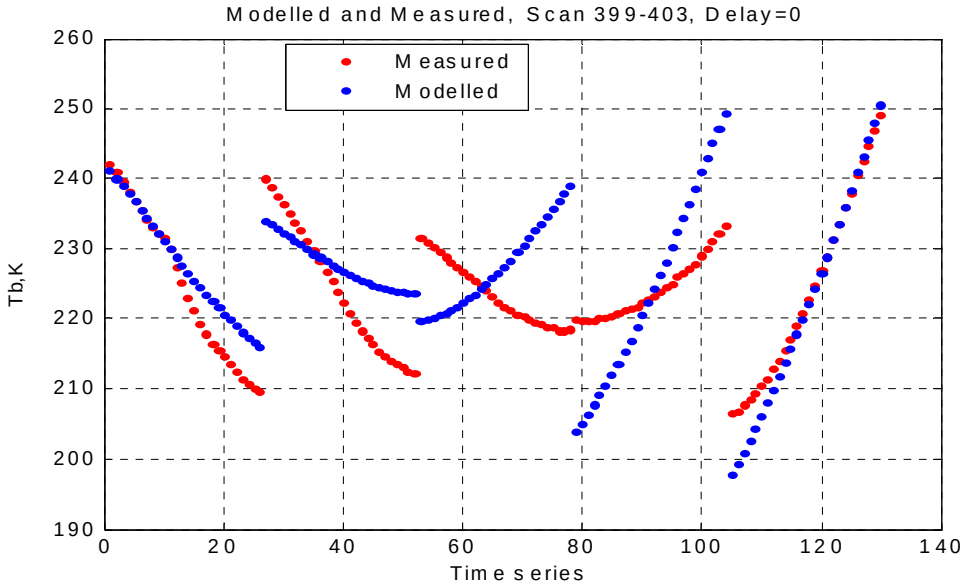

(a)

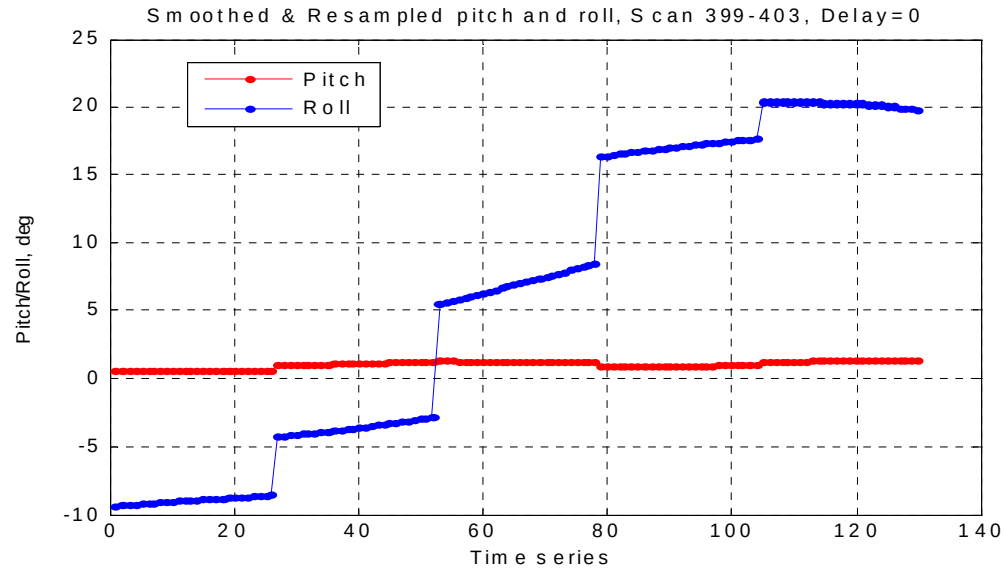

(b)

Figure 4.1 (a) Modelled and measured vertical Tb for FWD scene, scan 399-403 (b) Corresponding aircraft roll and pitch.

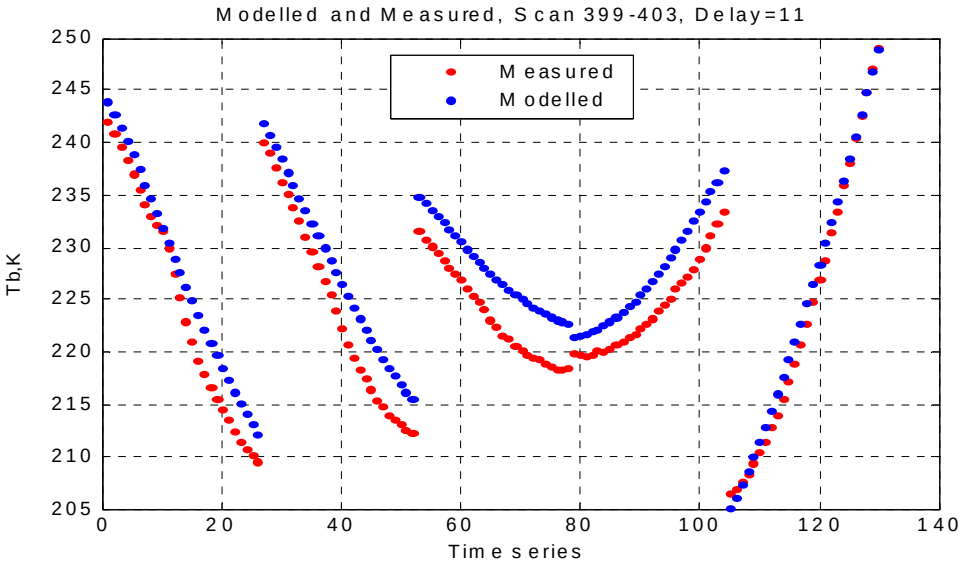

(a)

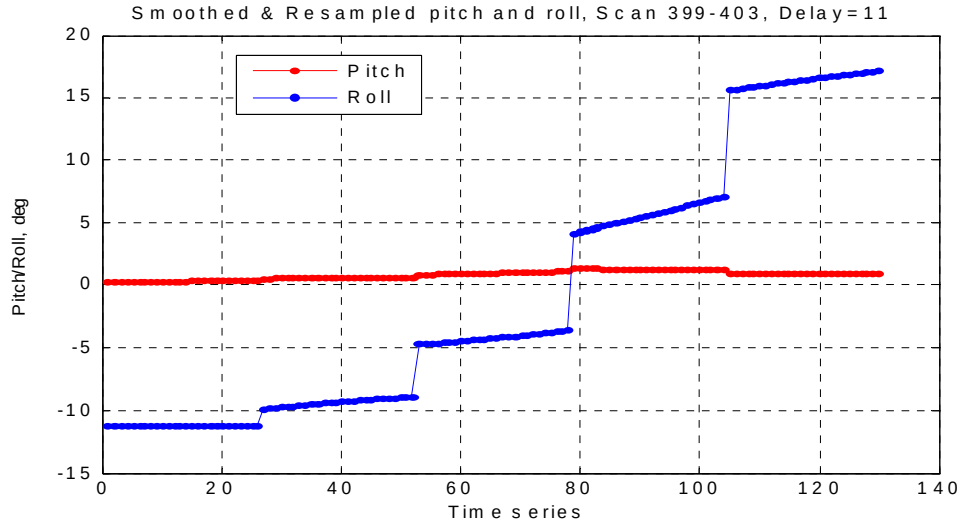

(b)

Figure. 4.2 (a) Modelled and measured vertical Tb for FWD scene, scan 399-403 (b) Corresponding aircraft roll and pitch delayed by 11 seconds.

This empirical evaluation of time bias was preformed a number of times under differing conditions to assure that the best correlation occurred for the same (fixed) time offset. Next are comparisons for scans 931 through 937. Aft scans are presented in Fig. 4.3 (no time bias) and 4.4 (11 sec time bias); and corresponding forward scans are presented in Figs. 4.5 and 4.6. Additional comparisons are given if Fig. 4.7 and 4.8 for scans 1029 through 1034 for the forward scene. Thus a consistent time bias of 11 seconds was adopted and used for the remainder of the comparisons presented herein.

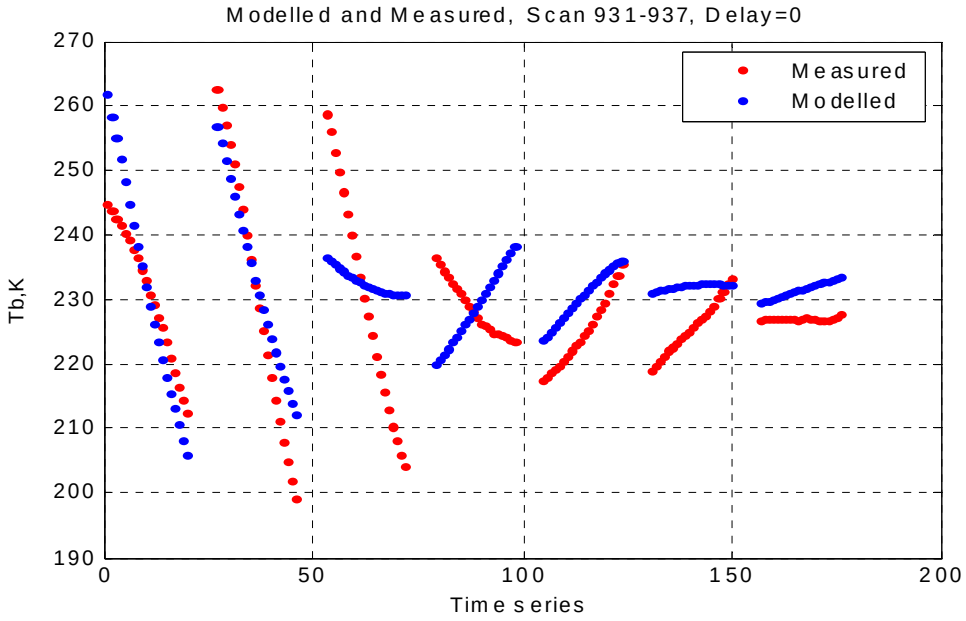

(a)

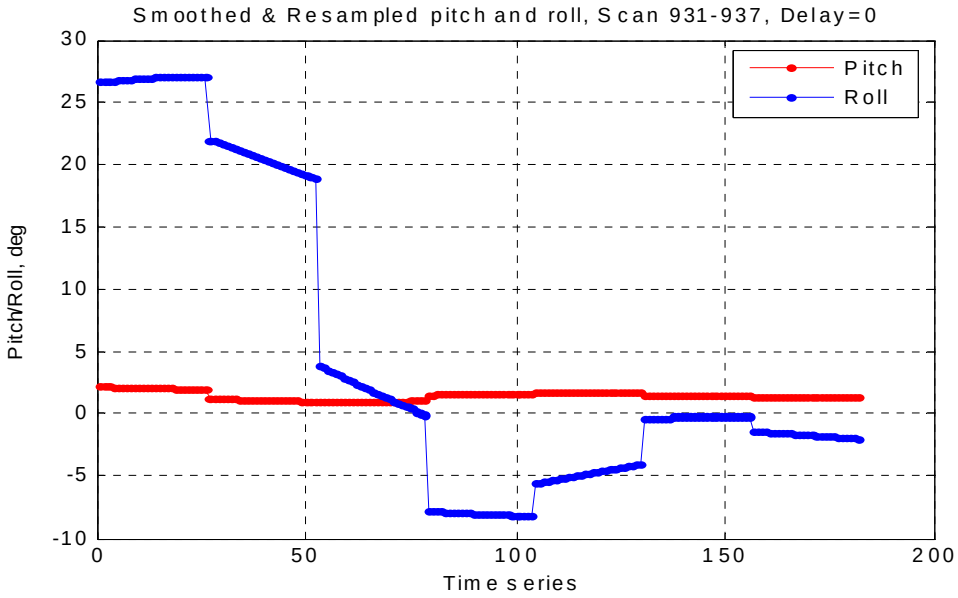

(b)

Figure. 4.3 (a) Modelled and measured vertical Tb for AFT scene, scan 931-937 (b) Corresponding aircraft roll and pitch delayed by 0 seconds.

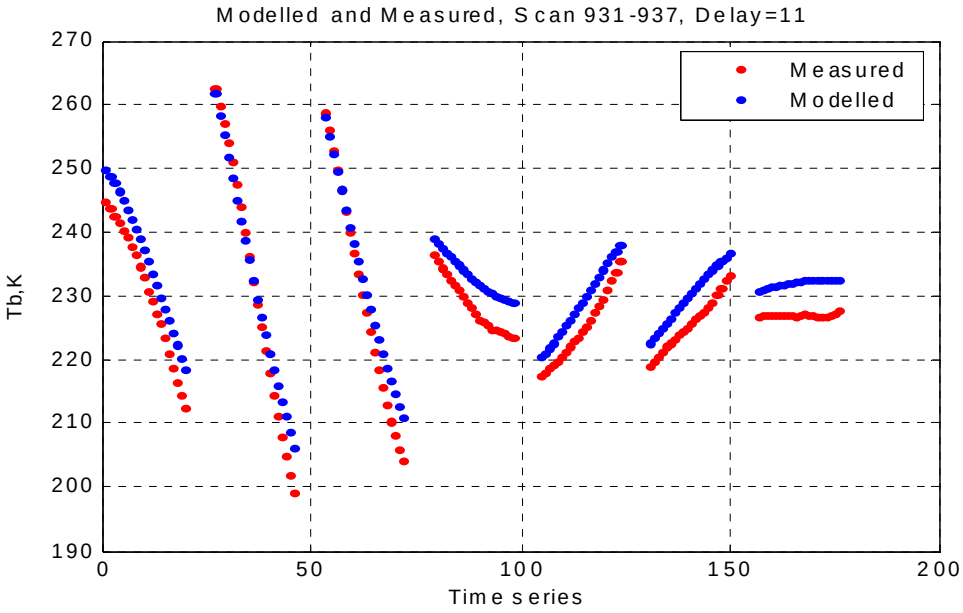

(a)

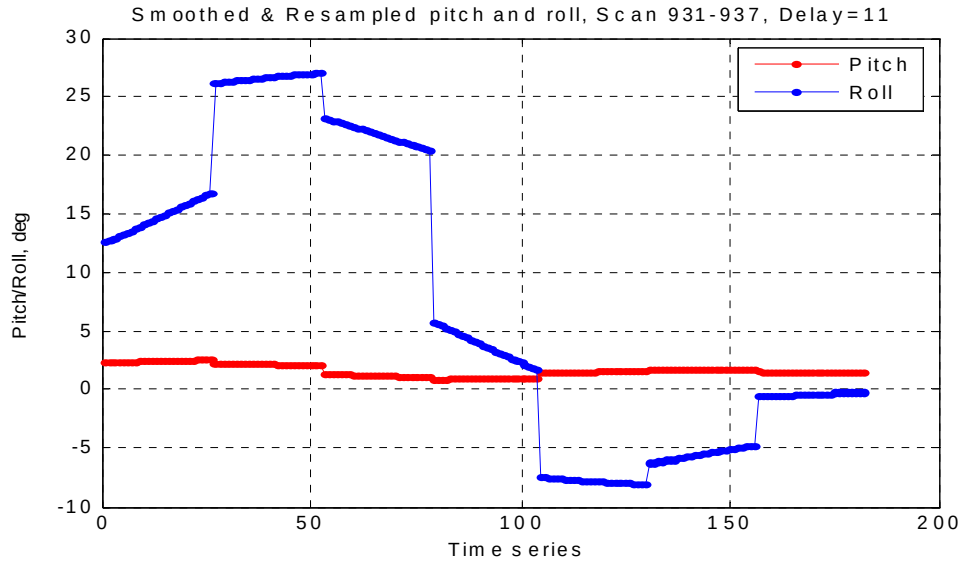

(b)

Figure. 4.4 (a) Modelled and measured vertical Tb for AFT scene, scan 931-937 (b) Corresponding aircraft roll and pitch delayed by 11 seconds.

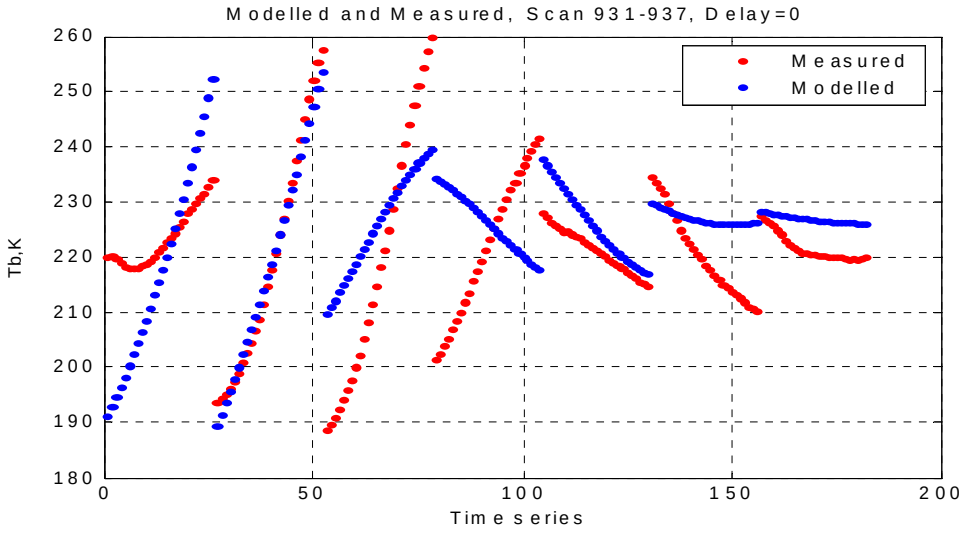

(a)

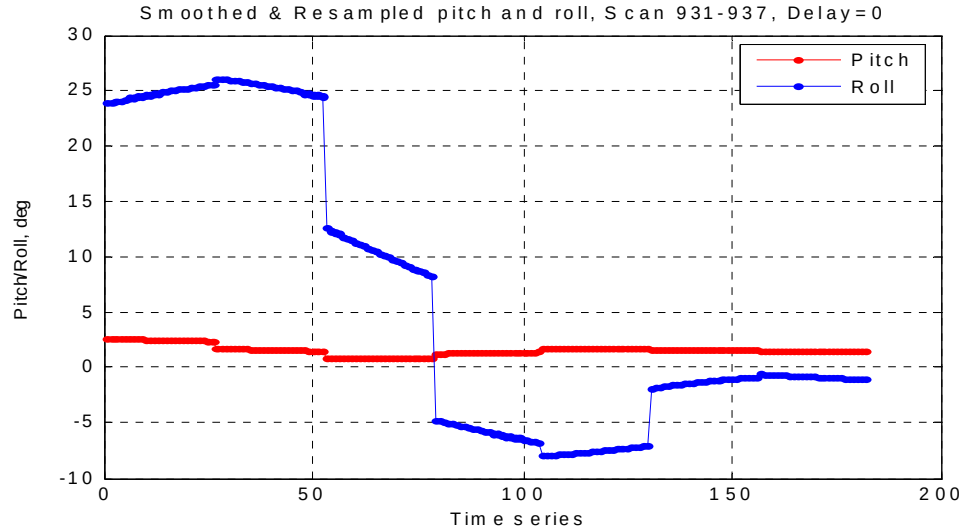

(b)

Figure 4.5 (a) Modelled and measured vertical Tb for FWD scene, scan 931-937 (b) Corresponding aircraft roll and pitch delayed by 0 seconds.

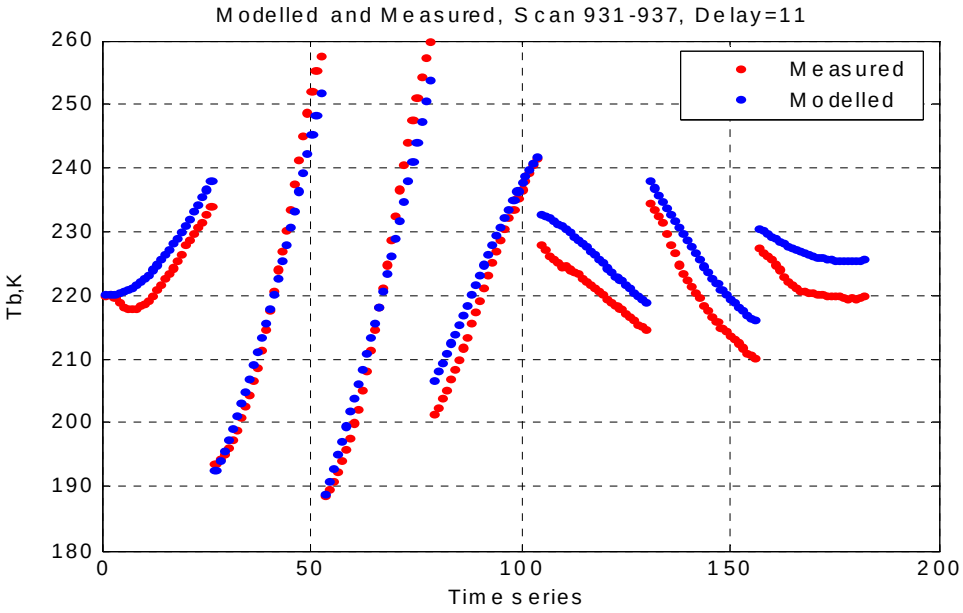

(a)

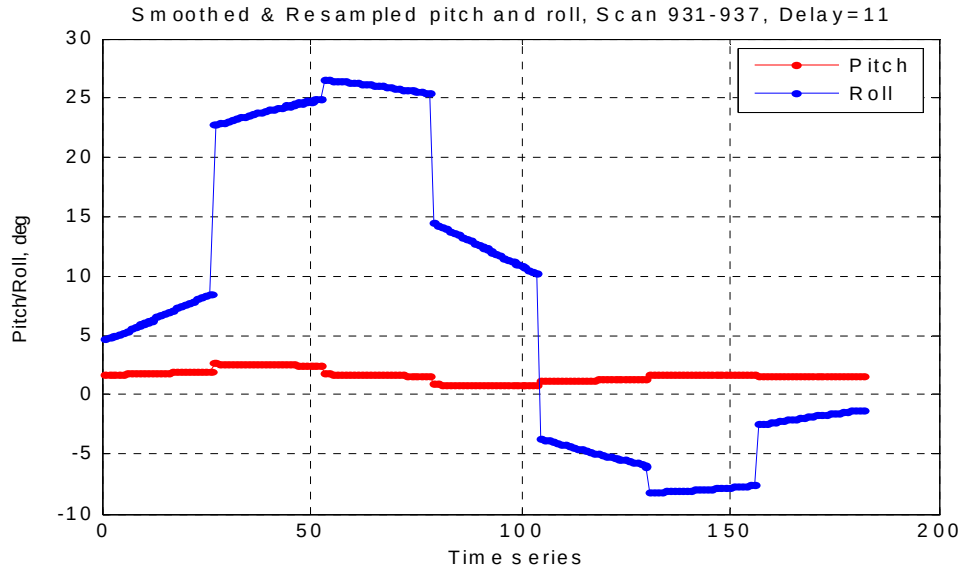

(b)

Figure. 4.6 (a) Modelled and measured vertical Tb for FWD scene, scan 931-937 (b) Corresponding aircraft roll and pitch delayed by 11 seconds.

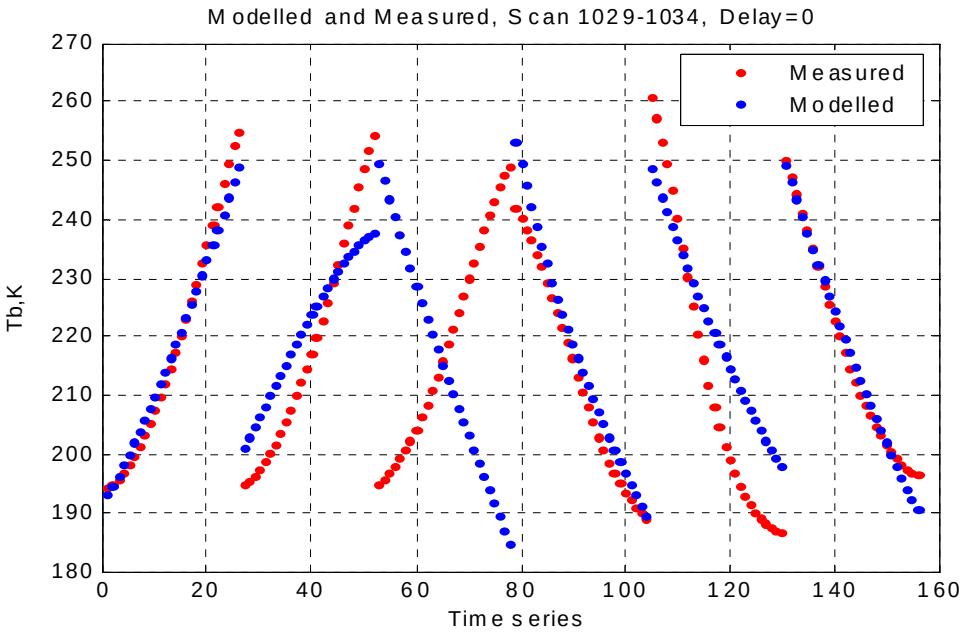

(a)

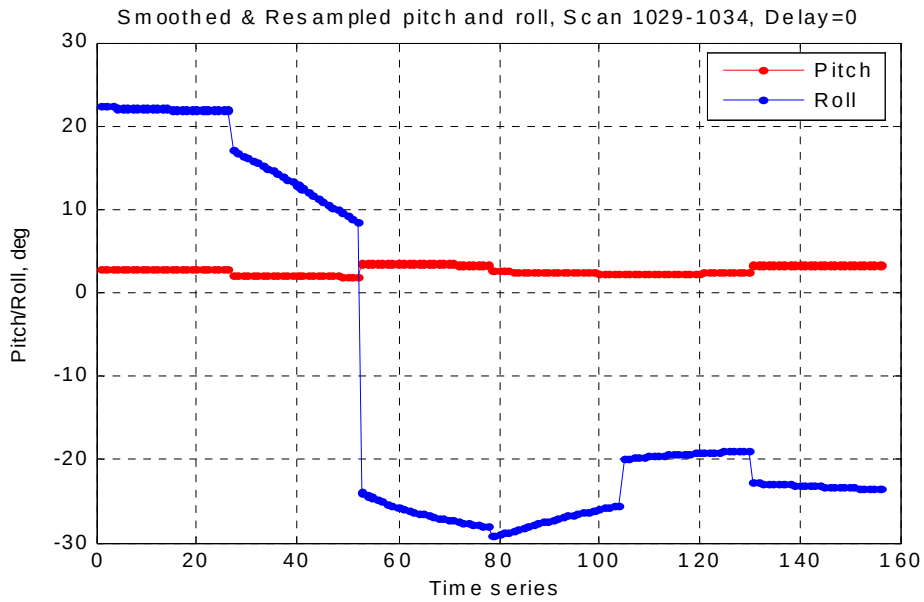

(b)

Figure 4.7 (a) Modelled and measured vertical Tb for FWD scene, scan 1029-1034 (b) Corresponding aircraft roll and pitch delayed by 0 seconds.

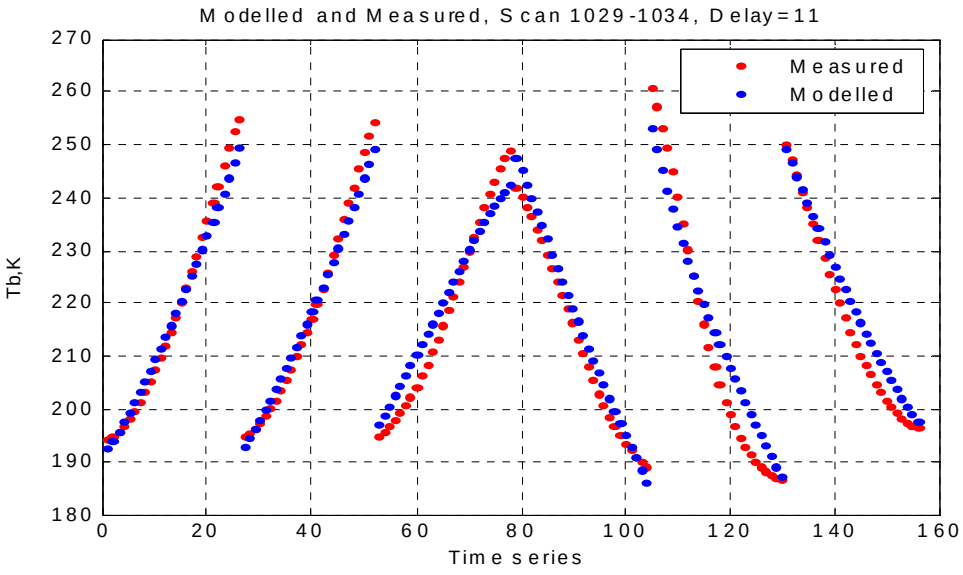

(a)

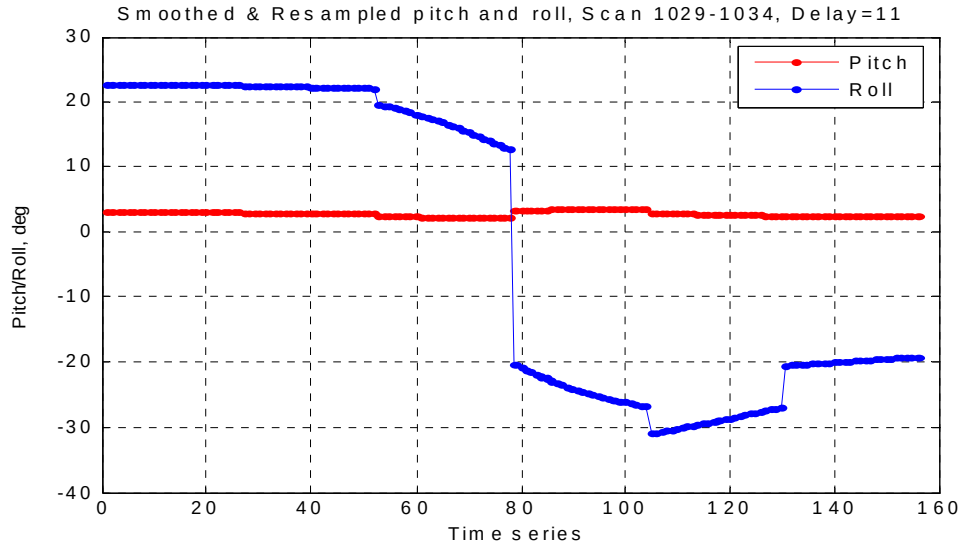

(b)

Figure. 4.8 (a) Modelled and measured vertical Tb for FWD scene, scan 1029-1034 (b) Corresponding aircraft roll and pitch delayed by 11 seconds.

4.2 Cloud Editing Procedure

As described in chapter 1, the measured brightness is the sum of the contributions of the ocean surface and the atmosphere; however the pertinent environmental (geophysical) conditions are not measured during the C-STAR flights. Since these geophysical parameters are not known, the most important question is; Are they uniformly distributed is space? If so, then they produce a constant Tb bias (independent of azimuth position), which is clearly separable from the variable effects of aircraft roll and pitch with azimuth. Therefore, for selected "fair weather" conditions, some parameters (sea surface temperature, ocean surface wind speed and atmospheric water vapor) are well observed by microwave sensors on polar-orbiting weather satellites and can be estimated with a reasonable degree of confidence [7, 14]. Only clouds (cloud water droplets and precipitation) are a major concern because of their heterogeneous nature and dynamic changes in time.

During the C-STAR flights, a quality contral (QC) procedure was applied to remove cloud-contaminated observations. For cloud QC, we develop an algorithm based on the difference between the measured H and V polarizations. Without significant clouds, the difference between the H and V brightness is > 50 K. Under cloudy conditions, the both the H and V brightness increase, but the Tb of H polarization experiences a much greater increase than the V-pol Tb. This fact allows us to remove non-uniform cloud cover by observing the difference of the H and V brightness and noting where that difference falls below 50 K threshold.

In figure 4.9, we illustrate the V and H brightness difference for the FWD scene with cloud cover present for scans 173 – 180. Note that the red line and bars denotes the

mean and standard deviation of the brightness respectively over these azimuth scans. By observing the vertical spread of Tb, we can clearly identify the locations where we have cloud cover. –Based upon these observations, a cloud editing QC procedure was developed as presented in Fig. 4.10. Here, we have plotted the brightness temperature difference for a given azimuth (+31 deg) and set the threshold for > 50 K as acceptable "no-cloud" cases.

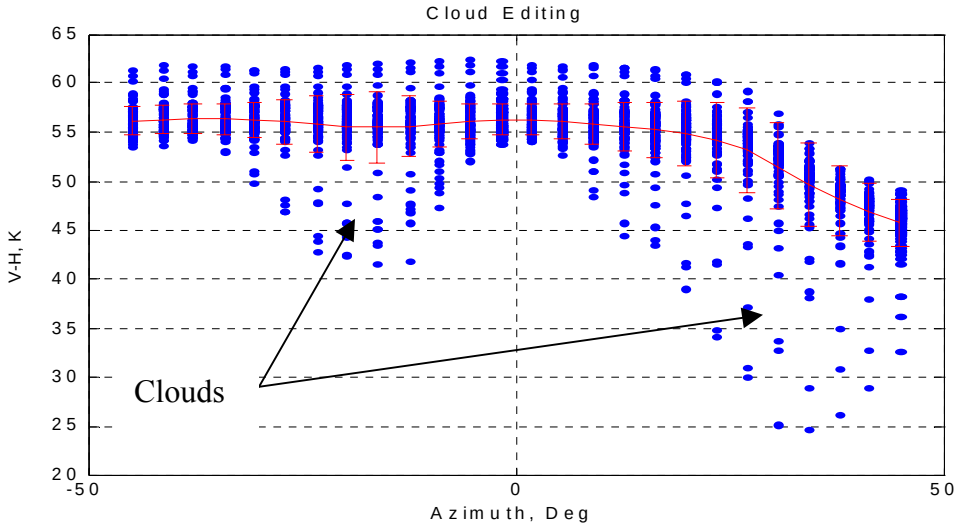

Figure 4.9 V minus H differential Tb for FWD scene, scan 180-280

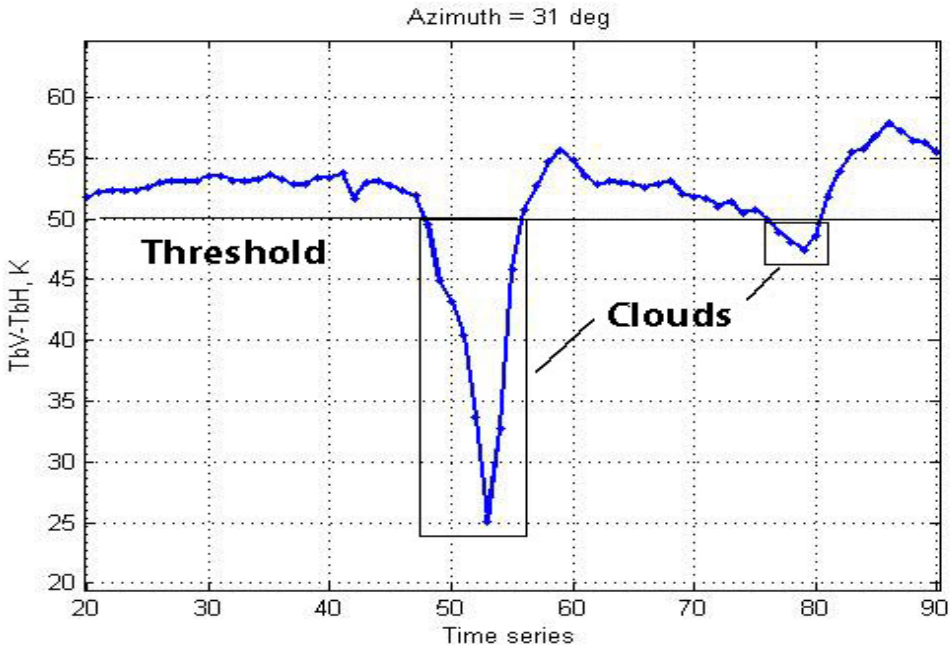

Fig 4.10. Example of cloud editing QC procedure for azimuth=31 deg (FWD scene).

4.3 Anomalous Forward Brightness Temperatures

By examining numerous forward azimuth scans of versus azimuth, it was observed that there was a systematic change in brightness temperature at the last six azimuth positions (Fig. 4.11). For the vertical polarization the Tb decreased rapidly; and for horizontal, it increased for the corresponding azimuth positions. Such a behavior is abnormal because, for low values of roll and pitch and under clear sky and calm surface wind environmental conditions, the expected Tb over azimuth is isotropic (constant over azimuth). The reason for this behavior is unknown; but a possible explanation may be that the radiometer antenna intercepts the aircraft's fuselage.

For all further analysis presented in this chapter, these azimuth locations are removed. Observations on measurements from the aft scene showed expected behavior therefore, no aft azimuth locations were removed

.

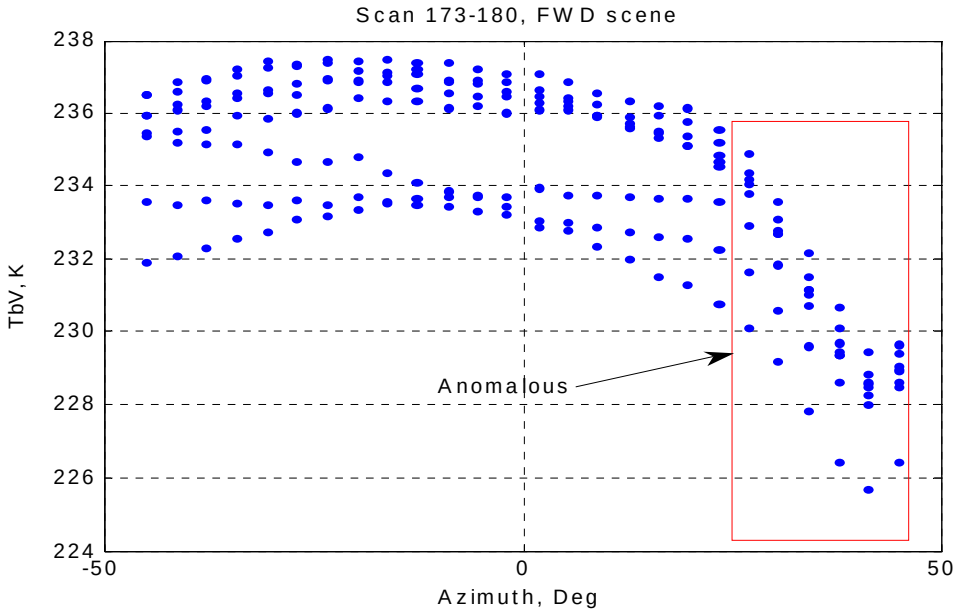

(a)

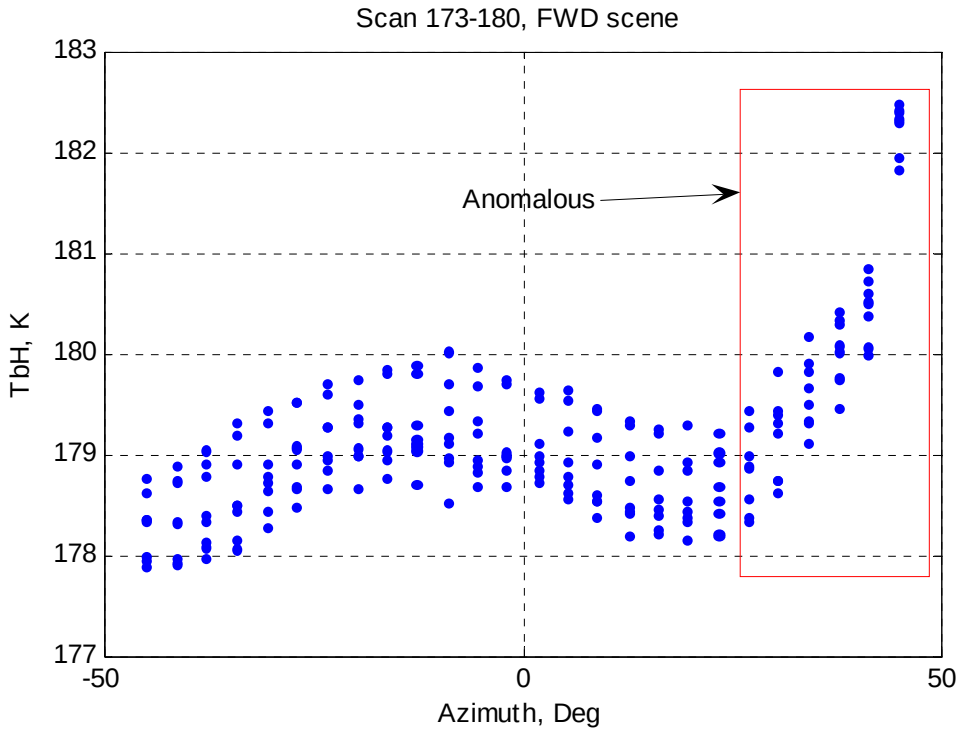

(b)

Fig. 4.11. Measured Tb anomaly (a) V Polarization (b) H polarization.

4.4 Aircraft Attitude Data Resampling

The validation of our model consists of comparisons of the measured and model brightness temperatures for numerous portions of flight trajectories. The models described in chapter 3 are the ones applied; but before the Tb's are modelled, further data processing is required on the aircraft attitude data. It is stated in chapter 2 that the aircraft attitude data are recorded once/sec, while independent radiometer Tb's are recorded every 96 msec. This poses a problem for modeling Tb because the instantaneous aircraft attitude data are not available at each azimuth position. Further, the change in roll and pitch are appreciable between the one-second samples; therefore these parameters must be estimated by using an interpolation procedure, which smoothes and resamples these aircraft data.

Smoothing is required because when the aircraft records a roll or pitch value, it is quantized (0.1 deg least significant bit step) during analog to digital conversion. Thus, smoothing provides a way of producing roll and pitch values that are more representative of the true instantaneous aircraft attitude. This is accomplished by employing a digital signal processing (DSP) technique of a moving averaging window that consists of a window of odd number of elements on which an average is calculated and assigned to the center data sample. As the window moves through the data samples, a new average is calculated each time. The end result is a smoothing effect that removes "step changes" within the data, which is equivalent to low pass filtering. The resampling technique uses linear interpolation methods to provide the required number of data points which is 26 per scene observation. An example of smoothed and resampled data for scan 183 is shown in figure 4.12.

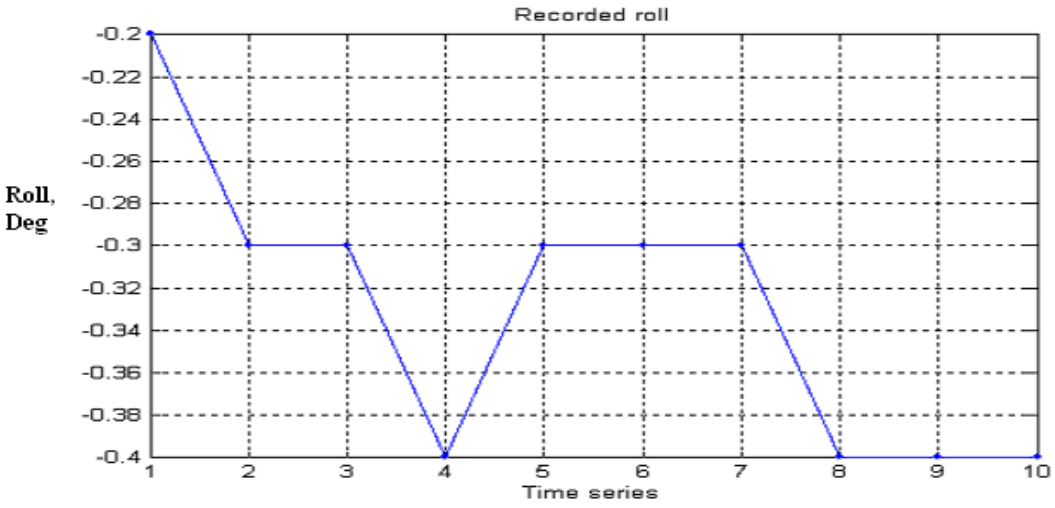

(a)

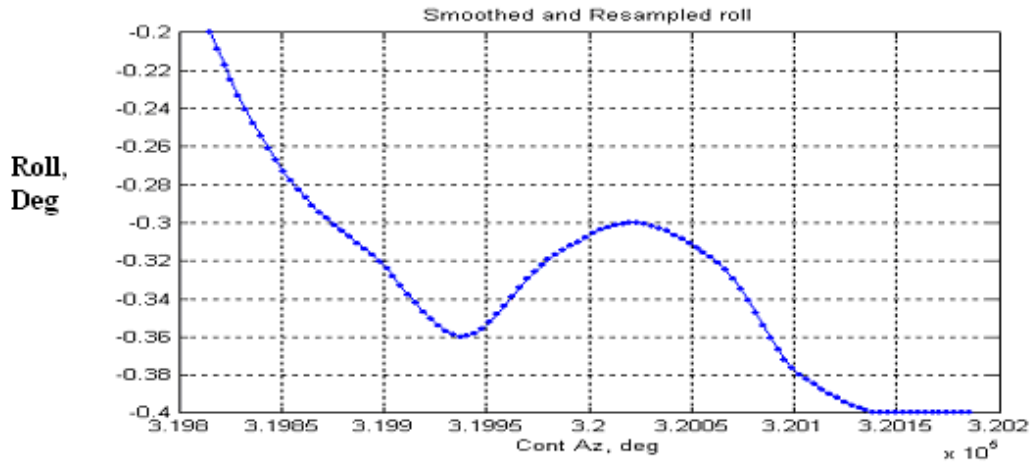

(b)

Fig. 4.12. (a) Example recorded quantized aircraft roll at one sample/sec for scan 183 (b) Smoothed and resampled roll at radiometer Tb measurements.

4.5 Tb comparisons

C-STAR was flown on several occasions; and two were selected around the State of Florida for this Tb model validation. The first flight was conducted in the Atlantic Ocean and was selected for its "fair weather" conditions that occurred on August 18, 2001 (hereafter called Andros Island flight). The second was performed in the Gulf of Mexico two days later on August 20, 2001 over more challenging surface and atmospheric conditions near hurricane Chantal. The significant differences in surface and atmospheric conditions allowed us to validate our models under a variety of flight conditions.

For a given flight segment, the procedure used to model the observed brightness is as follows:

1) Align aircraft and radiometer data in time by adding a delay of 11 sec to the aircraft data.
2) Smooth and resample aircraft attitude data.
3) Estimate environmental parameters using satellite data.
4) Model Tb's for selected scans

4.6 Andros Island Flight Tb Comparisons

The following section presents the comparison between our model and the measured Tb's for the C_STAR flight over Andros Island and in the Gulf of Mexico. The Andros island flight is primarily over mild environmental conditions while that in the Gulf of

Mexico has severe environmental conditions (moderate to heavy clouds and high winds). The Fig. 4.13 below illustrates the ground track and the selected scan groups for analysis during the Andros flight.

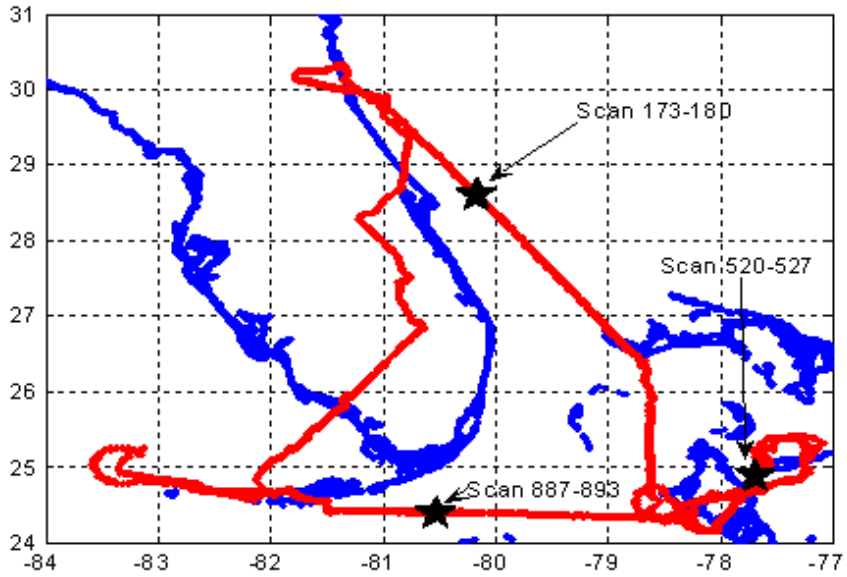

Fig. 4.13 Aircraft ground track during Andros Island flight with selected scan groups denoted by "stars".

As discussed in chapter 3, the Tb models for the vertical and horizontal polarizations, are;

$$Tbv = Tbv_{Atmos}(Az) + Tbv_{atmos}(Az) * \Gamma_v(\theta_i) * \tau + Tbv_{surface} * \tau + \frac{dTbv}{d\theta} * \Delta\theta_i \quad (4.1)$$

$$Tbh = Tbh_{Atmos}(Az) + Tbh_{atmos}(Az) * \Gamma_h(\theta_i) * \tau + Tbh_{surface} * \tau + \frac{dTbh}{d\theta} * \Delta\theta_i \quad (4.2)$$

and the unknown Tb_{atmos} was estimated using the procedure explained in chapter 3 and the following equations;

$$Tbv_{Atmos}(Az) = \frac{Tbv_{norm}(Az) - SST * (1 - \Gamma_v)}{1 + \tau * \Gamma_v} \quad (4.3)$$

$$Tbh_{Atmos}(Az) = \frac{Tbh_{norm}(Az) - SST * (1 - \Gamma_h)}{1 + \tau * \Gamma_h} \quad (4.4)$$

The $Tbh_{surface}$ is assumed to be isotropic and is estimated from satellite measurements of the surface wind speed as is the surface power reflection coefficient Γ. The term $Tb_{Atmos}(Az)$ term represents the brightness temperature emitted by the atmosphere, which is assumed to vary with azimuth position. Since atmospheric emission is non-polarized, both the vertical and horizontal polarizations should be the same. The Fig. 4.14 below illustrates an example of the calculated atmospheric brightness for the forward scene for scans 173-180.

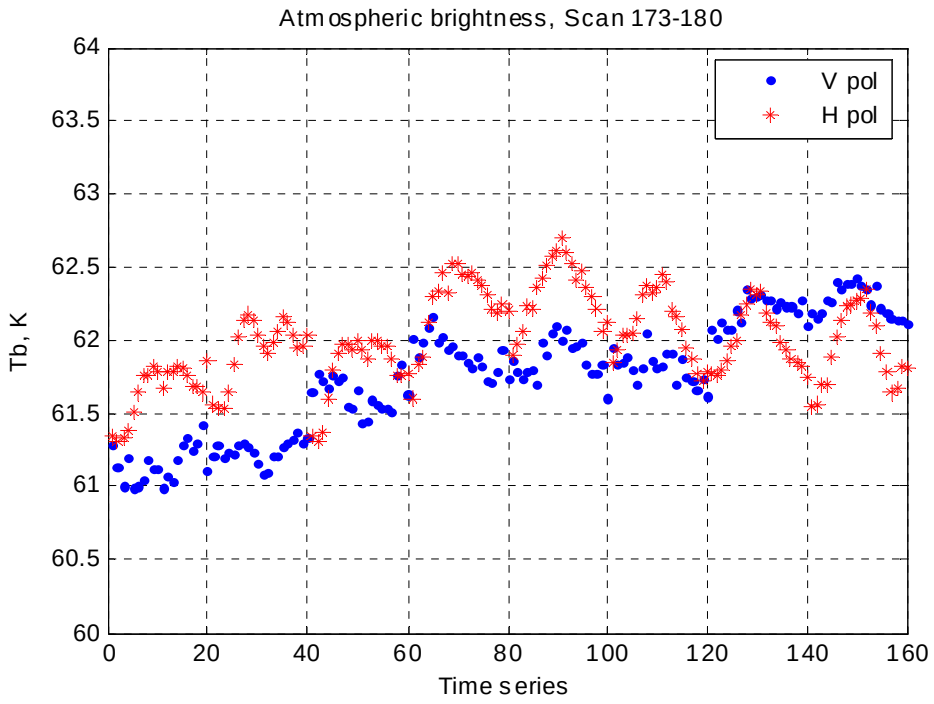

Figure 4.14 Atmospheric Tb for FWD scene, scan 173-180.

After using these environmental parameter estimates in eq. 4.1, the comparison between measured and modelled Tb's for both V- and H-polarization for the Andros Island flight is shown in Fig. 4.15 for the FWD scene and selected scans 173 -180. It is noted that the modelled and measured curves compare extremely well. Figures for the AFT scene are presented in Fig. 4.16.

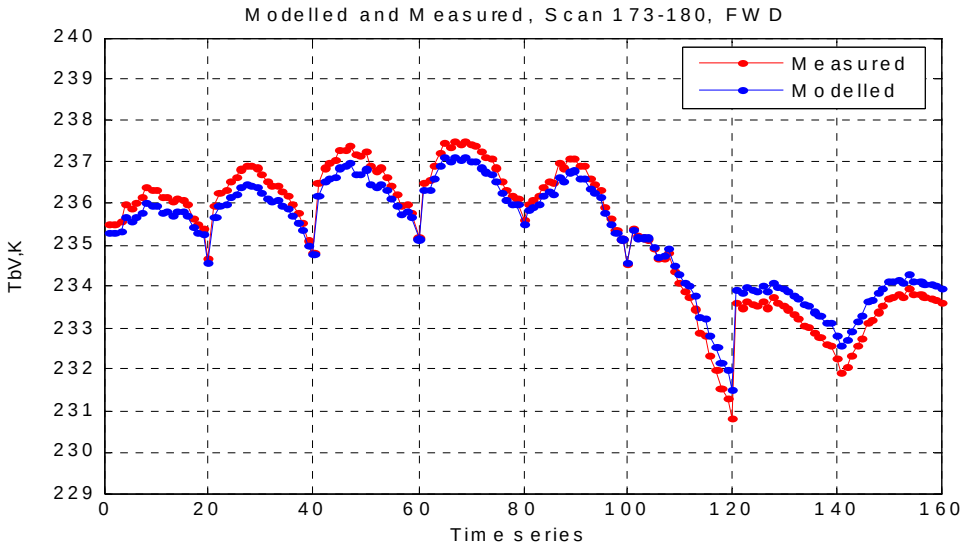

(a)

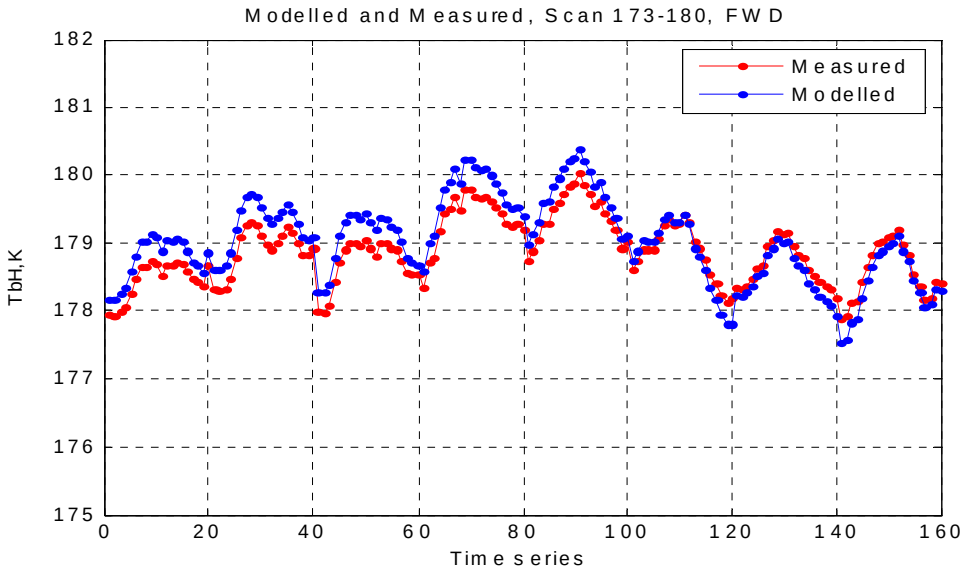

(b)

Figure 4.15 (a) Measured and modelled vertical Tb for Andros flight for FWD scene, scan 173-180. (b) Corresponding horizontal Tb.

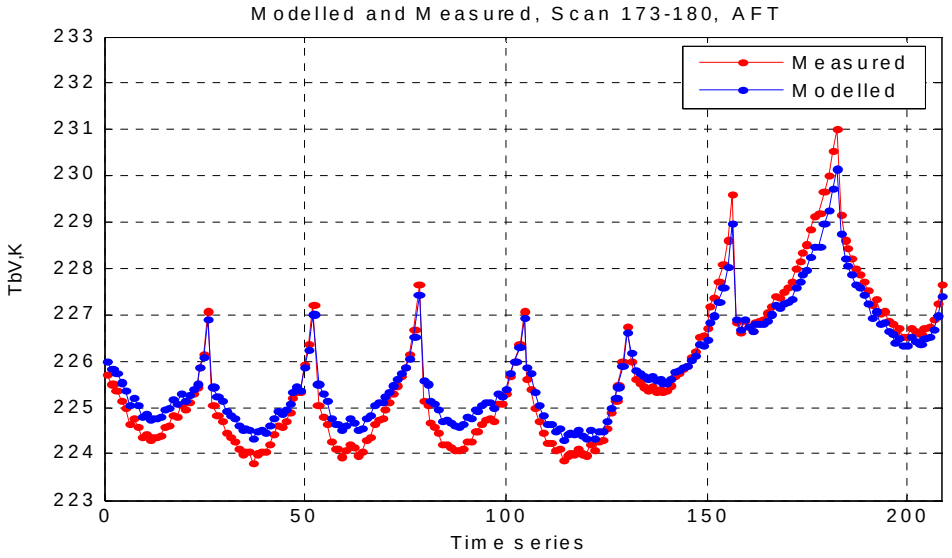

(a)

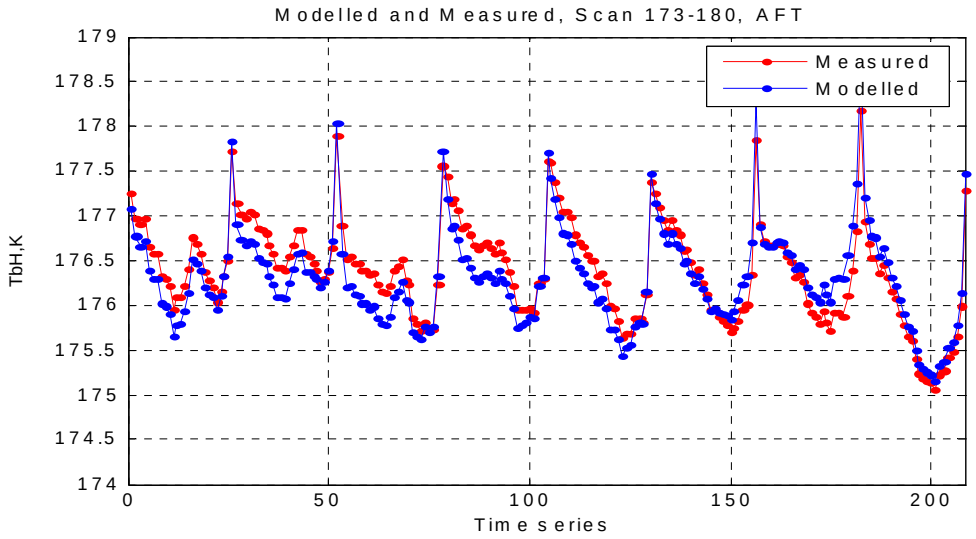

(b)

Figure 4.16(a) Measured and modelled vertical Tb for Andros flight for AFT scene, scan 173-180. (b) Corresponding horizontal Tb.

FWD and AFT comparisons for the second scan group (520 – 526) are shown in Fig. 4.17 and 4.19. In the AFT observations of this scan group, further editing was required due to the fact that part of the scans were observing land instead of water. Figure 4.18b, which is a plot of the antenna boresight location, shows that most of the scans have portions observing land. This correlates with figure 4.18a where we observe expected increases in land brightness at those corresponding azimuths. Since our models were developed for ocean brightness temperature, the land contaminated data points were removed.

Finally, the FWD and AFT comparisons for the third scan group (887 – 893) are shown in figure 4.20 through 4.21 respectively.

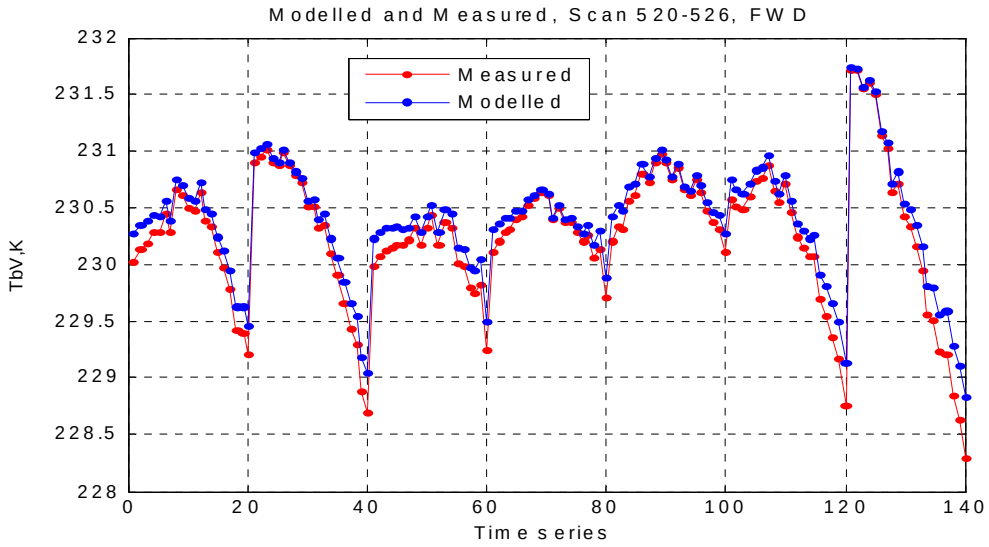

(a)

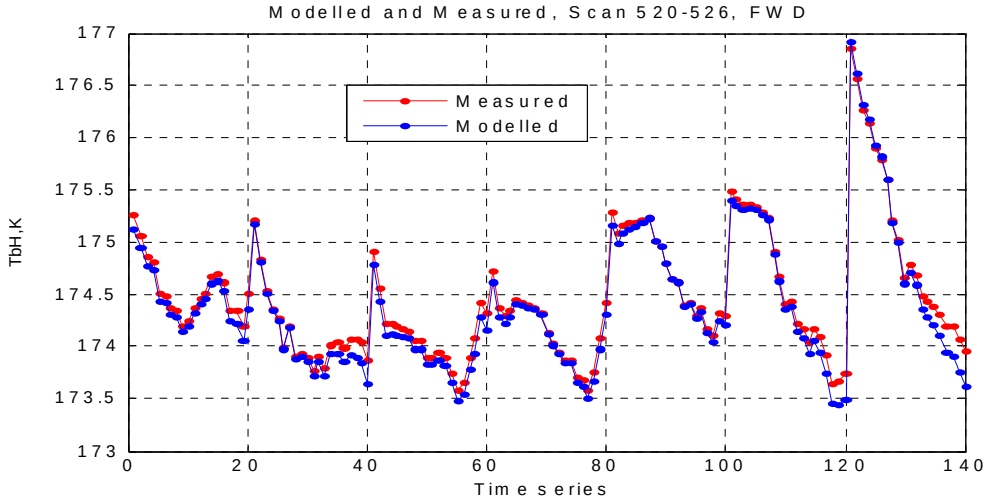

(b)

Figure 4.17 (a) Measured and modelled vertical Tb for Andros flight for FWD scene, scan 520-526. (b) Corresponding horizontal Tb.

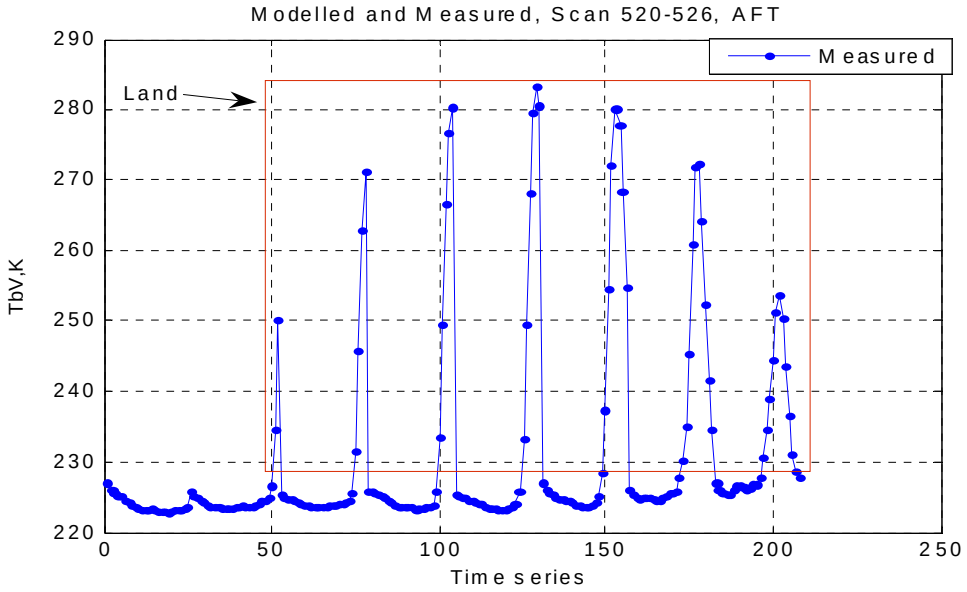

(a)

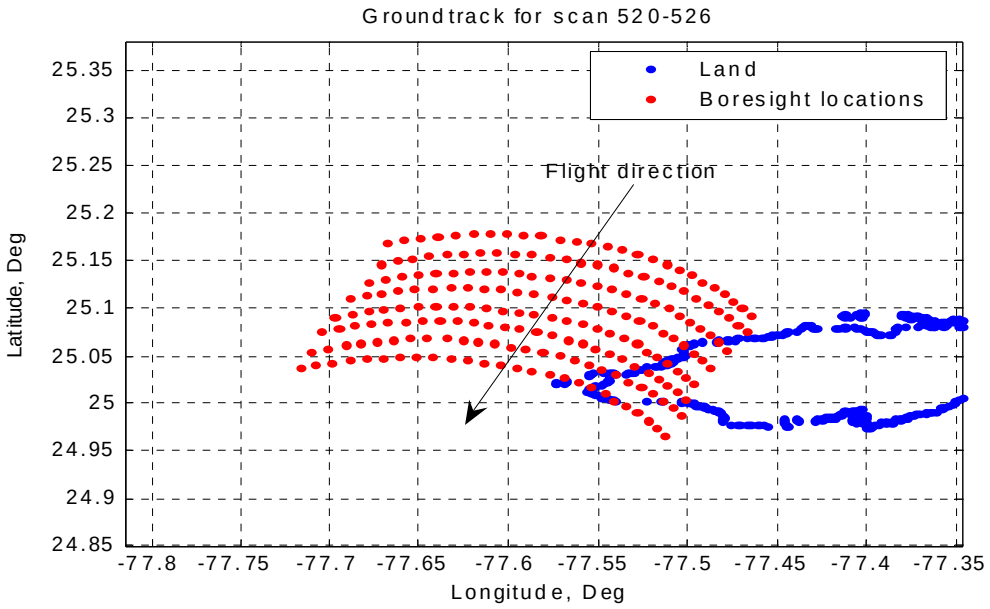

(b)

Figure 4.18 (a)) Measured vertical Tb for Andros flight for AFT scene, scan 520-526.

(b) Corresponding antenna boresight locations

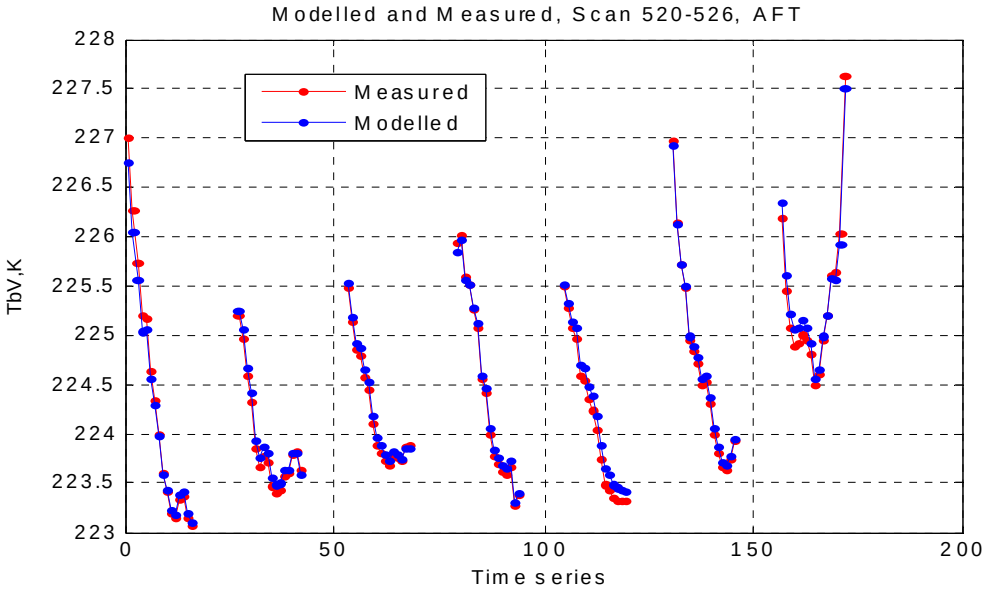

(a)

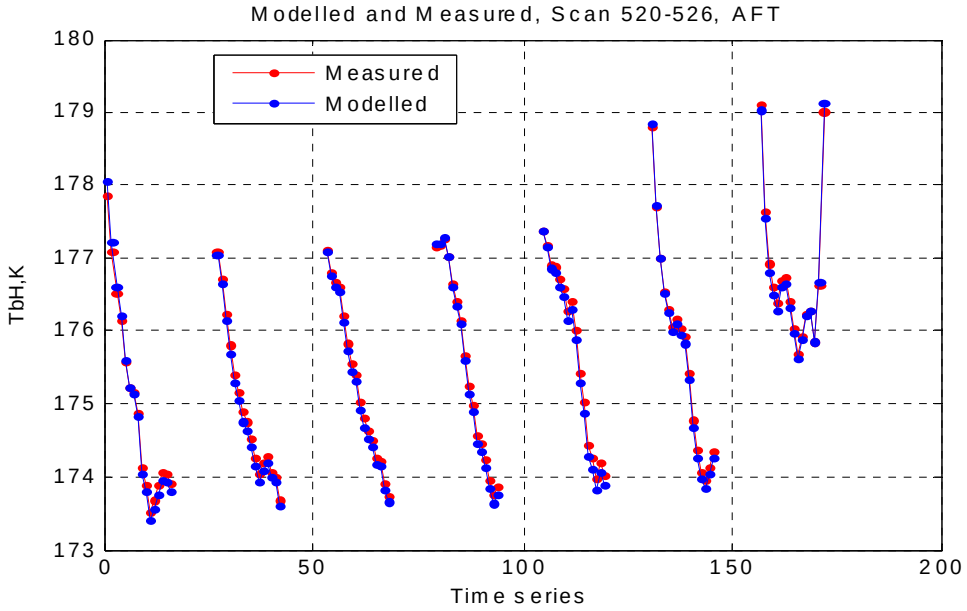

(b)

Figure 4.19 (a) Measured and modelled vertical Tb for Andros flight for AFT scene, scan 520-526 and land removed. (b) Corresponding horizontal Tb.

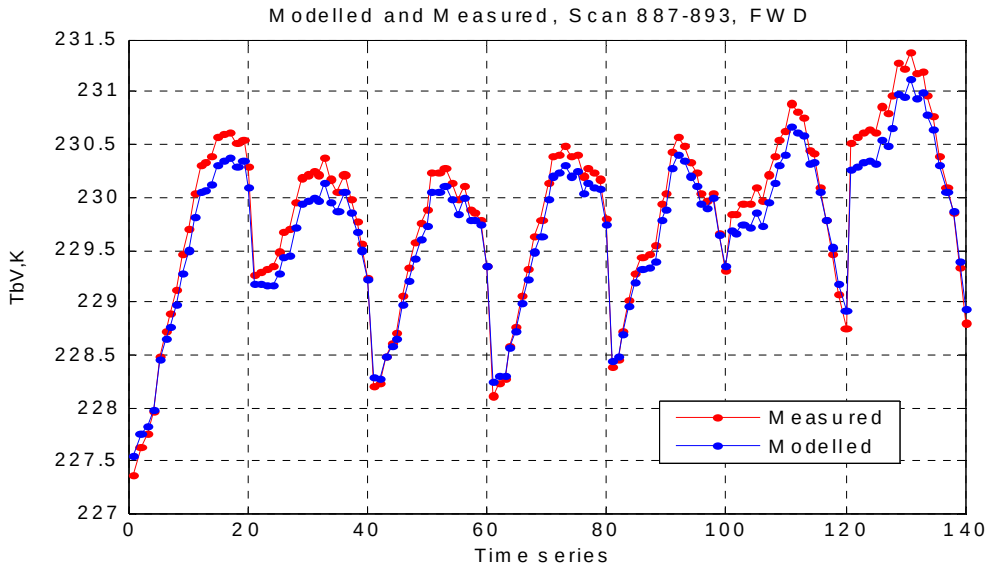

(a)

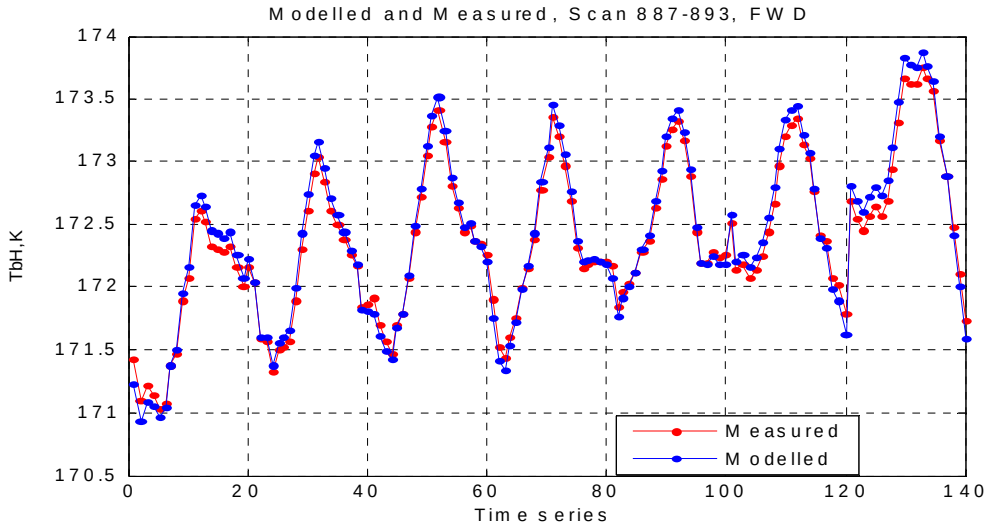

(b)

Figure 4.20 (a) Measured and modelled vertical Tb for Andros flight for FWD scene, scan 887-893. (b) Corresponding horizontal Tb.

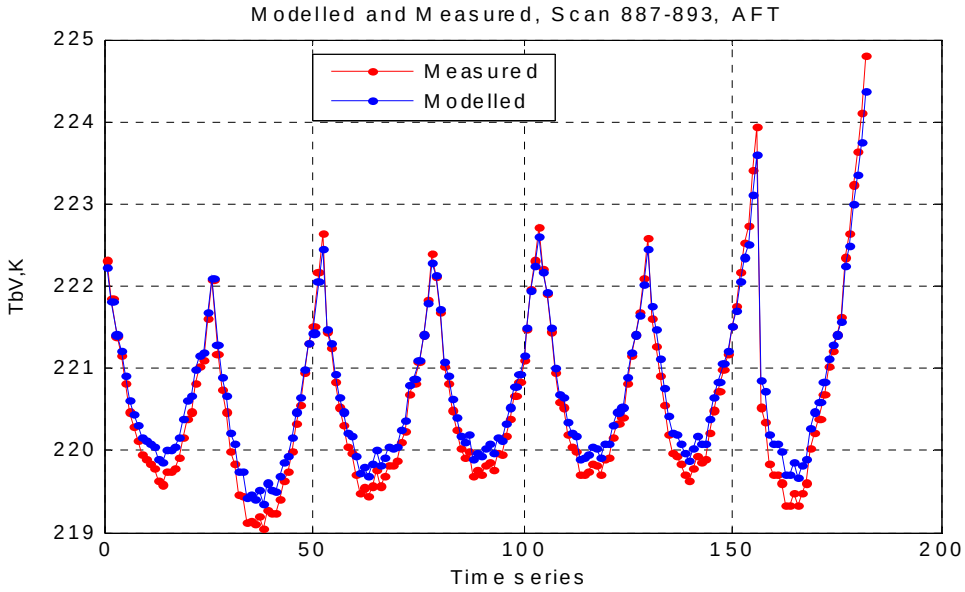

(a)

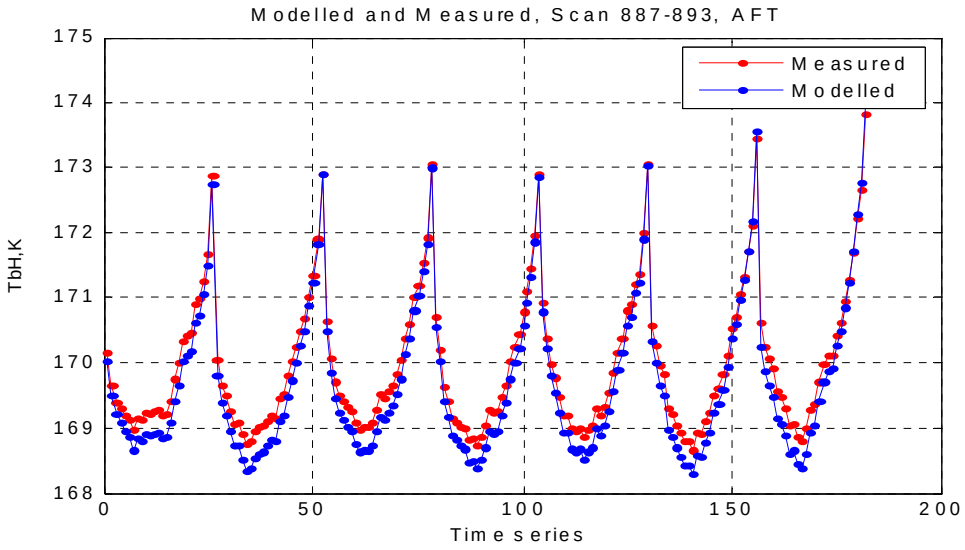

(b)

Figure 4.21 (a) Measured and modelled vertical Tb for Andros flight for AFT scene, scan 887-893. (b) Corresponding horizontal Tb.

A summary of the RMS differences between the modelled and measured brightness for the above scan groups are listed in the following Table 4.1.

Table 4.1 RMS difference (deg) for horizontal and vertical Tb for Andros flight.

	Scan 173-180		Scan 520-527		Scan 887-893	
	Forward	Aft	Forward	Aft	Forward	Aft
RMS_V	.35	.36	.154	.18	.161	.194
RMS_H	.27	.24	.096	.488	.086	.28

4.7 Hurricane flight Tbv & Tbh Comparisons

Because the second C-STAR flight occurred in the Gulf of Mexico near a hurricane, there were much stronger environmental conditions. Typically, in the vicinity of a hurricane, there is extensive rain and cloud cover, which would obscure the surface observations. Scan were carefully selected, using the cloud editing QC procedure, to avoid areas where rain and heavy cloud cover existed. The following figure illustrates the ground track and the selected scan groups. A plot of the aircraft ground track with selected scan groups is shown in Fig. 4.22; and an example of the calculated atmospheric brightness used for modeling is shown in Fig. 4.23.

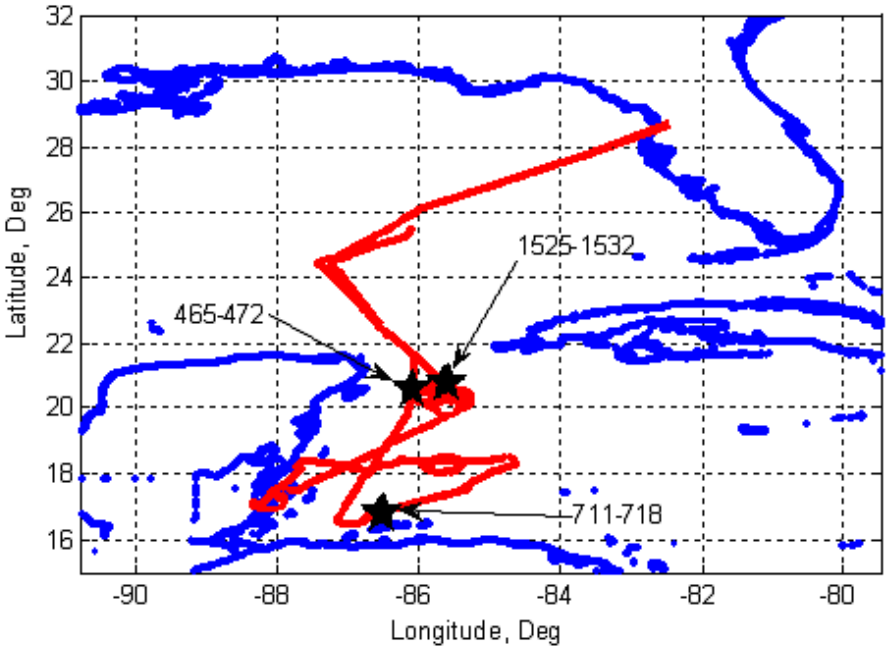

Figure 4.22 Ground track over Gulf of Mexico for hurricane flight.

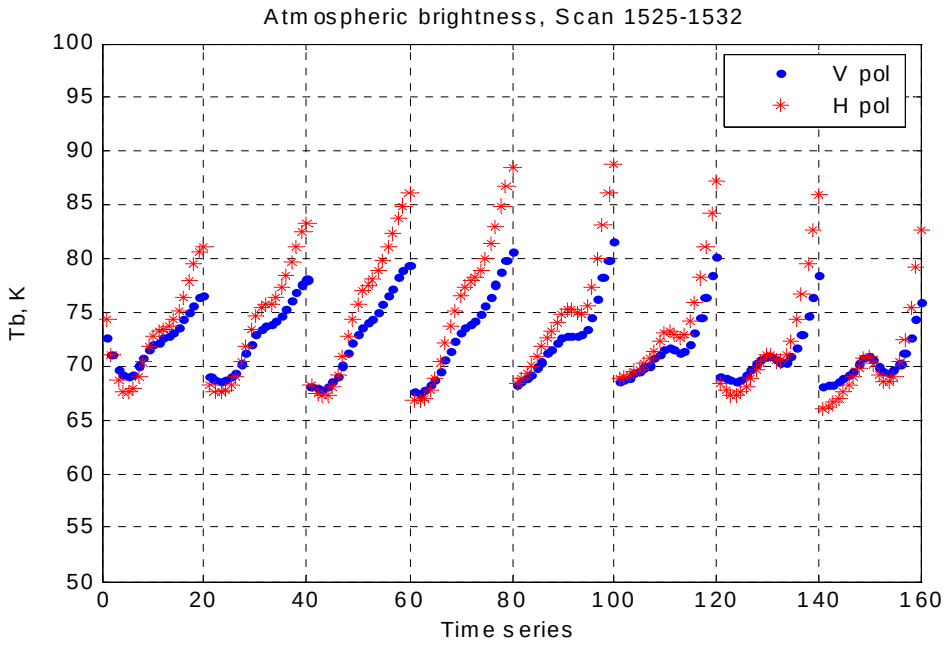

Figure 4.23 Atmospheric brightness for forward scene, scans 1525 - 1535.

Figures 4.24 and 4.25 show the comparison between the measured and modelled vertical brightness for the last scan group (1525 – 1532) for both the FWD and AFT scenes respectively. Next, the FWD and AFT comparisons for the first scan group (465 – 472) are shown in Fig. 4.26 and 4.27; and finally, the FWD and AFT comparisons for the middle scan group (711 – 718) are shown in figure 4.28 and 4.29. All of these results are similar to those of the Andros Island flight in that both modelled and measured sets of Tb curves agree very well in magnitude and dynamic range.

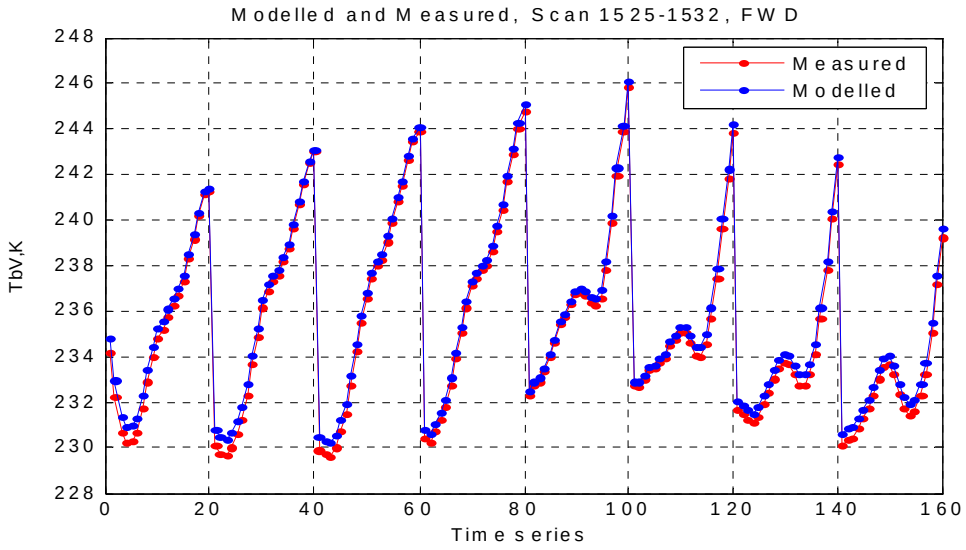

(a)

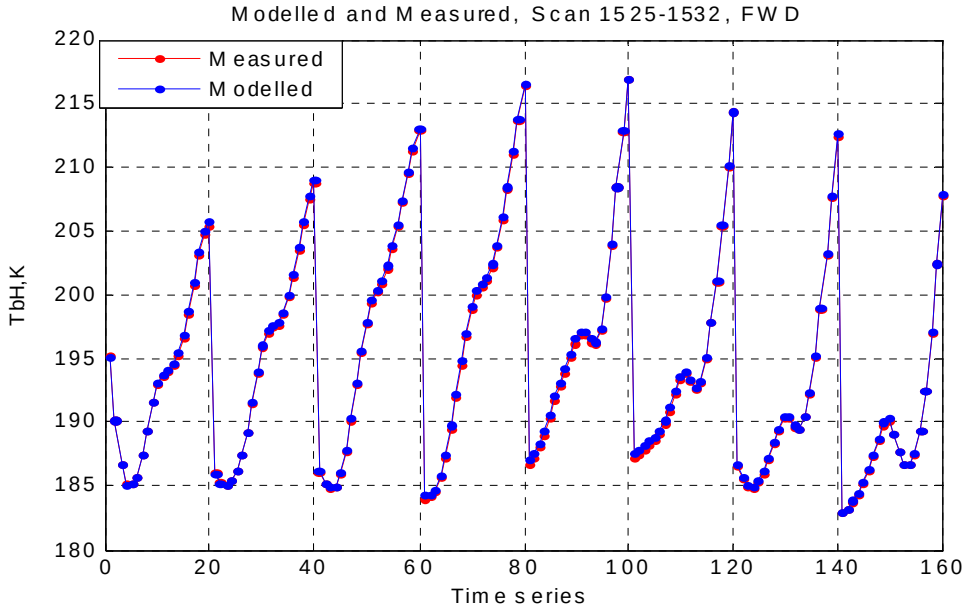

(b)

Figure 4.24 (a) Measured and modelled vertical Tb for Gulf of Mexico flight for FWD scene, scan 1525-1532. (b) Corresponding horizontal Tb.

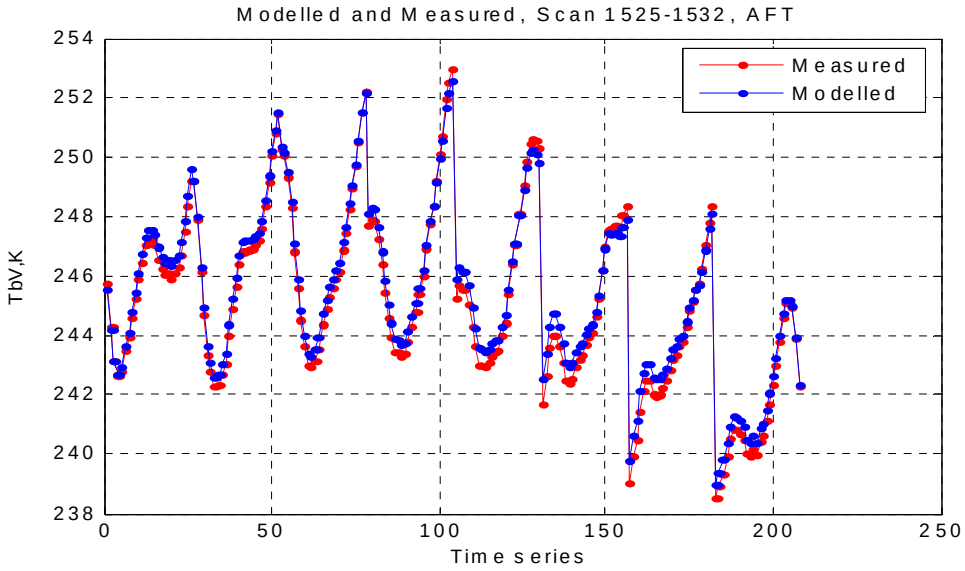

(a)

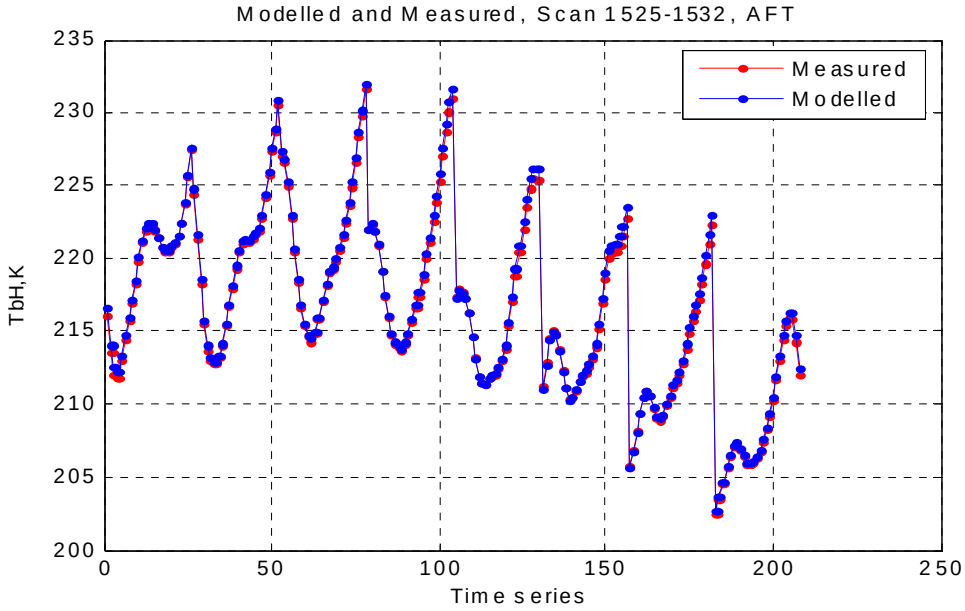

(b)

Figure 4.25 (a) Measured and modelled vertical Tb for Gulf of Mexico flight for AFT scene, scan 1525-1532. (b) Corresponding horizontal Tb.

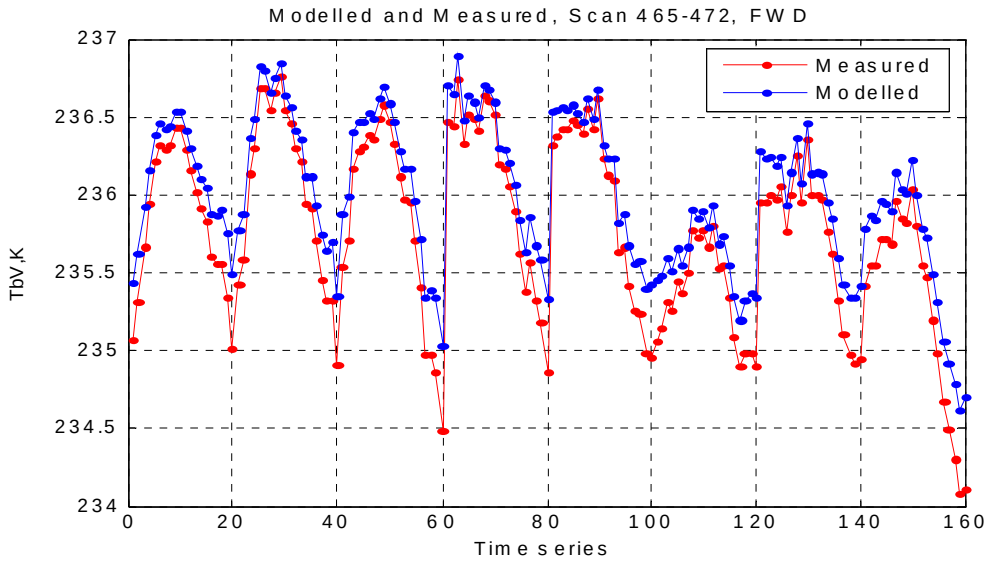

(a)

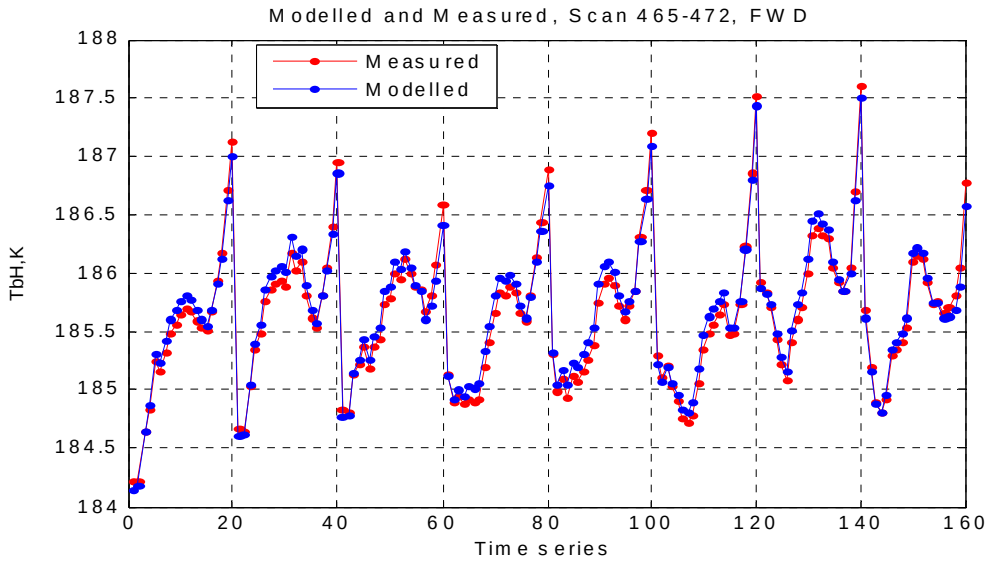

(b)

Figure 4.26 (a) Measured and modelled vertical Tb for Gulf of Mexico flight for FWD scene, scan 465-472. (b) Corresponding horizontal Tb.

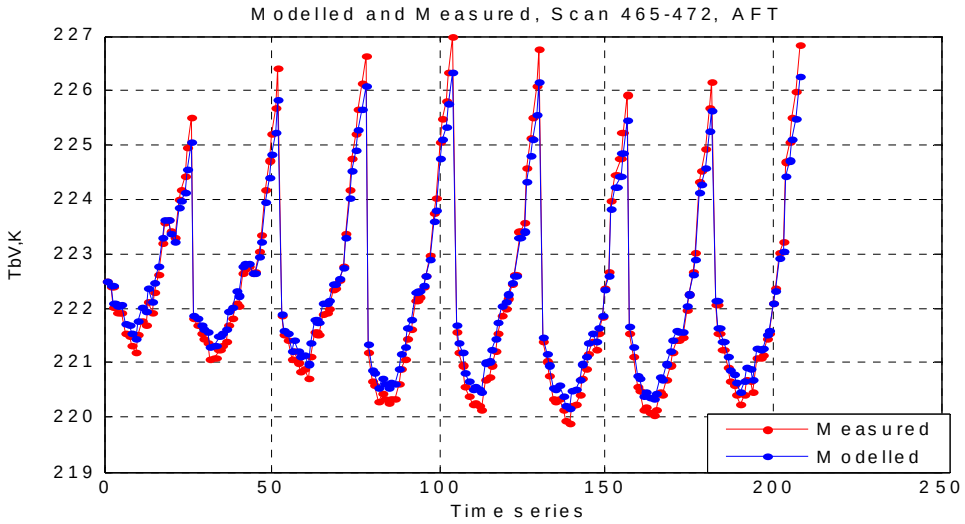

(a)

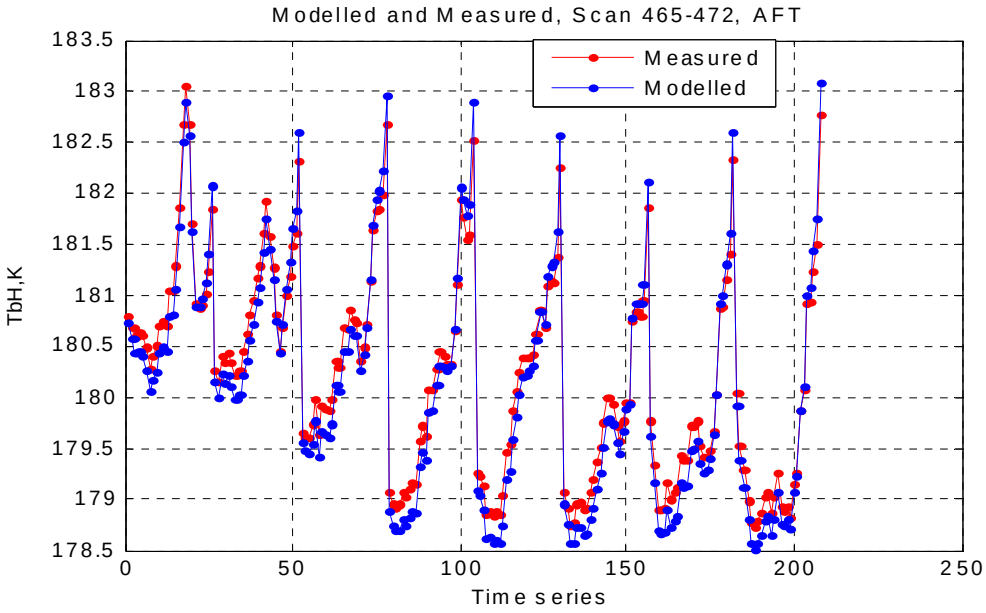

(b)

Figure 4.27 (a) Measured and modelled vertical Tb for Gulf of Mexico flight for AFT scene, scan 465-472. (b) Corresponding horizontal Tb.

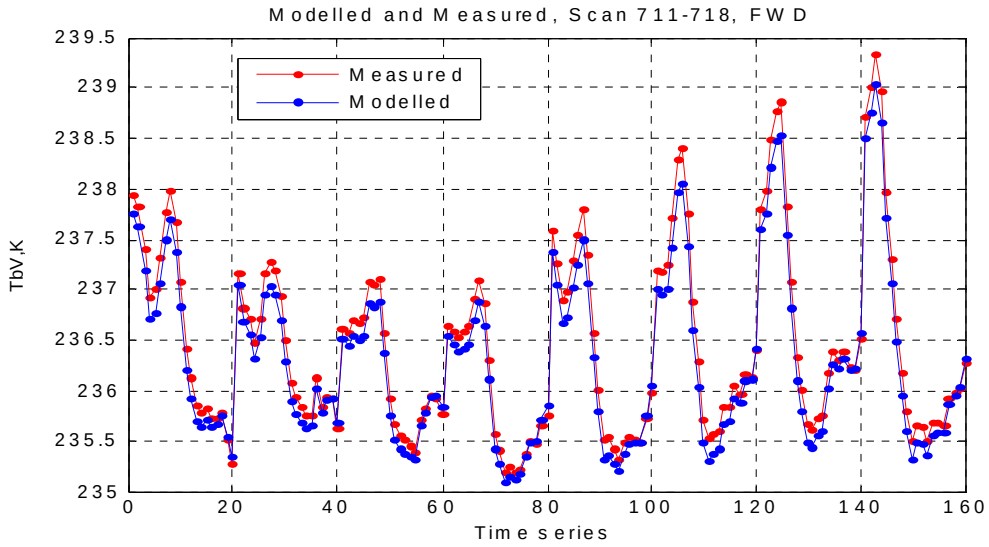

(a)

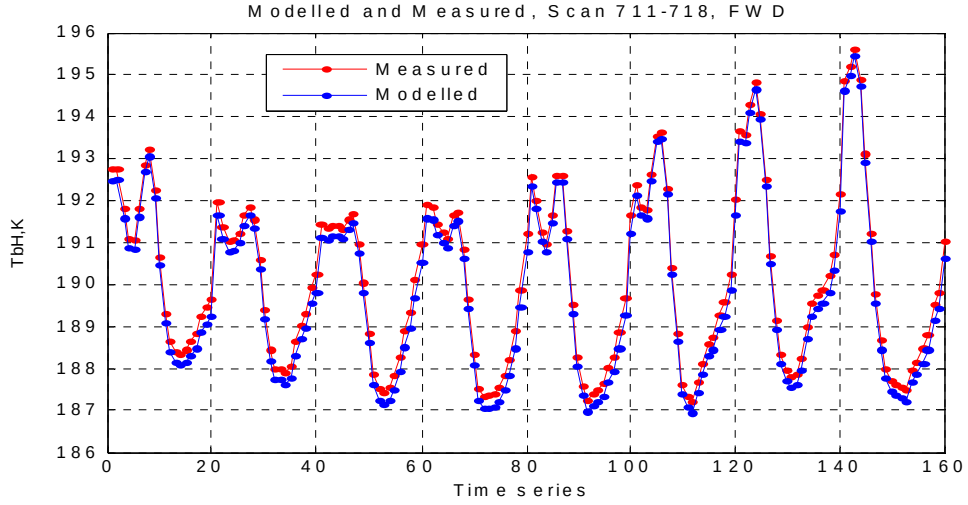

(b)

Figure 4.28 (a) Measured and modelled vertical Tb for Gulf of Mexico flight for FWD scene, scan 711-718. (b) Corresponding horizontal Tb.

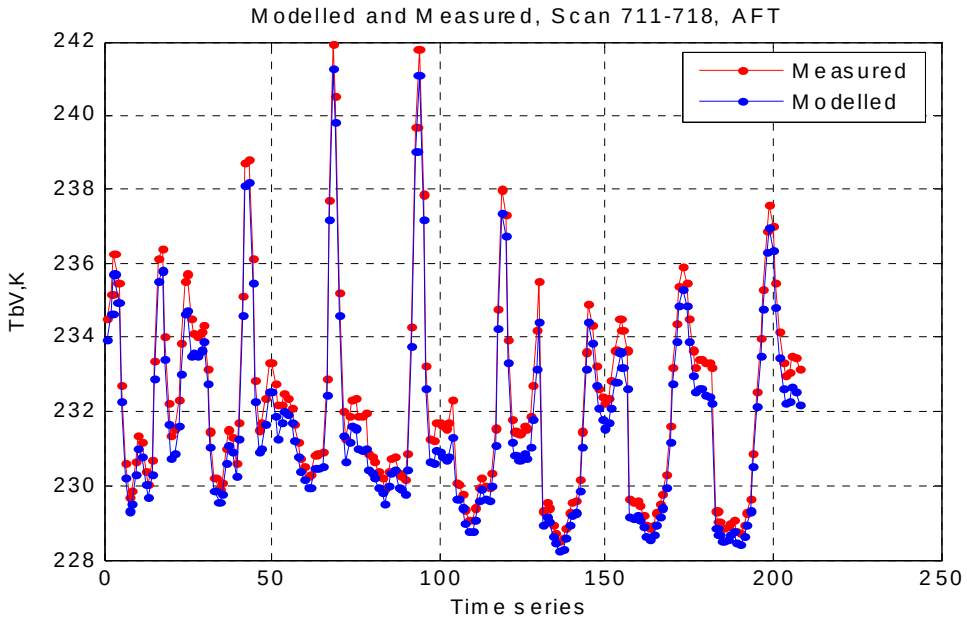

(a)

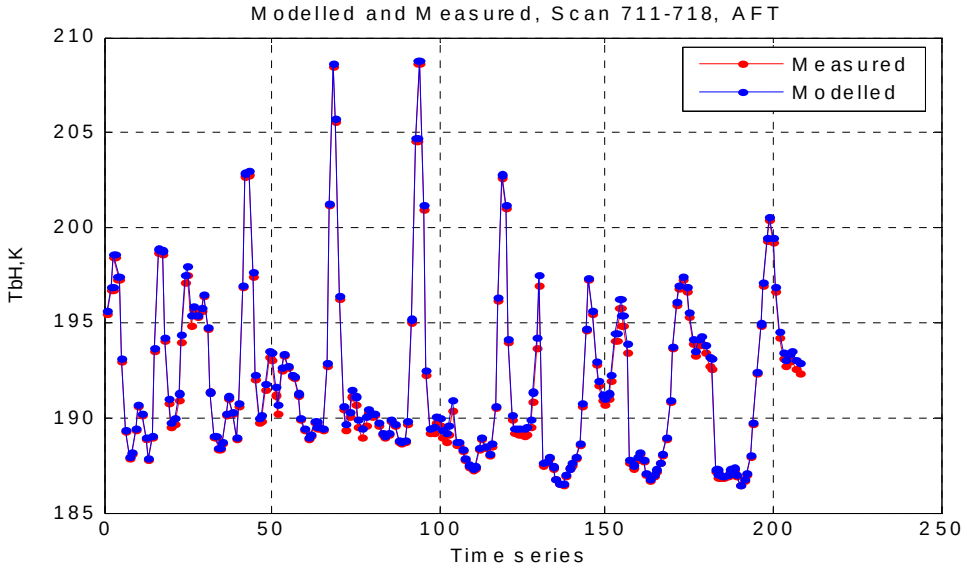

(b)

Figure 4.29 (a) Measured and modelled vertical Tb for Gulf of Mexico flight for AFT scene, scan 711-718. (b) Corresponding horizontal Tb.

These results for the RMS differences between the modelled and measured brightness, for the above scan groups during the Gulf of Mexico flights, are listed in the table below.

Table 4.2 RMS difference for horizontal and vertical Tb for Gulf of Mexico flight.

	Scan 1525-1532		Scan 465-472		Scan 711-718	
	Forward	Aft	Forward	Aft	Forward	Aft
RMS_V	.36	.35	.253	.24	.176	.581
RMS_H	.18	.28	.089	.205	.281	.23

4.8 Andros island TbP & TbQ comparison

Since the P- and Q-polarizations are obtained by equally mixing the horizontal and vertical polarizations, we would expect these Tb's to be between the typical vertical and horizontal brightness. Prior to showing comparisons for the P- and Q-polarizations, we repeat the models derived in chapter 3 eq. 3.11 and 3.12.

$$Tbp = TbH(\theta_i) * \cos^2(\beta_{+45}) + TbV(\theta_i) * \sin^2(\beta_{+45}) \qquad (4.5)$$

$$Tbq = TbH(\theta_i) * \cos^2(\beta_{-45}) + TbV(\theta_i) * \sin^2(\beta_{-45}) \qquad (4.6)$$

The selected scan groupings for these comparisons were the same as discussed above for V- and H-polarizations. The comparison of our model and the measured brightness temperatures are presented in Figs. 4.30 - 4.35 for the various scan groups and for the FWD and AFT scenes.

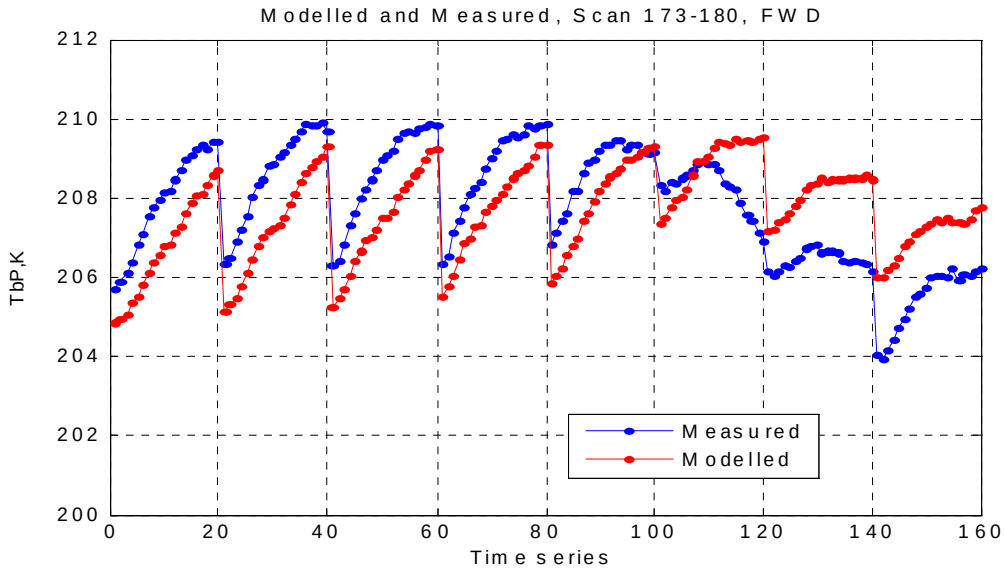

(a)

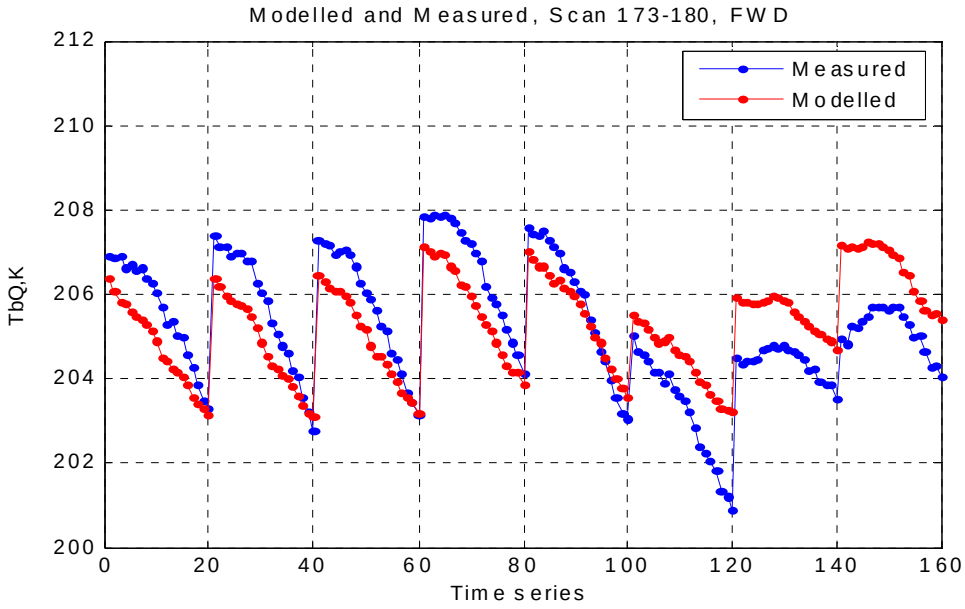

(b)

Figure 4.30 (a) Measured and modelled P Tb for Andros flight for FWD scene, scan 173-180. (b) Corresponding Q Tb.

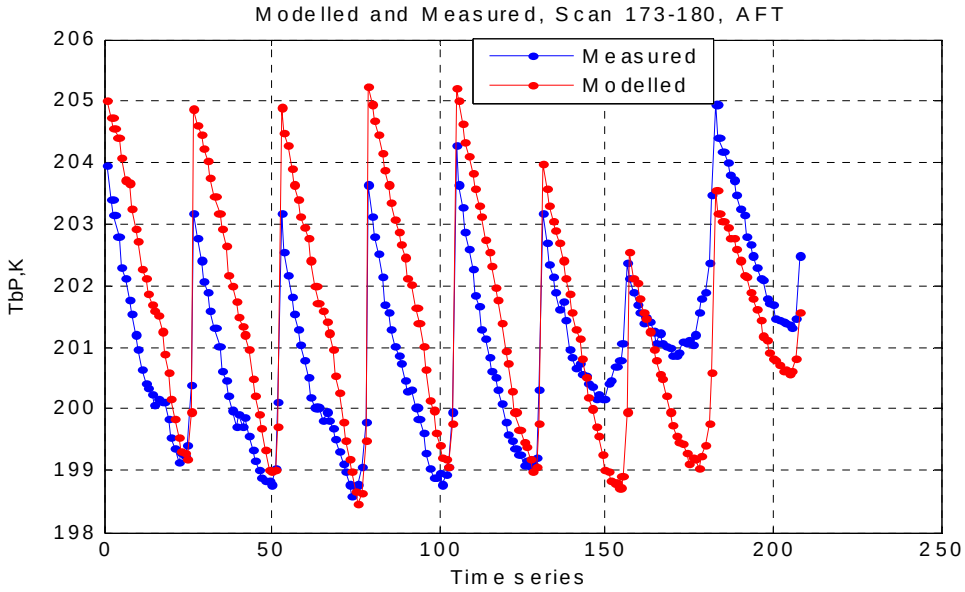

(a)

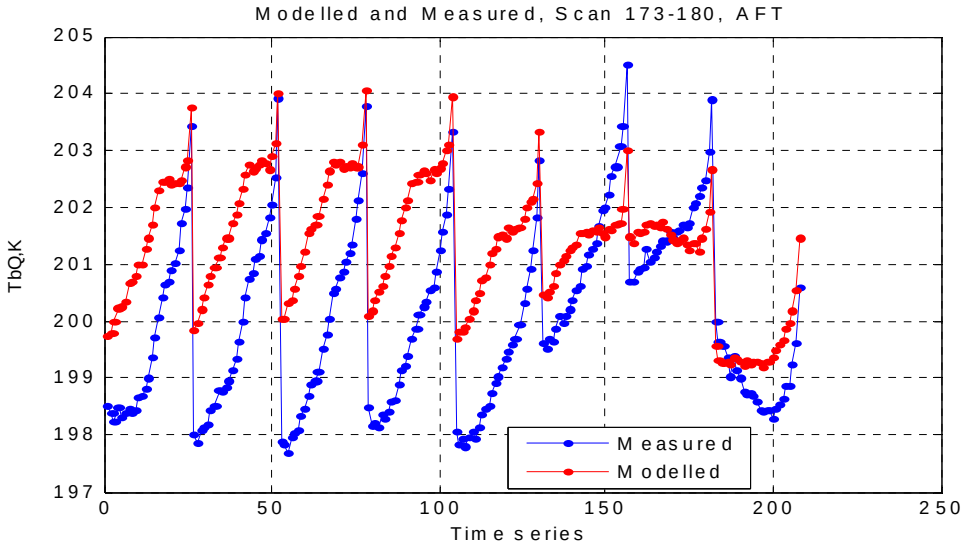

(b)

Figure 4.31 (a) Measured and modelled P Tb for Andros flight for AFT scene, scan 173-180. (b) Corresponding Q Tb.

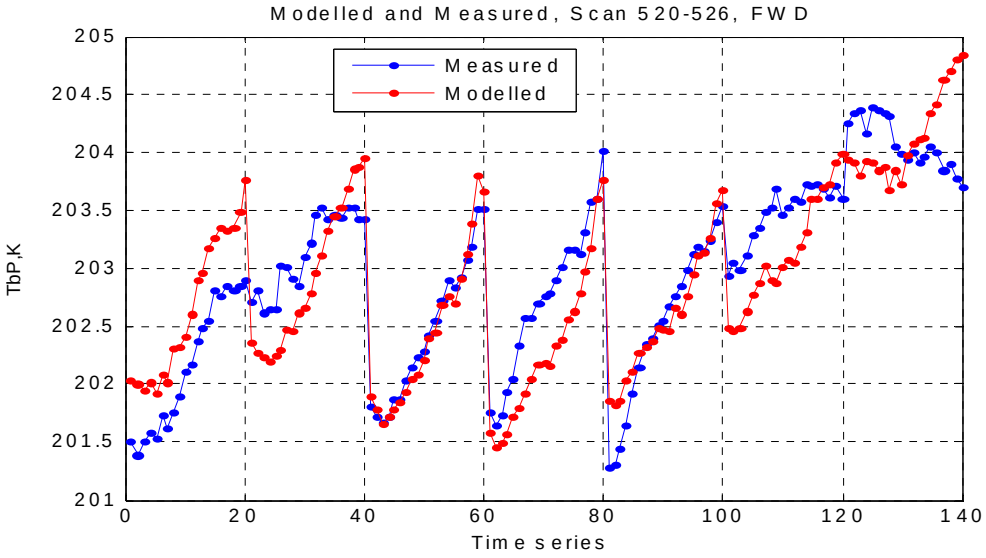

(a)

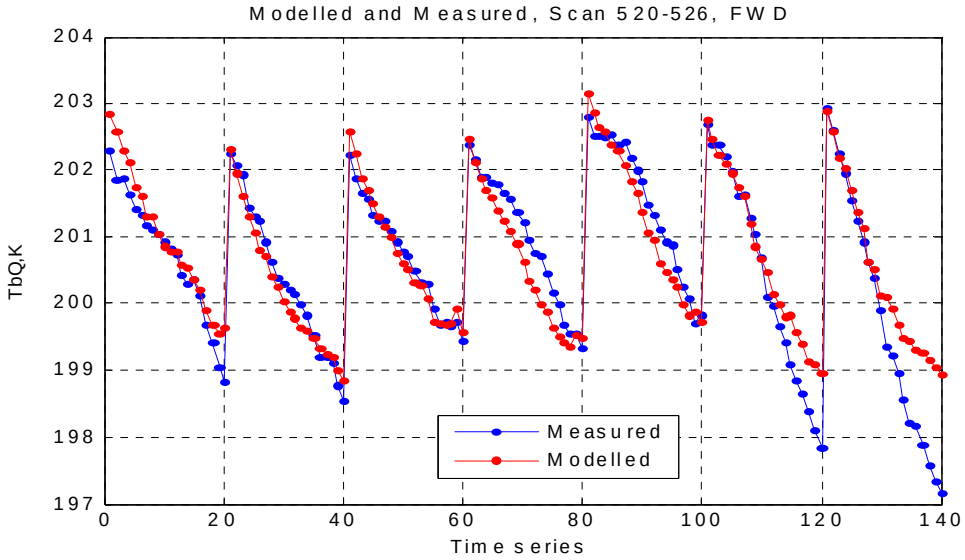

(b)

Figure 4.32 (a) Measured and modelled P Tb for Andros flight for FWD scene, scan 520-526. (b) Corresponding Q Tb.

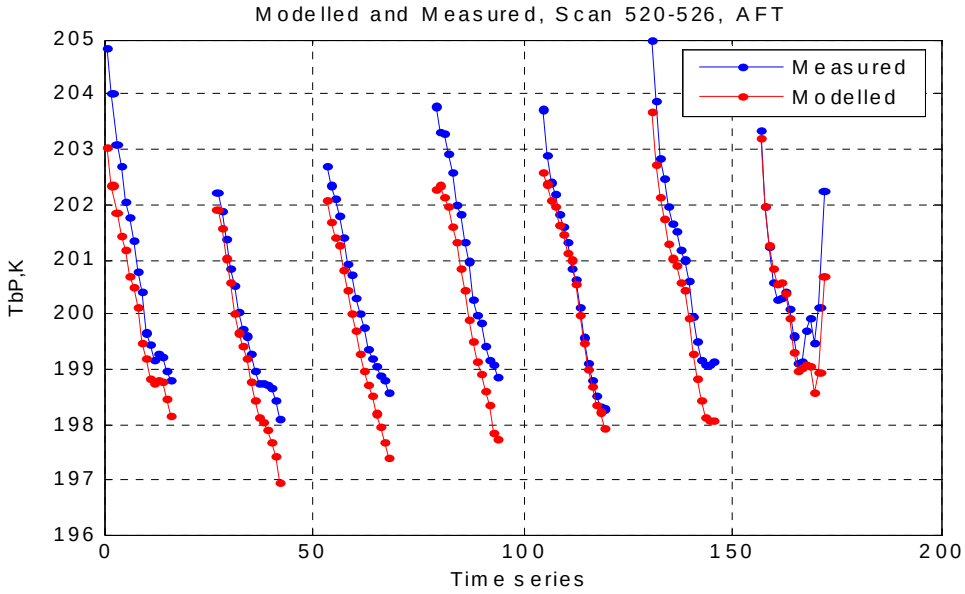

(a)

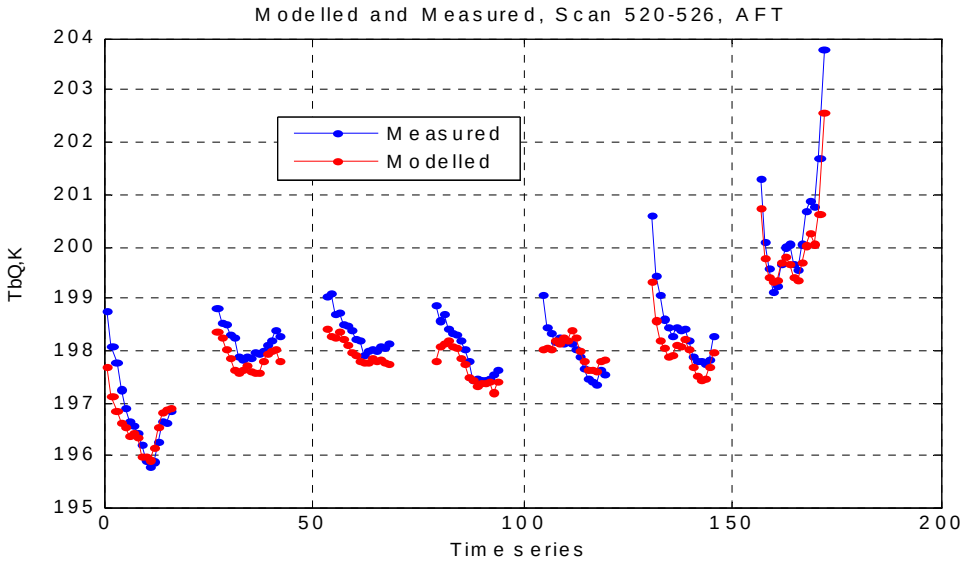

(b)

Figure 4.33 (a) Measured and modelled P Tb for Andros flight for AFT scene, scan 520-526. (b) Corresponding Q Tb.

FWD and AFT comparisons for scan group 887-893 are shown in figure 4.34 and 4.35 respectively.

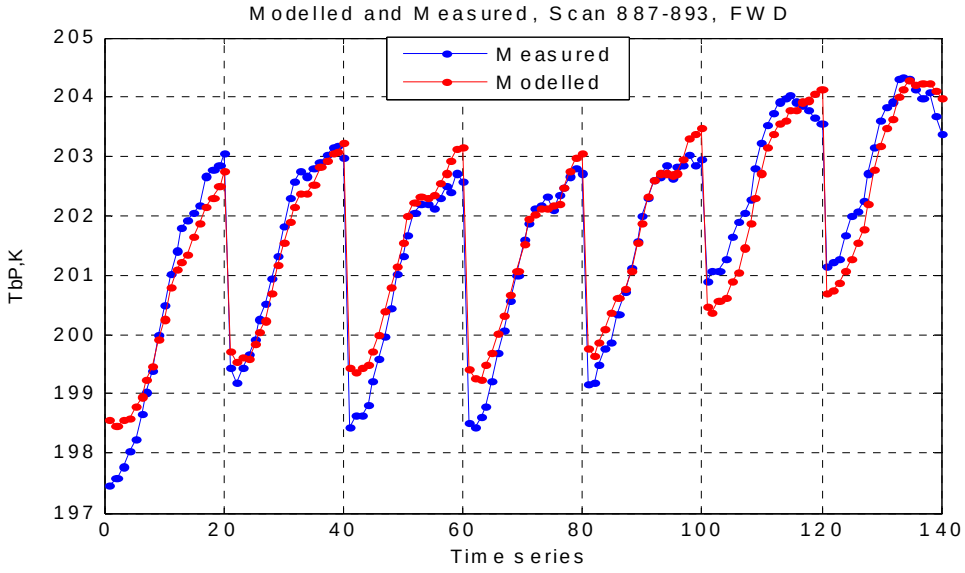

(a)

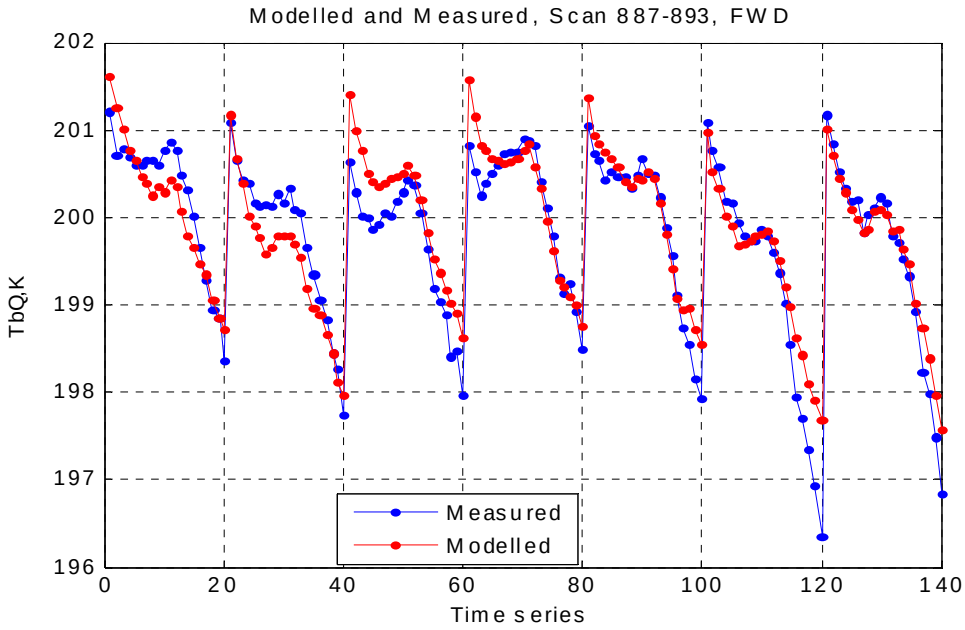

(b)

Figure 4.34 (a) Measured and modelled P Tbs for Andros flight for FWD scene, scan 887-893. (b) Corresponding Q Tb.

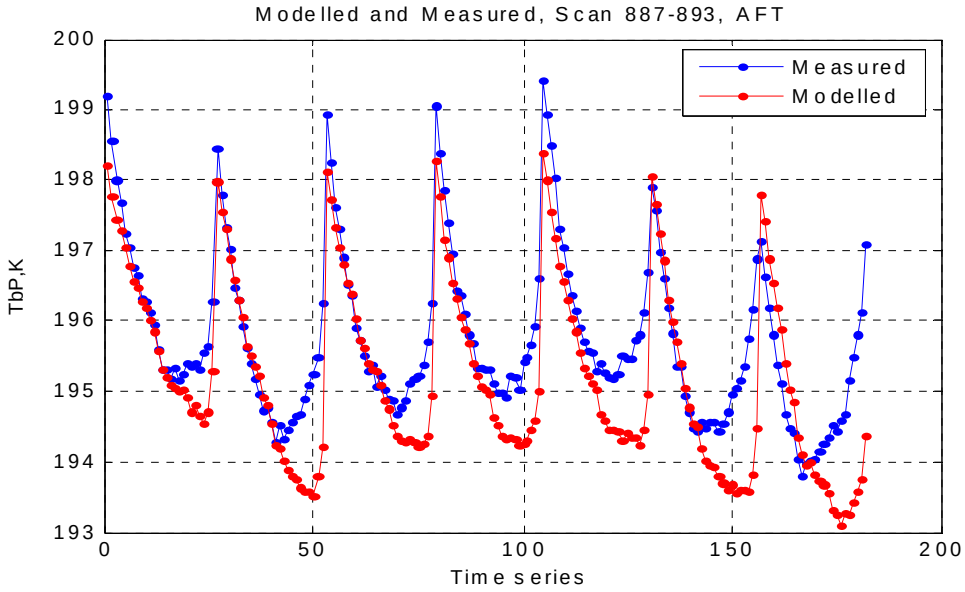

(a)

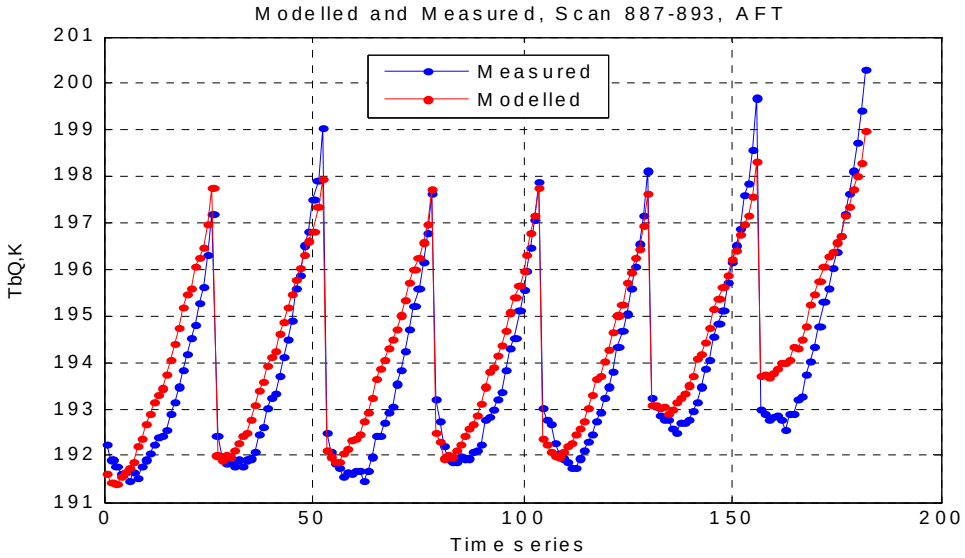

(b)

Figure 4.35 (a) Measured and modelled P Tb for Andros flight for AFT scene, scan 887-893. (b) Corresponding Q Tb.

A summary of the RMS differences between the modelled and measured brightness for the above scan groups is listed in Table 4.3.

Table 4.3 RMS difference (deg) for P- and Q-brightness for Andros flight.

	Scan 173-180		Scan 520-527		Scan 887-893	
	Forward	Aft	Forward	Aft	Forward	Aft
RMS_P	1.27	1.3	.367	.88	.401	.83
RMS_Q	.988	1.56	.397	.956	.348	.74

4.9 Hurrincane flight TbP & TbQ comparison

As mentioned previously, because of strong surface winds and heavy clouds and rain environmental conditions in the hurricane flight, we observed increases in the V- and H-pol brightness temperature. In this section, the comparison of our model and the measured brightness temperatures are presented in Figs. 4.36 - 4.41 for the various scan groups and for the FWD and AFT scenes. As was the case for V- and H-pols, the results reveals a very close match between our model and the measured polarizations.

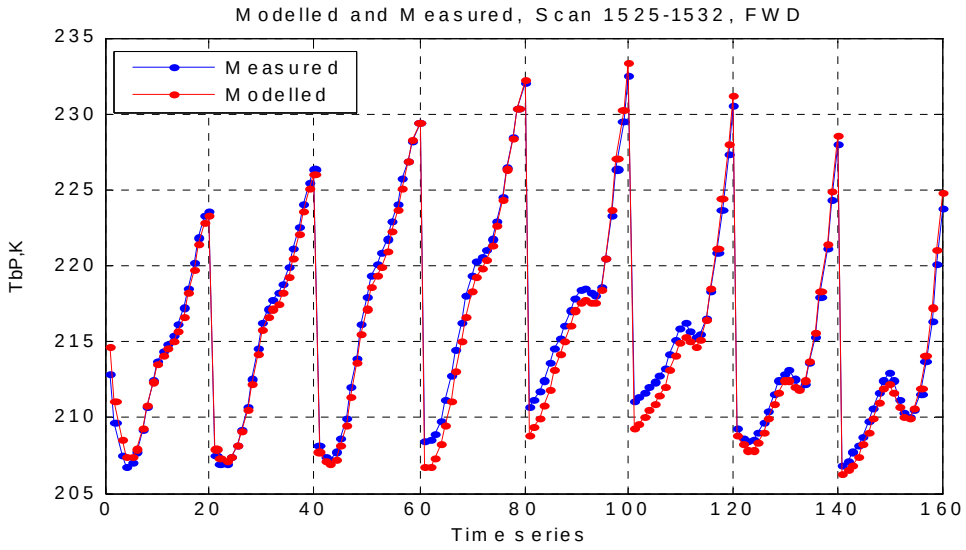

(a)

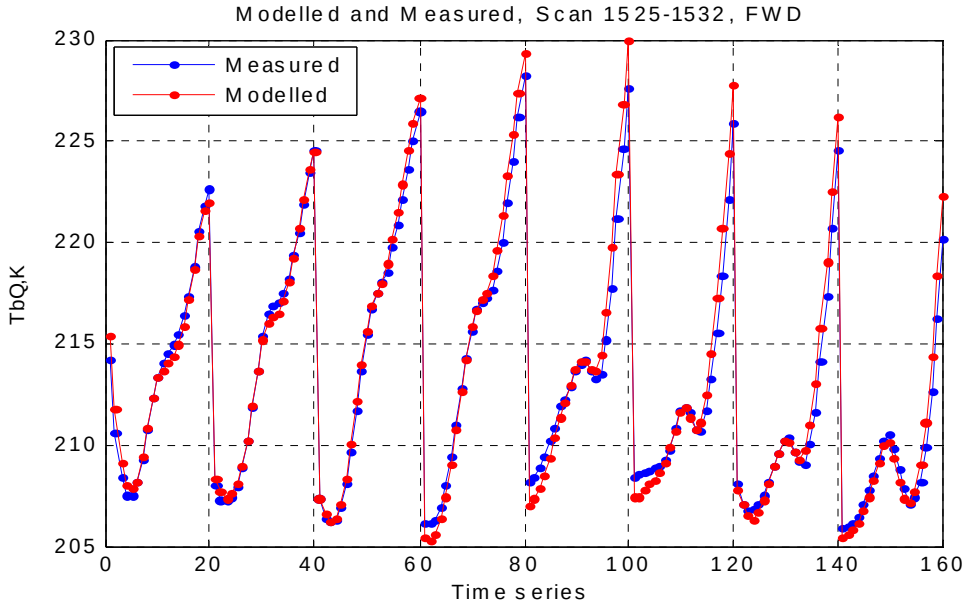

(b)

Figure 4.36 (a) Measured and modelled P Tb for Gulf of Mexico flight for FWD scene, scan 1525-1532. (b) Corresponding Q Tb.

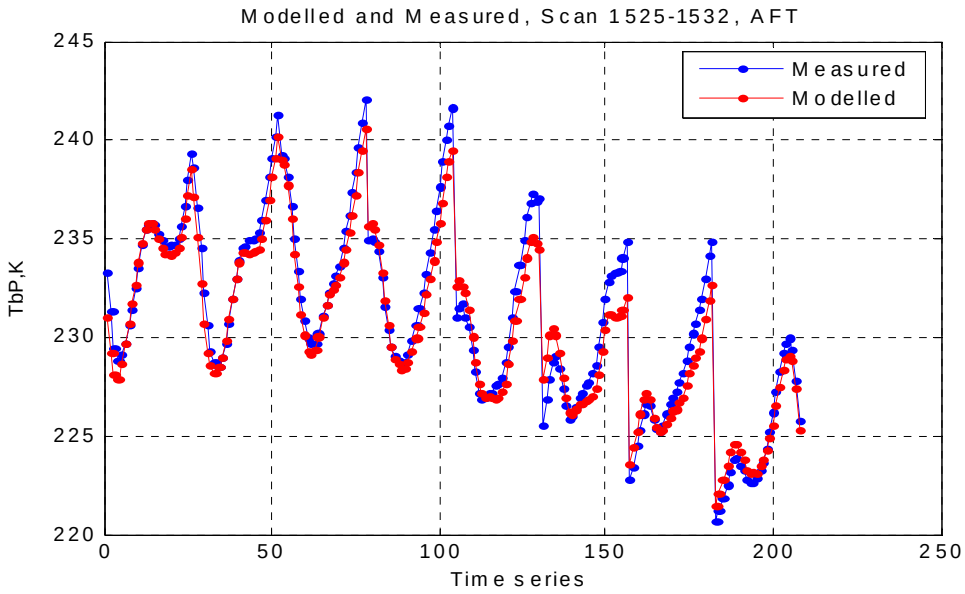

(a)

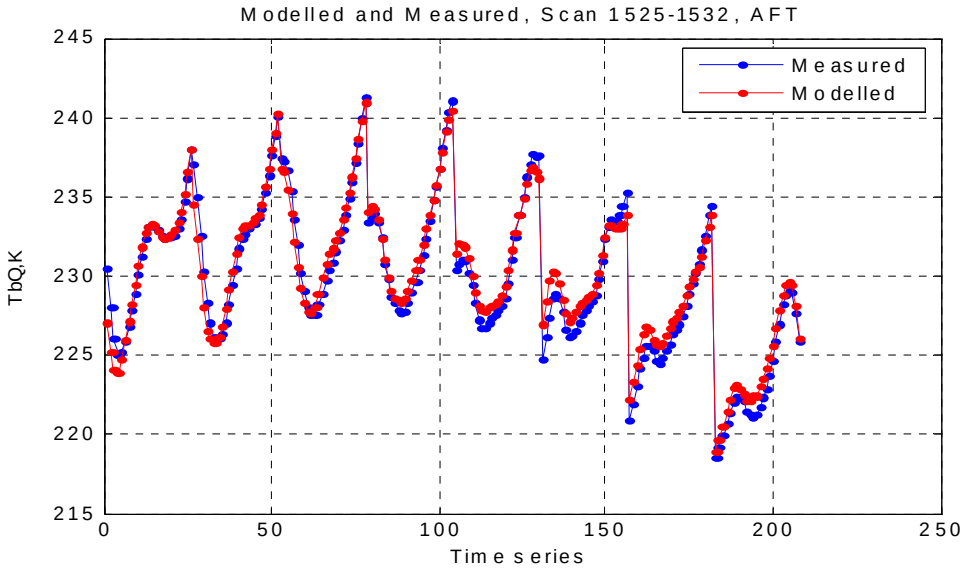

(b)

Figure 4.37 (a) Measured and modelled P brightness for Gulf of Mexico flight for AFT scene, scan 1525-1532. (b) Corresponding Q Tb.

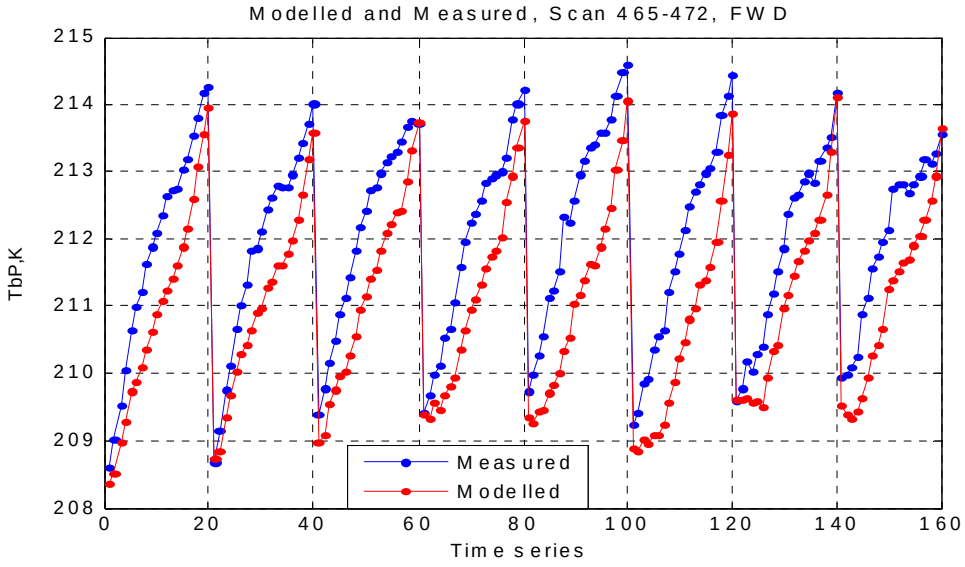

(a)

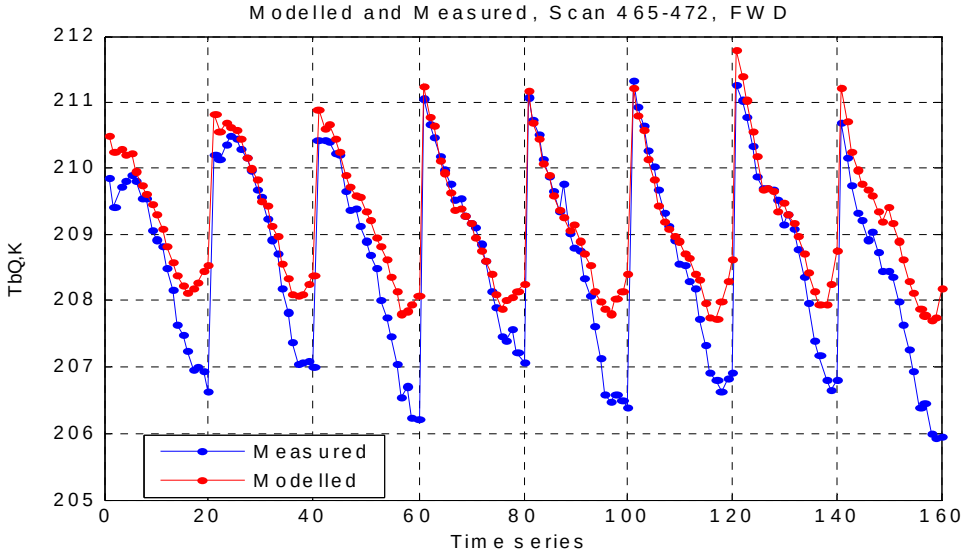

(b)

Figure 4.38 (a) Measured and modelled P Tb for Gulf of Mexico flight for FWD scene, scan 465-472. (b) Corresponding Q Tb.

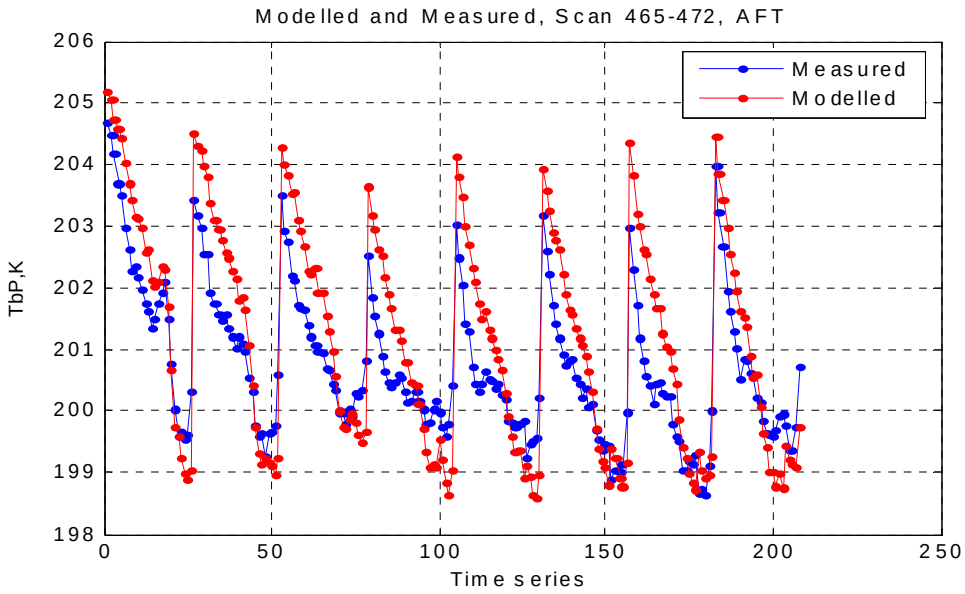

(a)

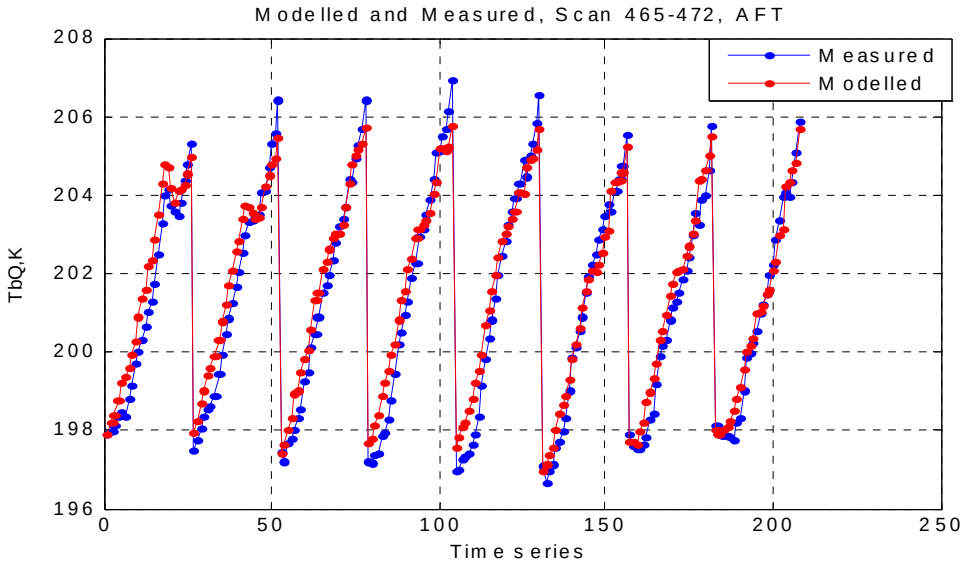

(b)

Figure 4.39 (a) Measured and modelled P Tb for Gulf of Mexico flight for AFT scene, scan 465-472. (b) Corresponding Q Tb.

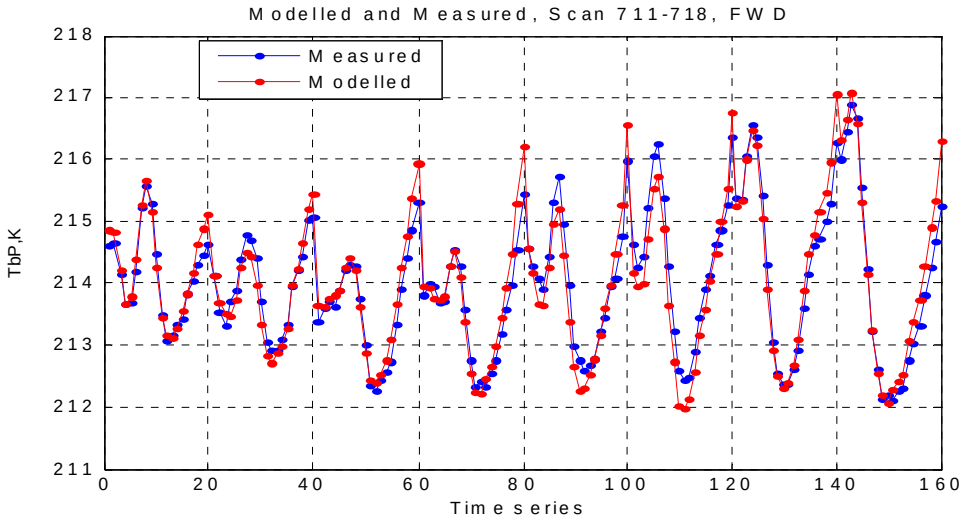

(a)

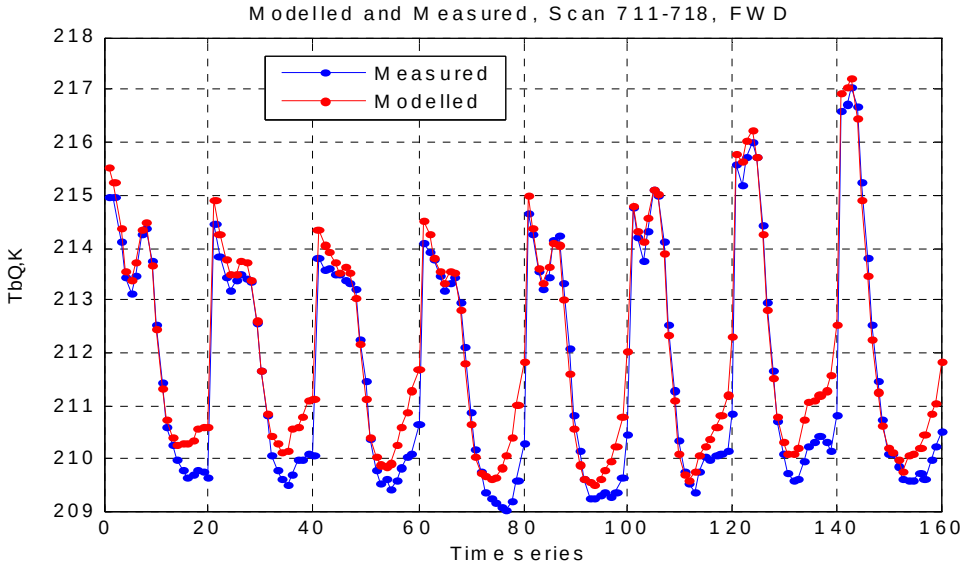

(b)

Figure 4.40 (a) Measured and modelled P Tb for Gulf of Mexico flight for FWD scene, scan 711-718. (b) Corresponding Q Tb.

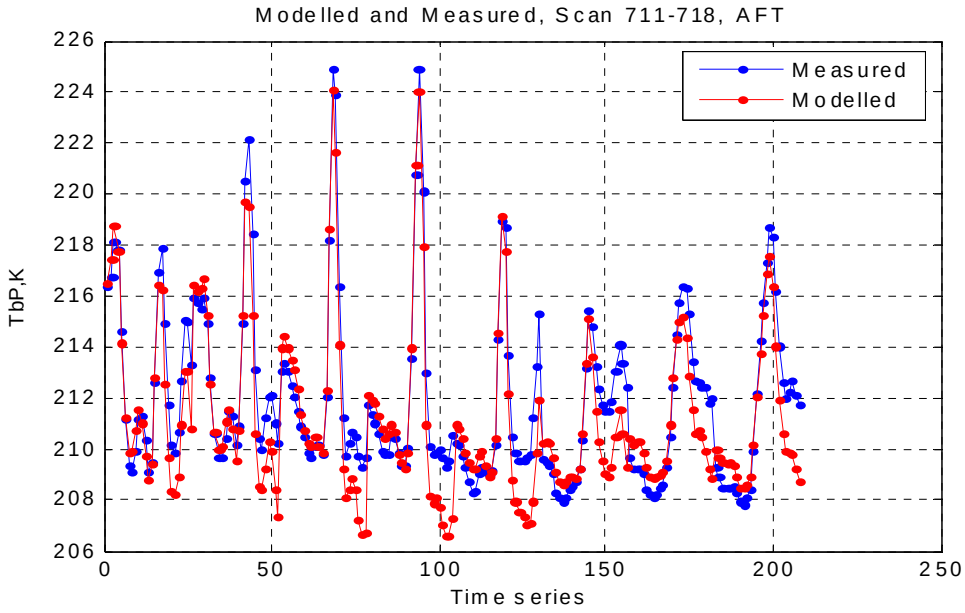

(a)

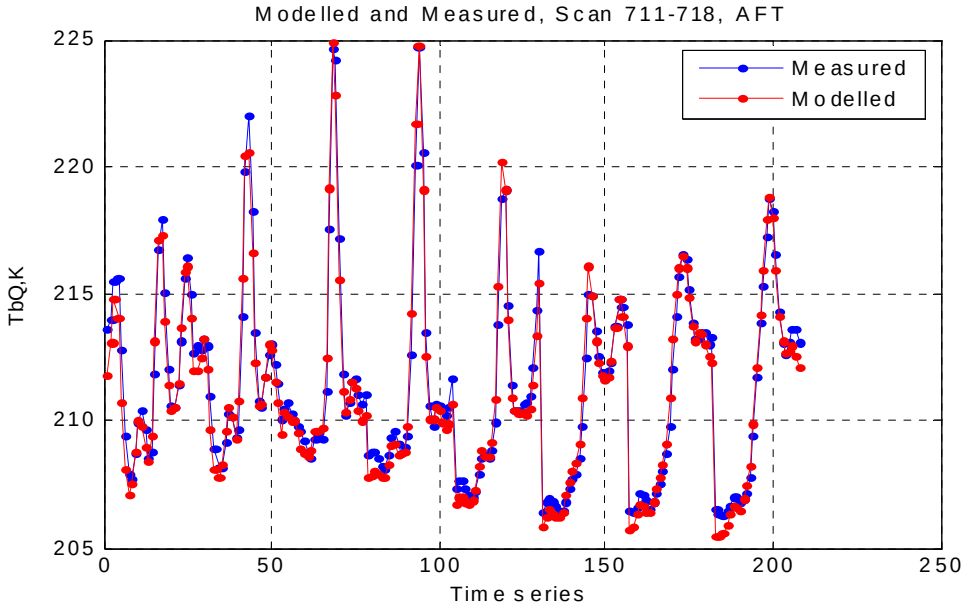

(b)

Figure 4.41 (a) Measured and modelled P Tb for Gulf of Mexico flight for AFT scene, scan 711-718. (b) Corresponding Q Tb.

A summary of the RMS differences between the modelled and measured brightness for the above scan groups is listed in the Table 4.4.

Table 4.4 RMS difference (deg) for P and Q brightness for Gulf of Mexico flight.

	Scan 1525-1532		Scan 465-472		Scan 711-718	
	Forward	Aft	Forward	Aft	Forward	Aft
RMS_P	.748	1.03	1.02	.89	.305	1.47
RMS_Q	.767	.9	.742	.59	.55	.675

CHAPTER 5: CONCLUSIONS

The intent of this thesis was to develop radiative transfer Tb models to account for platform attitude (roll and pitch) changes on measured polarized ocean brightness temperatures for a conically scanning microwave radiometer. These models were presented in chapter 3 for the V-, H-,P- and Q-polarizations. In chapter 4, these models were validated by making comparisons between modeled and measured Tb's obtained during two aircraft flights by the C-STAR (Conically Scanning Two Look Airborne Radiometer). Under clear shy conditions the comparisons were excellent; but there were difficulties experienced during heavy cloud conditions associated with a hurricane flight in the Gulf of Mexico. To accommodate these "severe" environmental conditions, algorithms were developed to model unwanted Tb variations caused heterogeneous clouds. Afterwards for all flight data examined, the effects of aircraft attitude changes on the measured brightness were effectively characterized which allowed accurate modeling of the V, H, P, and Q polarizations. Comparisons between measured and modeled brightness temperatures were presented, and results demonstrate that the analytical Tb model can accurately predict the measured polarized Tb's under actual flight conditions where the roll and pitch are accurately known.

APPENDIX A: SIMULATION CODE

Each of the files below requires the appropriate input data files; which are either processed data from the Andros flight or from the Gulf of Mexico flight. The main files are vh_andros.m, vh_hurricane.m, pq_andros.m, and pq_hurricane.m. In these, the start and stop scan number must be input for the desired scan group. Supporting files include Smooth.m, SmoothResample.m, and clouds_fwd_andros.m.

A.1 Smooth.m

```
%Running average
%Returns a smoothed version of input vector

function [y,weight]=smooth(x,wsize)

coldtb=x;
hw = ([wsize]+1)/2;
for ii = 1:length(hw)
w = linspace(1,3,hw(ii));
weight = [w,fliplr(w(1:(hw(ii)-1)))]';
Scoldtb(:,ii) = coldtb;
```

```
for k=1:length(coldtb)
   if (k>(hw(ii)-1)) & (k<length(coldtb)-(hw(ii)-2))
      psum = coldtb(k-(hw(ii)-1):k+(hw(ii)-1));
      Scoldtb(k,ii) = sum(psum.*weight)/sum(weight);
   end
end
end
y = Scoldtb;
```

A.2 SmoothResample.m

```
function [abb,ffb] = SmoothResample(camex,start,stop);

%Takes in a/c data and returns smoothed and resampled data along with az
%and scan number

[pitch,weight]=smooth(camex(:,20),5);  %smooth pitch
camex(:,20)=pitch;
[roll,weight]=smooth(camex(:,21),5);   %smooth roll
camex(:,21)=roll;
[heading,weight]=smooth(camex(:,26),5);  %smooth heading
camex(:,26)=heading;
[track,weight]=smooth(camex(:,47),5);   %smooth track
camex(:,47)=track;

%==============
a2=find(camex(:,2)>=start & camex(:,2)<=stop);
camex1=camex(a2,:);
%==============

azimuth=[]; start_az=135; new_data=[]; scan_num=[];

pitchb = interp1(1:10,camex1(:,20),linspace(1,10,104),'cubic'); %resample pitch
rollb  = interp1(1:10,camex1(:,21),linspace(1,10,104),'cubic'); %resample roll
```

```
headingb = interp1(1:10,camex1(:,26),linspace(1,10,104),'cubic'); %resample pitch
trackb  = interp1(1:10,camex1(:,47),linspace(1,10,104),'cubic'); %resample roll

for i = start:stop %generate azimuth
   for j=1:103
      if j==1
         az(i,j)=(i-1)*360 + start_az;
         azimuth=[azimuth;az(i,j)];
      else
   end
   az(i,j)=(i-1)*360 + start_az + j * (90/25);
   azimuth=[azimuth;az(i,j)];

end
   scan_num=[scan_num;i*ones(104,1)];
end

figure,plot(azimuth,rollb,'b.-');grid
figure,plot(camex(a2,21),'b.-');grid

new_data=[new_data;scan_num azimuth pitchb' rollb' headingb' trackb'];
new_data(:,2)=rem(new_data(:,2),360);

fb=find(new_data(:,2)>=315 | new_data(:,2)<=45);
ffb=new_data(fb,:);

az_300=find(ffb(:,2)>300);              %Make fwd azimuth between -50 and 50 deg
ffb(az_300,2)=ffb(az_300,2)-360;

ab=find(new_data(:,2)>=135 & new_data(:,2)<=225);
abb=new_data(ab(1:26),:);
```

A.3 clouds_fwd_andros.m

```
%Remove clouds for fwd scene.

clear all;
load  camex_200108230_TB_fwd_v3_1.dat;
fwd = camex_200108230_TB_fwd_v3_1;
```

```
% X=fwd(:,1)+15;  %colocate fore and aft pixels(difference between for and aft is 15
scans)
% fwd(:,1)=X;

fwd(:,7)=rem(fwd(:,7),360);            %Convert azimuth values to between 0 and 360
az_300=find(fwd(:,7)>300);             %Make fwd azimuth between -50 and 50 deg
fwd(az_300,7)=fwd(az_300,7)-360;

fwd_180=find(fwd(:,1)>=180 & fwd(:,1)<280); %Select scan numbers to process
fwd_180=fwd(fwd_180,:);

del_hv=fwd_180(:,8)-fwd_180(:,9);              %Difreence between H and V pol
% figure,plot(fwd_180(:,7),del_hv,'.');grid;

c=length(del_hv)/26;

HV = reshape(del_hv,26,c);
AZ = reshape(fwd_180(:,7),26,c);
% figure,plot(AZ,HV,'b.'),grid,hold;

HV_std = std(HV');
HV_mean = mean(HV,2);

%plot(mean(AZ,2),mean(HV,2),'om');          %mean of each azimuth bin
%plot(mean(AZ,2),std(HV')+35,'r');          %std deviation of each azimuth bin
 figure, subplot(2,1,1),
 plot(AZ,HV,'b.'),grid,hold;title('180-280')
 errorbar(mean(AZ,2),mean(HV,2),std(HV'),'r');

 S=[];st_dev=[];
 for i=180:279  %Make Standard Deviation same length as rest of data
    w=find(fwd_180(:,1)==i);
    len=length(w);
    S=HV_std';
    st_dev=[st_dev; S.*ones(len,1)];
end

M=[];MEAN=[];
 for i=180:279  %Make mean same length as rest of data
    w=find(fwd_180(:,1)==i);
    len=length(w);
    M=HV_mean;
    MEAN=[MEAN; M.*ones(len,1)];
end

%  1:21  22.del hv  23.mean  24.std deviation
```

```
fwd_180=[fwd_180 del_hv MEAN st_dev];

%  ms_plus = fwd_180(:,13)+3*fwd_180(:,14);  %mean + .5 std deviation
 ms_minus = fwd_180(:,23)-1*fwd_180(:,24); %mean - .5 std deviation

 hv_edit = find(fwd_180(:,22) <= ms_minus);  %Convert clouds to NaN
 fwd_180(hv_edit,:)=NaN;
 hv_edit = fwd_180;

cloudedit=hv_edit;                %cloudedit is new matrix to be used

 subplot(2,1,2),
 plot(cloudedit(:,7),cloudedit(:,22),'.');grid;
```

A.4 vh_andros.m

```
%Model V and H pols for fwd scene
clear all;
 load  camex_200108230_TB_fwd_v3_1.dat; fwd=camex_200108230_TB_fwd_v3_1;
 load  camex_200108230_TB_aft_v3_1.dat; aft=camex_200108230_TB_aft_v3_1;

 v_poly=[-1.3312e-004 0.0064 0.4093]; %Vector for reflection coeff polyfit for v pol
 h_poly=[4.9242e-005 5.5964e-005 0.5363];%Vector for reflection coeff polyfit for h pol
% ========================================
% required vectors
 tb=[];
 azimuthA=[]; start_az=135; new_data=[]; scan_num=[];error_v=[];error_h=[];
 series=[];series_a=[];error_v_a=[];error_h_a=[];

% gamma_h=0.635;
% gamma_v=0.36;
tau=0.778;  %Atmospheric transmissivity
tdn_c=67.4; %Downwelling brightness

tv_surface=193.8; %Vertical surface brightness for fwd
th_surface=106.8; %Horizontal surface brightness for fwd

tv_surface_a=191.5;%Vertical surface brightness for aft
th_surface_a=108.2;%Horizontal surface brightness for aft
```

```
sst=29;
  % ========================================

 load cstar_2001230_nav3.txt;
 camex0=cstar_2001230_nav3;
s=find(camex0(:,1)>=360 & camex0(:,1)<=25104);
camex=camex0(s,:);

% % ========================================
% % shift roll and pitch  down k elements
k=11; %time delay
roll=camex(:,21)+0.5;
camex(:,21)=roll([end-k+1:end 1:end-k]);
pitch=camex(:,20)+0.5;
camex(:,20)=pitch([end-k+1:end 1:end-k]);

scan_start=175; %Start scan
scan_stop=175; %Stop scan

% ========================================

for start=scan_start:scan_stop;
stop=start;

%========================================
%find data for scan of interest
f=find(fwd(:,1)>=start & fwd(:,1)<=stop);
a=find(aft(:,1)>=start & aft(:,1)<=stop);

a2=find(camex(:,2)>=start & camex(:,2)<=stop);

ff=fwd(f,:);
aa=aft(a,:);
camex1=camex(a2,:);

%========================================
%Convert azimuth values to between 0 and 360
ff(:,7)=rem(ff(:,7),360);
aa(:,7)=rem(aa(:,7),360);
%========================================
%tb to be used in incidence
tbv_mean=repmat(220,size(ff,1),1) ;%*********
tbh_mean=repmat(170,size(ff,1),1) ;

%========================================
%column 22 and 23 are now tbv_mean and tbh_mean respectively
```

```
ff=[ff tbv_mean tbh_mean];   %fwd
aa=[aa tbv_mean tbh_mean];   %aft

%Make fwd azimuth between -50 and 50 deg
az_300=find(ff(:,7)>300);
ff(az_300,7)=ff(az_300,7)-360;

%fwd, remove 6 outlying az pts
a25=find(ff(:,7)>=25);
ff(a25,:)=NaN;

%In aft scene for scans 520-527, removed land contaminated brightness
% a190=find(aa(:,7)>=190);
% aa(a190,:)=NaN;
%=========================================%Incidence angle correction
% a=find(camex(:,2)==start);
% figure,plot(camex(a,21),'.-');grid;hold

%==========
%Smooth and resample aircraft attitude
[abb,ffb] = SmoothResample(camex,start,stop);
%==========

%  slope_v=2.04 ; slope_h=-0.54;
slope_v=2.22 ; slope_h=0.18;  %Rate of change of brightness with respect to incidence

mean_inc=53.3;

roll = ffb(:,4); %roll vector  %fwd
pitch = ffb(:,3); %pitch vector
azimuth = ffb(:,2).*(pi/180); %az in rad

roll_a = abb(:,4); %roll vector  %aft
pitch_a = abb(:,3); %pitch vector
azimuth_a = abb(:,2).*(pi/180); %az in rad

theta_i = mean_inc + pitch.*cos(azimuth) - roll.*sin(azimuth); %Theta(i) to be used in
incidence correction, fwd
theta_i_a = mean_inc + pitch_a.*cos(azimuth_a) - roll_a.*sin(azimuth_a); %Theta(i) to
be used in incidence correction, aft


ff=[ff theta_i]; % column 24 is theta(i), aft
aa=[aa theta_i_a]; % column 24 is theta(i). fwd

theta_corrected=[];
```

```
theta_corrected_a=[];

for jj= start:stop
scan11=ff(:,:);
scan11_a=aa(:,:);
if length(scan11)>0
       %1:21 ff 25: V inc corrected 26: H inc corrected 27:delta_theta
        theta_corrected=[theta_corrected; scan11,  scan11(:,8) - (scan11(:,24)-
(mean_inc)).*slope_v,  scan11(:,9) - (scan11(:,24)-(mean_inc)).*slope_h, scan11(:,24)-
(mean_inc)];%fwd
%          theta_corrected=[theta_corrected; scan11,  scan11(:,8) +
(scan11(:,24)).*slope_v,  scan11(:,9) + (scan11(:,24)).*slope_h];
        theta_corrected_a=[theta_corrected_a; scan11_a,  scan11_a(:,8) - (scan11_a(:,24)-
(mean_inc)).*slope_v,  scan11_a(:,9) - (scan11_a(:,24)-(mean_inc)).*slope_h,
scan11_a(:,24)-(mean_inc)];%aft

   else end
end
%=========================================
%Model with incidence correction
Tbv = theta_corrected(:,25); %Tbv vector, fwd
Tbh = theta_corrected(:,26); %Tbh vector

Tbv_a = theta_corrected_a(:,25); %Tbv vector, aft
Tbh_a = theta_corrected_a(:,26); %Tbh vector
%=========================================

tatmos_v = (Tbv- ((sst+273)*(1-gamma_v)*tau))./(1+tau*gamma_v);%aft
tatmos_h = (Tbh- ((sst+273)*(1-gamma_h)*tau))./(1+tau*gamma_h);

tatmos_v_a = (Tbv_a- ((sst+273)*(1-gamma_v)*tau))./(1+tau*gamma_v);%fwd
tatmos_h_a = (Tbh_a- ((sst+273)*(1-gamma_h)*tau))./(1+tau*gamma_h);

% tatmos=nanmean([tatmos_v tatmos_h],2);
% tatmos_a=nanmean([tatmos_v_a tatmos_h_a],2);
%=========================================

rhov=polyval(v_poly,theta_corrected(:,24));%aft
rhoh=polyval(h_poly,theta_corrected(:,24));

rhov_a=polyval(v_poly,theta_corrected_a(:,24));%fwd
rhoh_a=polyval(h_poly,theta_corrected_a(:,24));

%=========================================
v_model = tatmos_v + tatmos_v .* rhov.*tau + tv_surface*tau +
slope_v.*theta_corrected(:,27);%fwd
```

```
h_model = tatmos_h + tatmos_h .* rhoh.*tau + th_surface*tau +
slope_h.*theta_corrected(:,27);

v_model_a = tatmos_v_a + tatmos_v_a .* rhov_a.*tau + tv_surface_a*tau +
slope_v.*theta_corrected_a(:,27);%aft
h_model_a = tatmos_h_a + tatmos_h_a .* rhoh_a.*tau + th_surface_a*tau +
slope_h.*theta_corrected_a(:,27);

%=========================================

series=[series;ff(1:20,8),ff(1:20,9),v_model(1:20),h_model(1:20), azimuth(1:20),
pitch(1:20), roll(1:20), Tbv(1:20), Tbh(1:20), tatmos_v(1:20),tatmos_h(1:20) ,rhov(1:20)
,rhoh(1:20), theta_corrected(1:20,24), v_model(1:20), h_model(1:20), tatmos(1:20),
slope_v.*theta_corrected(1:20,27),slope_h.*theta_corrected(1:20,27)]; %fwd
series_a=[series_a;aa(1:26,8),aa(1:26,9),v_model_a(1:26),h_model_a(1:26),
azimuth_a(1:26), pitch_a(1:26), roll_a(1:26), Tbv_a(1:26), Tbh_a(1:26),
tatmos_v_a(1:26),tatmos_h_a(1:26) ,rhov_a(1:26) ,rhoh_a(1:26),
theta_corrected_a(1:26,24), v_model_a(1:26), h_model_a(1:26), tatmos_a(1:26),
slope_v.*theta_corrected_a(1:26,27),slope_h.*theta_corrected_a(1:26,27)]; %aft

end

%%%%%%%%%%%%%%%%%%%%%%%%%%%%%%%%%%%%%%%%%%%%%%%%%%%%%%%%%%%%%%%%%%%%%%%%%%%%
%Fwd
  figure,plot(series(:,1),'.-r');grid;hold
  plot(series(:,15),'.-');
  xlabel('Time series');ylabel('TbV,K');title('Modelled and Measured, Scan 520-526,
FWD'); legend('Measured','Modelled');
 axis([0 160 229 240]);

 figure,plot(series(:,2),'.-r');grid;hold
 plot(series(:,16),'.-');
 xlabel('Time series');ylabel('TbH,K');title('Modelled and Measured, Scan 520-526,
FWD'); legend('Measured','Modelled');
axis([0 160 175 182]);

%Aft

  figure,plot(series_a(:,1),'.-r');grid;hold
  plot(series_a(:,15),'.-');
  xlabel('Time series');ylabel('TbV,K');title('Modelled and Measured, Scan 520-526,
AFT'); legend('Measured','Modelled');
  axis([0 208 223 233]);


 figure,plot(series_a(:,2),'.-r');grid;hold
```

```
 plot(series_a(:,16),'.-');
 xlabel('Time series');ylabel('TbH,K');title('Modelled and Measured, Scan 520-526,
AFT'); legend('Measured','Modelled');
 axis([0 208 174 179]);
```

A.5 vh_hurricane.m

```
%Model V and H pols for hurricane flight
clear all;
 load  camex_200108232_TB_fwd_v3_1.dat; fwd=camex_200108232_TB_fwd_v3_1;
 load  camex_200108232_TB_aft_v3_1.dat; aft=camex_200108232_TB_aft_v3_1;

 %quadratic poly coeffs
 v_poly=[-1.0893e-004 0.0046 0.4339];
 h_poly=[5.0000e-005 -3.5000e-004 0.5334];
% ========================================
% required vectors
 tb=[];
 azimuthA=[]; start_az=135; new_data=[]; scan_num=[];error_v=[];error_h=[];
 series=[];series_a=[];error_v_a=[];error_h_a=[];

gamma_h=0.645;
gamma_v=0.42;
tau=0.778;
tdn_c=67.4;
sst=29;

tv_surface=180;
th_surface=105;

tv_surface_a=177;
th_surface_a=107.5;
```

```
 % ==========================================

load cstar_2001232_nav3.txt;
camex0=cstar_2001232_nav3;
s=find(camex0(:,1)>=360 & camex0(:,1)<=25104);
camex=camex0(s,:);

% % ==========================================
% % shift roll and pitch  down k elements
k=11;
roll=camex(:,21)+0.5;
camex(:,21)=roll([end-k+1:end 1:end-k]);
pitch=camex(:,20)+0.5;
camex(:,20)=pitch([end-k+1:end 1:end-k]);

% scan_start=1525-12;
% scan_stop=1532-12;
scan_start=711;
scan_stop=718;
% ==========================================

for start=scan_start:scan_stop;
stop=start;

%==========================================
%find data for scan of interest
f=find(fwd(:,1)>=start & fwd(:,1)<=stop);
a=find(aft(:,1)>=start & aft(:,1)<=stop);

a2=find(camex(:,2)>=start & camex(:,2)<=stop);

ff=fwd(f,:);
aa=aft(a,:);

camex1=camex(a2,:);

%==========================================
%Convert azimuth values to between 0 and 360
ff(:,7)=rem(ff(:,7),360);
aa(:,7)=rem(aa(:,7),360);

%==========================================
%tb to be used in incidence
tbv_mean=repmat(220,size(ff,1),1) ;%*********
tbh_mean=repmat(170,size(ff,1),1) ;
```

```
%=========================================
%column 22 and 23 are now tbv_mean and tbh_mean respectively
ff=[ff tbv_mean tbh_mean];   %fwd
aa=[aa tbv_mean tbh_mean];   %aft

%Make fwd azimuth between -50 and 50 deg
az_300=find(ff(:,7)>300);
ff(az_300,7)=ff(az_300,7)-360;

%fwd, remove 6 outlying az pts
a25=find(ff(:,7)>=25);
ff(a25,:)=NaN;

%=========================================%Incidence angle correction
%==========
[abb,ffb] = SmoothResample(camex,start,stop);
%==========

%  slope_v=2.04 ; slope_h=-0.54;
slope_v=2.22 ; slope_h=0.18;

mean_inc=53.3;

roll = ffb(:,4); %roll vector  %fwd
pitch = ffb(:,3); %pitch vector
azimuth = ffb(:,2).*(pi/180); %az in rad

roll_a = abb(:,4); %roll vector  %fwd
pitch_a = abb(:,3); %pitch vector
azimuth_a = abb(:,2).*(pi/180); %az in rad

 theta_i = mean_inc + pitch.*cos(azimuth) - roll.*sin(azimuth); %Theta(i) to be used in
incidence correction
 theta_i_a = mean_inc + pitch_a.*cos(azimuth_a) - roll_a.*sin(azimuth_a); %Theta(i) to
be used in incidence correction

ff=[ff theta_i]; % column 24 is theta(i)
aa=[aa theta_i_a]; % column 24 is theta(i)

theta_corrected=[];
theta_corrected_a=[];

for jj= start:stop
scan11=ff(:,:);
scan11_a=aa(:,:);
```

```
if length(scan11)>0
      %1:21 ff 25: V inc corrected 26: H inc corrected 27:delta_theta
        theta_corrected=[theta_corrected; scan11,  scan11(:,8) - (scan11(:,24)-
(mean_inc)).*slope_v,  scan11(:,9) - (scan11(:,24)-(mean_inc)).*slope_h, scan11(:,24)-
(mean_inc)];%fwd
%         theta_corrected=[theta_corrected; scan11,  scan11(:,8) +
(scan11(:,24)).*slope_v,  scan11(:,9) + (scan11(:,24)).*slope_h];
        theta_corrected_a=[theta_corrected_a; scan11_a,  scan11_a(:,8) - (scan11_a(:,24)-
(mean_inc)).*slope_v,  scan11_a(:,9) - (scan11_a(:,24)-(mean_inc)).*slope_h,
scan11_a(:,24)-(mean_inc)];%aft

   else end
end
%=========================================
%Model with incidence correction
%fwd
Tbv = theta_corrected(:,25); %Tbv vector
Tbh = theta_corrected(:,26); %Tbh vector
%aft
Tbv_a = theta_corrected_a(:,25); %Tbv vector
Tbh_a = theta_corrected_a(:,26); %Tbh vector

%=========================================
%fwd
tatmos_v = (Tbv- ((sst+273)*(1-gamma_v)*tau))./(1+tau*gamma_v);
tatmos_h = (Tbh- ((sst+273)*(1-gamma_h)*tau))./(1+tau*gamma_h);
%aft
tatmos_v_a = (Tbv_a- ((sst+273)*(1-gamma_v)*tau))./(1+tau*gamma_v);
tatmos_h_a = (Tbh_a- ((sst+273)*(1-gamma_h)*tau))./(1+tau*gamma_h);

% tatmos=nanmean([tatmos_v tatmos_h],2);
% tatmos_a=nanmean([tatmos_v_a tatmos_h_a],2);

%=========================================
%fwd
rhov=polyval(v_poly,theta_corrected(:,24));
rhoh=polyval(h_poly,theta_corrected(:,24));

%aft
rhov_a=polyval(v_poly,theta_corrected_a(:,24));
rhoh_a=polyval(h_poly,theta_corrected_a(:,24));

%=========================================
%fwd
```

```
v_model = tatmos_v + tatmos_v .* rhov.*tau + tv_surface*tau +
slope_v.*theta_corrected(:,27);
h_model = tatmos_h + tatmos_h .* rhoh.*tau + th_surface*tau +
slope_h.*theta_corrected(:,27);

%aft
v_model_a = tatmos_v_a + tatmos_v_a .* rhov_a.*tau + tv_surface_a*tau +
slope_v.*theta_corrected_a(:,27);
h_model_a = tatmos_h_a + tatmos_h_a .* rhoh_a.*tau + th_surface_a*tau +
slope_h.*theta_corrected_a(:,27);

%=========================================

series=[series;ff(1:20,8),ff(1:20,9),v_model(1:20),h_model(1:20), azimuth(1:20),
pitch(1:20), roll(1:20), Tbv(1:20), Tbh(1:20), tatmos_v(1:20) ,tatmos_h(1:20) ,rhov(1:20)
,rhoh(1:20), theta_corrected(1:20,24), v_model(1:20), h_model(1:20),
tatmos(1:20),slope_v.*theta_corrected(1:20,27),slope_h.*theta_corrected(1:20,27)];
%fwd
series_a=[series_a;aa(1:26,8),aa(1:26,9),v_model_a(1:26),h_model_a(1:26),
azimuth_a(1:26), pitch_a(1:26), roll_a(1:26), Tbv_a(1:26), Tbh_a(1:26),
tatmos_v_a(1:26),tatmos_h_a(1:26) ,rhov_a(1:26) ,rhoh_a(1:26),
theta_corrected_a(1:26,24), v_model_a(1:26), h_model_a(1:26), tatmos_a(1:26),
slope_v.*theta_corrected_a(1:26,27),slope_h.*theta_corrected_a(1:26,27)]; %aft


end

 %%%%%%%%%%%%%%%%%%%%%%%%%%%%%%%%%%%%%%%%%%%%%%%%%%%%%%%%%%%%%%%%%%%%%%%%%%%%%%%%
% figure,plot(series(:,1),'.-');grid;hold
% plot(series(:,8),'.-r');title('Inc Normalization, V pol'),legend('Measured','Normalized');
% figure,plot(series(:,2),'.-');grid;hold
% plot(series(:,9),'.-r');title('Inc Normalization, H pol'),legend('Measured','Normalized');
%
% %
%  figure,plot(series(:,5).*(180/pi),series(:,10),'.');grid;hold
%  plot(series(:,5).*(180/pi),series(:,11),'*r');title('Tatmos'),legend('V pol','H pol');
% figure,plot(series(:,10),'.');grid;hold
% plot(series(:,11),'*r');title('Atmospheric brightness, Scan 1525-1532'),legend('V pol','H
pol');
% xlabel('Time series'),ylabel('Tb, K')
% axis([0 160 50 100]);

% plot(series(:,17),'.-k');
% figure,plot(series(:,14), series(:,12),'.-');grid;hold
% plot(series(:,14), series(:,13),'.-r');title('refl coeff')
```

```
 figure,plot(series(:,1),'.-r');grid;hold
 plot(series(:,15),'.-');
 xlabel('Time series');ylabel('TbV,K');title('Modelled and Measured, Scan 711-718,
FWD'); legend('Measured','Modelled');
%  axis([0 160 225 250]);

 figure,bar(711:718,error_v);grid,title('Difference between measured V and modelled V,
FWD'),
xlabel('Scan Number'),ylabel('RMS Error')

 figure,plot(series(:,2),'.-r');grid;hold
 plot(series(:,16),'.-');
 xlabel('Time series');ylabel('TbH,K');title('Modelled and Measured, Scan 711-718,
FWD'); legend('Measured','Modelled');
% axis([0 160 175 225]);

 figure,bar(711:718,error_h);grid,title('Difference between measured H and modelled H,
FWD'),
xlabel('Scan Number'),ylabel('RMS Error')

%Aft

 figure,plot(series_a(:,1),'.-r');grid;hold
 plot(series_a(:,15),'.-');
 xlabel('Time series');ylabel('TbV,K');title('Modelled and Measured, Scan 711-718,
AFT'); legend('Measured','Modelled');
%   axis([0 208 223 233]);

 figure,bar(711:718,error_v_a);grid,title('Difference between measured V and modelled
V, AFT'),
xlabel('Scan Number'),ylabel('RMS Error')

 figure,plot(series_a(:,2),'.-r');grid;hold
 plot(series_a(:,16),'.-');
 xlabel('Time series');ylabel('TbH,K');title('Modelled and Measured, Scan 711-718,
AFT'); legend('Measured','Modelled');
%  axis([0 208 174 179]);

 figure,bar(711:718,error_h_a);grid,title('Difference between measured H and modelled
H, AFT'),
xlabel('Scan Number'),ylabel('RMS Error')
```

A.6 pq_Andros.m

```
%To model +- 45 pols for Andros island
clear all;

%Vectors to determine refflection coeficient for given incidence angle
 v_poly=[-1.3312e-004 0.0064 0.4093];
 h_poly=[4.9242e-005 5.5964e-005 0.5363];

%==============================================
%required vectors
azimuthA=[]; start_az=135; new_data=[];
scan_num=[];error_v=[];error_h=[];;series_fwd=[];series_aft=[];
corrected_p_fwd=[];corrected_q_fwd=[]; corrected_p_aft=[]; corrected_q_aft=[];
Bestv=[]; Besth=[];
error_v_aft=[];error_h_aft=[];
incidence_fwd=[];incidence_aft=[];
series_stokes_fwd=[];series_stokes_aft=[];
%==============================================

%Required data
load  camex_200108230_TB_fwd_v3_1.dat;% processed fwd data
load  camex_200108230_TB_aft_v3_1.dat;% processed aft data

fwd = camex_200108230_TB_fwd_v3_1;
aft = camex_200108230_TB_aft_v3_1;

gamma_h=0.635;  %Reflection coefficient for H pol
gamma_v=0.36;   %Reflection coefficient for V pol
tau=0.778;      %Atmospheric transmitivity
tdn_c=67.4;     %Downwelling brightness

tv_surface=197; %Surface brightness for V pol for fwd scene
th_surface=109; %Surface brightness for H pol for fwd scene

tv_surface_aft=188; %Surface brightness for V pol for aft scene
th_surface_aft=102; %Surface brightness for H pol for aft scene

sst=29; %Sea surface temperature

load cstar_2001230_nav3.txt; %Aircraft data
camex0=cstar_2001230_nav3;
s=find(camex0(:,1)>=360 & camex0(:,1)<=25104);
camex=camex0(s,:);
```

```
%==========================================
%shift roll and pitch  down k elements
k=11;   % Time delay
roll=camex(:,21)+0.5; %Roll bias
camex(:,21)=roll([end-k+1:end 1:end-k]);
pitch=camex(:,20)+0.5;%Pitch bias
camex(:,20)=pitch([end-k+1:end 1:end-k]);

heading=camex(:,26);
camex(:,26)=heading([end-k+1:end 1:end-k]);

track=camex(:,47);
camex(:,47)=track([end-k+1:end 1:end-k]);
%==========================================
 eps=[];

%Scan group
scan_start=520; %Start scan
scan_stop=526; %Stop scan

for start=scan_start:scan_stop;
stop=start;

%==============================================

  v_fwd=225;
  h_fwd=182;

%==============================================
%find data for scan of interest
f=find(fwd(:,1)>=start & fwd(:,1)<=stop);
a=find(aft(:,1)>=start & aft(:,1)<=stop);
a2=find(camex(:,2)>=start & camex(:,2)<=stop);

ff=fwd(f,:);
aa=aft(a,:);
camex1=camex(a2,:);

%==============================================
%Convert azimuth values to between 0 and 360
ff(:,7)=rem(ff(:,7),360);
aa(:,7)=rem(aa(:,7),360);

%==============================================
%tb to be used in incidence
 tbv_mean_fwd=repmat(v_fwd,26,1) ;
```

```
 tbh_mean_fwd=repmat(h_fwd,26,1) ;

%================================================
%column 22 and 23 are now tbv_mean and tbh_mean respectively
ff=[ff tbv_mean_fwd tbh_mean_fwd];   %fwd
aa=[aa tbv_mean_fwd tbh_mean_fwd];   %aft

%Make fwd azimuth between -50 and 50 deg
az_300=find(ff(:,7)>300);
ff(az_300,7)=ff(az_300,7)-360;

%fwd, remove 6 outlying az pts
 a25=find(ff(:,7)>=25);
 ff(a25,:)=NaN;

 %In aft scene for scans 520-527, removed land contaminated brightness
%  a190=find(aa(:,7)>=190);
%  aa(a190,:)=NaN;

%================================================
%Incidence angle correction
%===========
[abb,ffb] = SmoothResample(camex,start,stop);
%===========

% slope_v=2.04 ; slope_h=-0.54;
slope_v=2.22 ; slope_h=0.18;

mean_inc=53.3;

heading_fwd=ffb(:,5);%heading fwd
track_fwd=ffb(:,6);%track fwd
roll_fwd = ffb(:,4); %roll vector   %fwd
pitch_fwd = ffb(:,3); %pitch vector
azimuth_fwd = ffb(:,2).*(pi/180); %az in rad

heading_aft=abb(:,5);%heading aft
track_aft=abb(:,6);%track aft
roll_aft = abb(:,4); %roll vector  %aft
pitch_aft = abb(:,3); %pitch vector
azimuth_aft = abb(:,2).*(pi/180); %az in rad

theta_i_fwd = mean_inc + pitch_fwd.*cos(azimuth_fwd) - roll_fwd.*sin(azimuth_fwd);
%Theta(i) to be used in incidence correction
theta_i_aft = mean_inc + pitch_aft.*cos(azimuth_aft) - roll_aft.*sin(azimuth_aft);
%Theta(i) to be used in incidence correction
```

```
ff=[ff theta_i_fwd]; % column 24 is theta(i)
aa=[aa theta_i_aft];

theta_corrected_fwd=[];
theta_corrected_aft=[];

for jj= start:stop
scan11_fwd=ff(:,:);
scan11_aft=aa(:,:);

      %1:21 ff 25: V inc corrected 26: H inc corrected
       theta_corrected_fwd=[theta_corrected_fwd; scan11_fwd,  scan11_fwd(:,8) -
(scan11_fwd(:,24)-(mean_inc)).*slope_v,  scan11_fwd(:,9) - (scan11_fwd(:,24)-
(mean_inc)).*slope_h];
%        theta_corrected_fwd=[theta_corrected_fwd; scan11_fwd,  scan11_fwd(:,22) +
(scan11_fwd(:,24)).*slope_v,  scan11_fwd(:,23) + (scan11_fwd(:,24)).*slope_h];

       theta_corrected_aft=[theta_corrected_aft; scan11_aft,  scan11_aft(:,8) -
(scan11_aft(:,24)-(mean_inc)).*slope_v,  scan11_aft(:,9) - (scan11_aft(:,24)-
(mean_inc)).*slope_h];
end

%================================================================
==========

Tbv_fwd = theta_corrected_fwd(:,25); %Tbv vector, Fwd
Tbh_fwd = theta_corrected_fwd(:,26); %Tbh vector

Tbv_aft = theta_corrected_aft (:,25); %Tbv vector, Aft
Tbh_aft = theta_corrected_aft (:,26); %Tbh vector

incidence_fwd=[incidence_fwd;theta_corrected_fwd(:,8) theta_corrected_fwd(:,9)
Tbv_fwd Tbh_fwd];
incidence_aft=[incidence_aft;theta_corrected_aft(:,8) theta_corrected_aft(:,9) Tbv_aft
Tbh_aft];

%================================================================
=========
%Atmospheric brightness for fwd scene
tatmos_v = (Tbv_fwd - ((sst+273)*(1-gamma_v)*tau))./(1+tau*gamma_v);
tatmos_h = (Tbh_fwd - ((sst+273)*(1-gamma_h)*tau))./(1+tau*gamma_h);

%Atmospheric brightness for aft scene
tatmos_v_aft = (Tbv_aft- ((sst+273)*(1-gamma_v)*tau))./(1+tau*gamma_v);
tatmos_h_aft = (Tbh_aft- ((sst+273)*(1-gamma_h)*tau))./(1+tau*gamma_h);
```

```
%Mean atmospheric brightness
% tatmos=nanmean([tatmos_v tatmos_h],2);
% tatmos_aft=nanmean([tatmos_v_aft tatmos_h_aft],2);
%=========================================
%Reflection coefficient for fwd scene
rhov=polyval(v_poly,theta_corrected_fwd(:,24));
rhoh=polyval(h_poly,theta_corrected_fwd(:,24));

%Reflection coefficient for aft scene
rhov_aft=polyval(v_poly,theta_corrected_aft(:,24));
rhoh_aft=polyval(h_poly,theta_corrected_aft(:,24));

%==================================
%Modeled brightness for fwd scene
v_model = tatmos_v + tatmos_v .* rhov.*tau + tv_surface*tau ;
h_model = tatmos_h + tatmos_h .* rhoh.*tau + th_surface*tau ;

%Modeled brightness for aft scene
v_model_aft = tatmos_v_aft + tatmos_v_aft .* rhov_aft.*tau + tv_surface_aft*tau;
h_model_aft = tatmos_h_aft + tatmos_h_aft .* rhoh_aft.*tau + th_surface_aft*tau;

%=========================================

e=0.9087; %Horn rotation error

gamma_fwd = (roll_fwd.*cos(azimuth_fwd) + pitch_fwd.*sin(azimuth_fwd)).*(pi/180);
%Gammas in radian, Fwd (PRA)
beta_p_fwd=((45+e)*(pi/180))+gamma_fwd; %Betas in radians
beta_q_fwd=((-45+e)*(pi/180))+gamma_fwd;

gamma_aft = (roll_aft.*cos(azimuth_aft) + pitch_aft.*sin(azimuth_aft)).*(pi/180);
%Gammas in radian, Aft (PRA)
beta_p_aft=((45+e)*(pi/180))+gamma_aft; %Betas in radians
beta_q_aft=((-45+e)*(pi/180))+gamma_aft;

%=================================================================
==========
tbp_sim_fwd = h_model .*  (cos(beta_p_fwd)).^2 + v_model .* (sin(beta_p_fwd)).^2;
%Fwd
tbq_sim_fwd = h_model .*  (cos(beta_q_fwd)).^2 + v_model .* (sin(beta_q_fwd)).^2;

%=================================================================
==========
```

```
tbp_sim_aft = h_model_aft .*  (cos(beta_p_aft)).^2 + v_model_aft .*
(sin(beta_p_aft)).^2; %Aft
tbq_sim_aft = h_model_aft .*  (cos(beta_q_aft)).^2 + v_model_aft .*
(sin(beta_q_aft)).^2;

yaw_fwd=heading_fwd-track_fwd;
yaw_aft=heading_aft-track_aft;

%1:measP 2:measQ 3:simP 4:simQ 5:az 6:pitch 7:roll
series_fwd=[series_fwd;ff(1:20,10), ff(1:20,11), tbp_sim_fwd(1:20), tbq_sim_fwd(1:20),
azimuth_fwd(1:20), pitch_fwd(1:20), roll_fwd(1:20), yaw_fwd(1:20),
theta_i_fwd(1:20)]; %fwd
series_aft=[series_aft;aa(1:26,10), aa(1:26,11), tbp_sim_aft(1:26), tbq_sim_aft(1:26),
azimuth_aft(1:26), pitch_aft(1:26), roll_aft(1:26), yaw_aft(1:26), theta_i_aft(1:26)]; %aft

end

%fwd
figure,plot(series_fwd(:,1),'.-');grid;hold
plot(series_fwd(:,3),'r.-')
xlabel('Time series');ylabel('TbP,K');title(' Modelled and Measured, Scan 887-893,
FWD');
legend('Measured','Modelled');

figure,plot(series_fwd(:,2),'.-');grid;hold
plot(series_fwd(:,4),'r.-')
xlabel('Time series');ylabel('TbQ,K');title(' Modelled and Measured, Scan 887-893,
FWD');
legend('Measured','Modelled');

%Aft
%
%  figure,plot(series_aft(:,1),'.-');grid;hold
%  plot(series_aft(:,3),'r.-')
%  xlabel('Time series');ylabel('TbP,K');title(' Modelled and Measured, Scan 520-526,
AFT');
% legend('Measured','Modelled');
%
%  figure,plot(series_aft(:,2),'.-');grid;hold
%  plot(series_aft(:,4),'r.-')
%  xlabel('Time series');ylabel('TbQ,K');title(' Modelled and Measured, Scan 520-526,
AFT');
%  legend('Measured','Modelled');
%
```

A.7 pq_hurricane.m

```
%To model +- 45 pols for hurricane flight
clear all;

%================================================
%required vectors
azimuthA=[];series_fwd_trial=[]; start_az=135; new_data=[];
scan_num=[];error_p=[];error_q=[];series_fwd=[];
corrected_p_fwd=[];corrected_q_fwd=[];series_aft=[];
error_p_aft=[];error_q_aft=[];
 corrected_p_aft=[]; corrected_q_aft=[];
%================================================
load  camex_200108232_TB_fwd_v3_1.dat;
fwd = camex_200108232_TB_fwd_v3_1;

load  camex_200108232_TB_aft_v3_1.dat;
aft = camex_200108232_TB_aft_v3_1;

 %quadratic poly coeffs
 v_poly=[-1.0893e-004 0.0046 0.4339];
 h_poly=[5.0000e-005 -3.5000e-004 0.5334];


gamma_h=0.645;
gamma_v=0.42;
tau=0.778;
tdn_c=67.4;
sst=29;

tv_surface=185.5;
th_surface=107.5;

tv_surface_aft=179.5;
th_surface_aft=95.5;

load cstar_2001232_nav3.txt;
camex0=cstar_2001232_nav3;
s=find(camex0(:,1)>=360 & camex0(:,1)<=25104);
camex=camex0(s,:);
%================================================
%shift roll and pitch  down k elements
```

```
k=11;
roll=camex(:,21)+0.5;
camex(:,21)=roll([end-k+1:end 1:end-k]);
%camex(:,21)=0;
pitch=camex(:,20)+0.5;
camex(:,20)=pitch([end-k+1:end 1:end-k]);

heading=camex(:,26);
camex(:,26)=heading([end-k+1:end 1:end-k]);

track=camex(:,47);
camex(:,47)=track([end-k+1:end 1:end-k]);

 h_aft=176.5;
%=========================================
 eps=[];

 scan_start=711; %Start scan
 scan_stop=718;  %Stop scan

for start=scan_start:scan_stop;
stop=start;

v_fwd=233;
h_fwd=178;

%=============================================
%find data for scan of interest
f=find(fwd(:,1)>=start & fwd(:,1)<=stop);
a=find(aft(:,1)>=start & aft(:,1)<=stop);
a2=find(camex(:,2)>=start & camex(:,2)<=stop);

ff=fwd(f,:);
aa=aft(a,:);
camex1=camex(a2,:);

%=================================================
%Convert azimuth values to between 0 and 360
ff(:,7)=rem(ff(:,7),360);
aa(:,7)=rem(aa(:,7),360);

%=================================================
%tb to be used in incidence
 tbv_mean_fwd=repmat(v_fwd,26,1) ;
 tbh_mean_fwd=repmat(h_fwd,26,1) ;
```

```
%================================================
%column 22 and 23 are now tbv_mean and tbh_mean respectively
ff=[ff tbv_mean_fwd tbh_mean_fwd];   %fwd
aa=[aa tbv_mean_fwd tbh_mean_fwd];   %aft

%Make fwd azimuth between -50 and 50 deg
az_300=find(ff(:,7)>300);
ff(az_300,7)=ff(az_300,7)-360;

%fwd, remove 6 outlying az pts
 a25=find(ff(:,7)>=25);
 ff(a25,:)=NaN;

%================================================
%Incidence angle correction
%===========
[abb,ffb] = SmoothResample(camex,start,stop);
%===========

% slope_v=2.04 ; slope_h=-0.54;
 slope_v=2.22 ; slope_h=0.18;

mean_inc=53.3;

heading_fwd=ffb(:,5);%heading fwd
track_fwd=ffb(:,6);%track fwd
roll_fwd = ffb(:,4); %roll vector   %fwd
pitch_fwd = ffb(:,3); %pitch vector
azimuth_fwd = ffb(:,2).*(pi/180); %az in rad

heading_aft=abb(:,5);%heading aft
track_aft=abb(:,6);%track aft
roll_aft = abb(:,4); %roll vector  %aft
pitch_aft = abb(:,3); %pitch vector
azimuth_aft = abb(:,2).*(pi/180); %az in rad

 theta_i_fwd = mean_inc + pitch_fwd.*cos(azimuth_fwd) - roll_fwd.*sin(azimuth_fwd);
%Theta(i) to be used in incidence correction
 theta_i_aft = mean_inc + pitch_aft.*cos(azimuth_aft) - roll_aft.*sin(azimuth_aft);
%Theta(i) to be used in incidence correction

ff=[ff theta_i_fwd]; % column 24 is theta(i)
aa=[aa theta_i_aft];

theta_corrected_fwd=[];
theta_corrected_aft=[];
```

```
for jj= start:stop
scan11_fwd=ff(:,:);
scan11_aft=aa(:,:);

       %1:21 ff 25: V inc corrected 26: H inc corrected
        theta_corrected_fwd=[theta_corrected_fwd; scan11_fwd,scan11_fwd(:,8) -
(scan11_fwd(:,24)-(mean_inc)).*slope_v, scan11_fwd(:,9) -(scan11_fwd(:,24)-
(mean_inc)).*slope_h];
%         theta_corrected_fwd=[theta_corrected_fwd; scan11_fwd,  scan11_fwd(:,22) +
(scan11_fwd(:,24)).*slope_v,  scan11_fwd(:,23) + (scan11_fwd(:,24)).*slope_h];
        theta_corrected_aft=[theta_corrected_aft; scan11_aft,  scan11_aft(:,8) -
(scan11_aft(:,24)-(mean_inc)).*slope_v,  scan11_aft(:,9) - (scan11_aft(:,24)-
(mean_inc)).*slope_h];

end

%=================================================================
==========
%Model with incidence correction
Tbv_fwd = theta_corrected_fwd(:,25); %Corrected Tbv vector, Fwd
Tbh_fwd = theta_corrected_fwd(:,26); %Corrected Tbh vector

 Tbv_aft = theta_corrected_aft (:,25); %Tbv vector, Aft
 Tbh_aft = theta_corrected_aft (:,26); %Tbh vector

%=================================================================
=========

tatmos_v = (Tbv_fwd- ((sst+273)*(1-gamma_v)*tau))./(1+tau*gamma_v);
tatmos_h = (Tbh_fwd- ((sst+273)*(1-gamma_h)*tau))./(1+tau*gamma_h);

tatmos_v_aft = (Tbv_aft- ((sst+273)*(1-gamma_v)*tau))./(1+tau*gamma_v);
tatmos_h_aft = (Tbh_aft- ((sst+273)*(1-gamma_h)*tau))./(1+tau*gamma_h);

tatmos=nanmean([tatmos_v tatmos_h],2);
tatmos_aft=nanmean([tatmos_v_aft tatmos_h_aft],2);
%=========================================

rhov=polyval(v_poly,theta_corrected_fwd(:,24));
rhoh=polyval(h_poly,theta_corrected_fwd(:,24));

rhov_aft=polyval(v_poly,theta_corrected_aft(:,24));
rhoh_aft=polyval(h_poly,theta_corrected_aft(:,24));
%==================================
```

```
v_model = tatmos_v + tatmos_v .* rhov.*tau + tv_surface*tau ;
h_model = tatmos_h + tatmos_h .* rhoh.*tau + th_surface*tau ;

v_model_aft = tatmos_v_aft + tatmos_v_aft .* rhov_aft.*tau + tv_surface_aft*tau;
h_model_aft = tatmos_h_aft + tatmos_h_aft .* rhoh_aft.*tau + th_surface_aft*tau;

%=================================================================
==
e=0.9087;
gamma_fwd = (roll_fwd.*cos(azimuth_fwd) + pitch_fwd.*sin(azimuth_fwd)).*(pi/180);
%Gammas in radian, Fwd
beta_p_fwd=((45+e)*(pi/180))+gamma_fwd; %Betas in radians
beta_q_fwd=((-45+e)*(pi/180))+gamma_fwd;

gamma_aft = (roll_aft.*cos(azimuth_aft) + pitch_aft.*sin(azimuth_aft)).*(pi/180);
%Gammas in radian, Aft
beta_p_aft=((45+e)*(pi/180))+gamma_aft; %Betas in radians
beta_q_aft=((-45+e)*(pi/180))+gamma_aft;

%=================================================================
==========
tbp_sim_fwd = h_model .*  (cos(beta_p_fwd)).^2 + v_model .* (sin(beta_p_fwd)).^2;
%Fwd
tbq_sim_fwd = h_model .*  (cos(beta_q_fwd)).^2 + v_model .* (sin(beta_q_fwd)).^2;

tbp_sim_aft = h_model_aft .*  (cos(beta_p_aft)).^2 + v_model_aft .*
(sin(beta_p_aft)).^2; %Aft
tbq_sim_aft = h_model_aft .*  (cos(beta_q_aft)).^2 + v_model_aft .*
(sin(beta_q_aft)).^2;

 yaw_fwd=heading_fwd-track_fwd;
 yaw_aft=heading_aft-track_aft;

%1:measP 2:measQ 3:simP 4:simQ 5:az 6:pitch 7:roll
series_fwd=[series_fwd;ff(1:20,10), ff(1:20,11), tbp_sim_fwd(1:20), tbq_sim_fwd(1:20),
azimuth_fwd(1:20), pitch_fwd(1:20), roll_fwd(1:20)]; %fwd
series_aft=[series_aft;aa(1:26,10), aa(1:26,11), tbp_sim_aft(1:26), tbq_sim_aft(1:26),
azimuth_aft(1:26), pitch_aft(1:26), roll_aft(1:26), yaw_aft(1:26), theta_i_aft(1:26)]; %aft

end

 %fwd
 figure,plot(series_fwd(:,1),'.-');grid;hold
 plot(series_fwd(:,3),'r.-')
 xlabel('Time series');ylabel('TbP,K');title(' Modelled and Measured, Scan 711-718,
FWD');
```

```
legend('Measured','Modelled');
%  axis([0 160 200 212]);


 figure,plot(series_fwd(:,2),'.-');grid;hold
 plot(series_fwd(:,4),'r.-')
 xlabel('Time series');ylabel('TbQ,K');title(' Modelled and Measured, Scan 711-718,
FWD');
 legend('Measured','Modelled');
%   axis([0 160 200 212]);


%Aft

 figure,plot(series_aft(:,1),'.-');grid;hold
 plot(series_aft(:,3),'r.-')
 xlabel('Time series');ylabel('TbP,K');title(' Modelled and Measured, Scan 711-718,
AFT');
legend('Measured','Modelled');
%  axis([0 160 200 212]);


 figure,plot(series_aft(:,2),'.-');grid;hold
 plot(series_aft(:,4),'r.-')
 xlabel('Time series');ylabel('TbQ,K');title(' Modelled and Measured, Scan 711-718,
AFT');
 legend('Measured','Modelled');
%   axis([0 160 200 212]);
```

LIST OF REFERENCES

[1] Elachi, C. Introduction to the Physics and Techniques of Remote Sensing. John Wiley & Sons, Inc., New York, 1987

[2] Fawwaz T. Ulaby, Richard K. Moore, Adrian K. Fung, Microwave Remote Sensing : active and passive, Vol-1, Addison-Wesley Pub. Co, 1986

[3] Constantine A. Balanis, Advanced Engineering Electromagnetics, John Wiley & Sons, March 1989

[4] Klein, L. A., & Swift C. T. An Improved Model for the Dielectric Constant of Sea Water at Microwave Frequencies. IEEE Trans. Antennas Propag., AP-25, pp.104-111, 1977.

[5] Meeks. M. L., & Lilley A. E..The Microwave Spectrum of Oxygen in the Earth's Atmosphere. J. Geophys. Res., 68, pp. 1683-1703, 1963

[6] Wilheit, T. T., and A. T. C. Chang, "An Algorithm for Retrieval of Ocean Surface and Atmospheric Parameters from the Observations of the Scanning Multifrequency Microwave Radiometer (SMMR)", *Radio Science* (15), 525-544, 1980.

[7] Wentz, F. J., "A Well-Calibrated Ocean Algorithm for SSMI", *J. Geophys. Res.*, Vol. 102, No. C4, 8703-8718, 1997.

[8] Frank Wentz, "Measurement of Oceanic Wind Vector Using Satellite Microwave Radiometers", *IEEE Trans. Geosci. Remote Sensing*, vol. 30, September 1992.

[9] Mark James David E. Simmons, Conically-Scanning Two-Look Airborne Radiometer (C-STAR) Final Report, Oct 1994

[10] F.Lafontaine, Format for the 2001 C-STAR ASCII text files, basic quality control, NASA Marshal Space Flight Center, Aug 2001

[11] Yueh, S. H., W. J. Wilson, F. K. Li, W. B. Ricketts, and S. V. Nghiem, "Polarimetric Measurements of Sea Surface Brightness Temperatures using an Aircraft K-band Radiometer", *IEEE Trans. Geosci. Remote Sensing*, (33), 85-92, 1995.

[12] I. Corbella, A.J. Gasiewski, M. Klein and J.R Piepmeir, "Compensation of Elevation Angle Variations in Polarimetric Brightness Temperature Measurements from Airborne Microwave Radiometers", IEEE Trans. Geosci. Remote Sensing, vol. 39, January 2001.

[13] Jean Yves Kabore, Linwood W Jones, Robbie Hood, Mark James and Frank LaFontaine, An Incidence Angle Correction for a Conical Scanning Microwave Radiometer, IEEE South East Conference, April 8-10, 2005, Ft Lauderdale, FL

[14] Remote Sensing System, SSM/I data, Available on web site
http://www.ssmi.com/ssmi/ssmi_browse.html